Neural substrates of cold nociception in *Drosophila* larva

Atit A. Patel[1], Albert Cardona[2,3,4], and Daniel N. Cox[1*]

[1]Neuroscience Institute, Georgia State University, Atlanta, GA, USA

[2]HHMI Janelia Research Campus, Ashburn, VA, USA

[3]MRC Laboratory of Molecular Biology, Cambridge, UK

[4]Department of Physiology, Development, and Neuroscience, University of Cambridge, UK

*** Correspondence:**
Corresponding Author
dcox18@gsu.edu

Keywords: cold nociception, thermosensation, somatosensory circuits, *Drosophila*.

Abstract

Metazoans detect and differentiate between innocuous (non-painful) and/or noxious (harmful) environmental cues using primary sensory neurons, which serve as the first node in a neural network that computes stimulus specific behaviors to either navigate away from injury-causing conditions or to perform protective behaviors that mitigate extensive injury. The ability of an animal to detect and respond to various sensory stimuli depends upon molecular diversity in the primary sensors and the underlying neural circuitry responsible for the relevant behavioral action selection. Recent studies in *Drosophila* larvae have revealed that somatosensory class III multidendritic (CIII md) neurons function as multimodal sensors regulating distinct behavioral responses to innocuous mechanical and nociceptive thermal stimuli. Recent advances in circuit bases of behavior have identified and functionally validated *Drosophila* larval somatosensory circuitry involved in innocuous (mechanical) and noxious (heat and mechanical) cues. However, central processing of cold nociceptive cues remained unexplored. We implicate multisensory integrators (Basins), premotor (Down-and-Back) and projection (A09e and TePns) neurons as neural substrates required for cold-evoked behavioral and calcium responses. Neural silencing of cell types downstream of CIII md neurons led to significant reductions in cold-evoked behaviors and neural co-activation of CIII md neurons plus additional cell types facilitated larval contraction (CT) responses. We further demonstrate that optogenetic activation of CIII md neurons evokes calcium increases in these neurons. Collectively, we demonstrate how *Drosophila* larvae process cold stimuli through functionally diverse somatosensory circuitry responsible for generating stimulus specific behaviors.

Introduction

Metazoans detect innocuous and/or noxious environmental cues and appropriately generate relevant behavioral responses. There is a large diversity in types of nervous systems from relatively simple nerve nets to highly complex centralized organs dedicated for processing and executing behavioral commands. The ability of an organism to sense and respond to environmental cues is based on the underlying neural architecture and its connectivity to muscle groups for generating behavioral responses. Understanding the neural substrates underlying the execution of how behavioral commands are generated in the nervous system, spanning from the sensory neuron input to motor neuron output, constitutes one of the key areas of research in contemporary neuroscience.

Drosophila melanogaster is among the premier model organisms for studying molecular, cellular and circuit bases of behaviors in modern neuroscience driven by advances in electron microscopy (EM) connectomics, ability to perform high-throughput behavioral screens, characterization of stereotyped behavioral phenotypes, the ability to perform cell-type specific manipulations and genetic accessibility (for review see (Eschbach & Zlatic, 2020). Another critical benefit of using *Drosophila* to study neural connectivity at the synaptic level is its relatively small, but complex CNS, where there are only ~10,000 neurons in the *Drosophila* larval CNS and ~100,000 neurons in adult *Drosophila melanogaster* brain compared to 86 billion neurons in the human brain (Herculano-Houzel, 2009; Scheffer et al., 2020). Highly detailed serial section transmission electron microscopy (ssTEM) whole brain volumes with synaptic level resolution have been obtained for both *Drosophila* larval (Ohyama et al., 2015) and adult (Zheng et al., 2018) brains, where neurons were reconstructed using a collaborative web-based software, CATMAID (Saalfeld et al., 2009; Schneider-Mizell et al., 2016). Concerted efforts from many laboratories have made tremendous advances in reconstructing the *Drosophila* larval connectome at synaptic level resolution and there has been great progress in mapping out select connectomes at the EM level (Clark et al., 2018; Eschbach & Zlatic, 2020; Kohsaka et al., 2017). Connectomes have been further validated using behavioral and functional imaging studies for olfaction in combination with learning and memory (Berck et al., 2016; Eichler et al., 2017; Eschbach et al., 2020; Saumweber et al., 2018), feeding (Miroschnikow et al., 2018; Schlegel et al., 2016), visual processing (Larderet et al., 2017), locomotion (Carreira-Rosario et al., 2018; Fushiki et al., 2016; Heckscher et al., 2015; Hiramoto et al., 2021; Kohsaka et al., 2019; Zarin et al., 2019; Zwart et al., 2016), chemotaxis (Tastekin et al., 2018), thermosensation (Hernandez-Nunez et al., 2021), mechanosensation (Jovanic et al., 2016; Jovanic et al., 2019; Masson et al., 2020), nociceptive modalities (Burgos et al., 2018; Gerhard et al., 2017; Hu et al., 2017; Imambocus et al., 2022; Kaneko et al., 2017; Ohyama et al., 2015; Takagi et al., 2017), among others (Andrade et al., 2019; Huckesfeld et al., 2021; Imura et al., 2020; Mark et al., 2021; Valdes-Aleman et al., 2021; Winding et al., 2022).

We are particularly interested in how larval somatosensation functions through peripheral sensory neurons located along the body wall just below the larval cuticle. Larval somatosensory

neurons are comprised of type I, mono-ciliated dendrites, (external sensory (es) and chordotonal (Ch) neurons) and type II, bipolar dendritic (td and bd) and highly branched multidendritic (md) neurons (classes I-IV, referred to as CI-IV md). Functional and behavioral roles of these sensory neurons include proprioception (CI md & Ch) (Caldwell et al., 2003; He et al., 2018; Vaadia et al., 2018), heat thermoreception (CIV md) (Babcock et al., 2009; Im et al., 2015; Ohyama et al., 2015; Tracey et al., 2003), cold thermoreception (Ch, CII md, & CIII md) (Turner et al., 2016; Turner et al., 2018), chemoreception (CIV md) (Himmel et al., 2019; Lopez-Bellido et al., 2019) and mechanosensation (Ch, CII md, CIII md, & CIV md) (Hu et al., 2017; Hwang et al., 2007; Jovanic et al., 2019; Masson et al., 2020; Ohyama et al., 2015; Scholz et al., 2015). Recent studies have unraveled circuit bases underlying thermo- (heat), chemo- and mechanosensation, however, circuit bases of noxious cold thermosensory evoked behaviors are yet to be described (Burgos et al., 2018; Hu et al., 2017; Hu et al., 2020; Imambocus et al., 2022; Jovanic et al., 2016; Jovanic et al., 2019; Hernandez-Nunez et al., 2021; Kaneko et al., 2017; Lopez-Bellido et al., 2019; Masson et al., 2020; Ohyama et al., 2015; Yoshino et al., 2017).

Neural circuitry downstream of select somatosensory neurons has been elucidated both physiologically and behaviorally in the context of nociceptive stimuli that evoke characteristic rolling behavior in *Drosophila* larvae. Specifically, Ch and CIV md neurons signal through multisensory integrator neurons (Basins) via ascending pathways to command neurons for mechanical and nociceptive stimulation that synergistically impact larval rolling escape responses (Ohyama et al., 2015). CIV md neuron mediated nociceptive escape behaviors also function through premotor neurons such as Down-and-Back (DnB) and medial clusters of CIV md interneurons (mCSI) (Burgos et al., 2018; Yoshino et al., 2017). Additionally, A08n projection neurons receive input from CIV md neuron and the peptidergic neuron DP-ilp7 to integrate multisensory inputs from CII, CIII and CIV md neurons (Imambocus et al., 2022). A08n and DP-ilp7 neurons are specifically required for nociceptive mechanical and chemical sensing but not for nociceptive thermosensation (Hu et al., 2017; Imambocus et al., 2022; Kaneko et al., 2017; Tenedini et al., 2019; Vogelstein et al., 2014). Lastly, Ch and CIII md neuronal connectivity, through ascending projection neurons A09e and TePns as well as premotor neuron Chair-1, are required for anemotaxis and innocuous mechanical sensing (Jovanic et al., 2019; Masson et al., 2020). While CIII md neuron connectivity to select second order neurons has been published (Masson et al., 2020), the functional and behavioral roles of these circuit components in the context of cold nociception remain unexplored. We hypothesized that the noxious cold sensitive somatosensory nociceptive circuit functions through shared circuitry amongst other somatosensory modalities.

Analyses of cold sensitive circuitry downstream of CIII md neurons elucidated dual pathways for signal transduction: (1) CIII md neurons directly signal through premotor neurons that modulate motor activity and (2) CIII md neurons also function via multisensory integrators and projections neurons to convey somatosensory information to higher order brain regions. Somatosensory neurons (Ch and CIII md) are required for cold-evoked responses but not CIV md neurons (Turner et al., 2016; Turner et al., 2018). Multisensory integration neurons, Basins 1-

114 4, are required for cold nociception, facilitate CIII md evoked larval contraction (CT) responses,
115 and select Basins exhibit cold evoked increases in calcium. Premotor neurons, DnB and mCSI,
116 are required and facilitate cold-evoked behavioral responses, whereas Chair-1 premotor neurons
117 are required for cold nociception but do not facilitate CIII md neuron mediated responses. Lastly,
118 nociceptive projection neurons A09e and TePns also integrate cold stimuli but only A09e
119 neurons enhance CIII md neuron mediated behavioral responses.
120
121 **Results**
122
123 **Peripheral sensory neurons share synaptic partners**
124 Recent work on competitive interactions and behavioral transitions in *Drosophila* larvae
125 has reported CIII md and Ch connectomes in the context of larval mechanosensation (Masson et
126 al., 2020). We performed a comparative circuit analysis of somatosensory (Ch, CIII md and CIV
127 md) neurons using an online repository hosted by LMB Cambridge, which contains a ssTEM
128 volume of *Drosophila melanogaster* first instar larval central nervous system and a repository of
129 neural reconstructions (https://neurophyla.mrc-lmb.cam.ac.uk/). Here, we report and
130 contextualize relevant CIII md neuron downstream neurons, whose functional roles in cold
131 nociception were evaluated. The meta-analysis of previously published literature on *Drosophila*
132 larval somatosensory connectomes revealed several common post-synaptic partners that are
133 shared amongst Ch, CIII md and CIV md neurons (**Figure 1A**). CIII md neurons are upstream of
134 multisensory integration neurons, pre-motor neurons and projection neurons. Class III md
135 neurons are synaptically connected to multisensory integration neurons (Basin-2, -3 & -4). The
136 downstream pathway from Basins includes connectivity to A00c neurons and a polysynaptic
137 pathway to the rolling command neuron (Goro) via A05q neurons. CIII md neurons are also
138 connected to various pre-motor neurons, which are ventral nerve cord localized neurons
139 providing synaptic input to motor neurons, including DnB, A02n and Chair-1, and projection
140 neurons including A05q, A09e, TePn05 and A08n. The CIII md neuron connectome analyses
141 reveal broad second order connectivity and complex interconnectivity amongst second order
142 neurons (**Figure 1A, Figure 1-figure supplement 1**). Functional and behavioral roles of CIII md
143 neuron second order interneurons in cold nociception remain unexplored and below we address
144 this knowledge gap.
145
146
147 **Functional analysis of somatosensory neurons in cold nociception**
148 Due to shared post-synaptic neural connectivity of Ch, CIII md and CIV md neurons
149 (**Figure 1A, Figure 1-figure supplement 1**), we first assessed functional roles of these sensory
150 neurons in cold nociception by investigating: (1) stimulus-evoked calcium responses in the
151 *Drosophila* larval ventral nerve cord; (2) cold-evoked calcium responses of these sensory
152 neurons; (3) necessity and sufficiency of these sensory neurons in cold-evoked behaviors; and

153 (4) examining whether co-activating multiple sensory neurons facilitates CIII-mediated
154 behavioral response in *Drosophila* larvae.
155
156 1. CaMPARI analysis reveals distinct neuropil activation patterns by sensory stimuli
157 *Drosophila* larvae have distinct behavioral responses to various sensory stimuli including
158 touch, heat or cold. Exposure to noxious cold temperatures (≤10°C) evokes highly stereotyped
159 head and tail withdrawal towards the center of the animal, termed here as contraction (CT)
160 response (Patel et al., 2022; Turner et al., 2016). The cold-evoked CT response is defined as at
161 least 10% reduction in larval surface area (**Figure 1-figure supplement 4**). Innocuous
162 mechanical stimuli evokes a suite of behaviors including pausing, turning, head withdrawal,
163 and/or reverse locomotion. Noxious heat exposure leads to a corkscrew body roll escape
164 response (Babcock et al., 2011; Im et al., 2015; Ohyama et al., 2015; Tracey et al., 2003).
165 Previous work on stimulus-evoked changes in neural ensembles in larval zebrafish (*Danio rerio*)
166 used the genetically encoded calcium integrator CaMPARI to reveal distinct CNS neural
167 activation patterns in response noxious heat or cold exposure (Fosque et al., 2015). CaMPARI
168 affords great spatial resolution as stimulus-evoked neural responses are captured from a freely
169 moving animal.
170 With CaMPARI and pan-neural imaging of ventral nerve cord neurons, we visualized
171 central representations of somatosensory stimuli across sensory modalities including innocuous
172 mechanical, noxious cold or noxious heat, which are primarily detected via Ch, CIII md, & CIV
173 md neurons, respectively. We pan-neuronally expressed CaMPARI using *R57C10*^{GAL4} (Jenett et
174 al., 2012; Pfeiffer et al., 2008) and *Drosophila* larvae were simultaneously exposed to diverse
175 sensory stimuli and photoconverting light. Post-hoc imaging of intact *Drosophila* larvae ventral
176 nerve cord revealed relatively little neural activity when larvae are not presented with any
177 sensory stimulus (**Figure 1-figure supplement 2**). However, upon innocuous mechanical (gentle
178 touch) stimulation, there is a marked increase in neural activation as reported by F_{redLUT} (**Figure**
179 **1-figure supplement 2**). *Drosophila* larvae exposed to noxious heat experience a large, spatially
180 broad increase in neural activity. Incidentally, similar neuropil regions appear to be activated by
181 both innocuous touch and noxious heat, albeit at different levels (**Figure 1-figure supplement**
182 **2**). Lastly, noxious cold exposure leads to robust neural activation medially, in the neuropil,
183 however, cell bodies seem to have lower activation levels compared to touch or heat stimulations
184 (**Figure 1-figure supplement 2**). These experiments measuring pan-neuronal ventral nerve cord
185 activity in response to sensory stimuli would be ideal for comparative neural activation analyses,
186 were the spatial resolution of the optical microscope sufficient. Acknowledging the limitations of
187 the approach, we heretofore focus instead on single-cell type specific genetic driver lines for
188 identified neurons that can be assigned to known neurons in the connectome,
189
190 2. CIII md somatosensory neurons exhibit robust Ca^{2+} responses to cold
191 Somatosensory neurons function as primary sensors of external stimuli. Ch and CIII md
192 neurons have previously been reported to present cold evoked increases in Ca^{2+} (Turner et al.,

193 2016; Turner et al., 2018). Previous reports indicate that CIV md neurons are weakly sensitive to
194 cold stimuli (Turner et al., 2016). Cold sensitivity of sensory neurons (Ch, CIII md, & CIV md)
195 was assessed by selectively expressing the CaMPARI2 Ca^{2+} integrator in sensory neurons using
196 cell-type specific driver lines (**Figure 1-figure supplement 3A**). CaMPARI2 signal, as assessed
197 by F_{red}/F_{green} ratios at the cell body, reveal all three neuron subtypes (Ch, CIII md and CIV md)
198 have significantly higher response upon cold exposure compared to no stimulus controls
199 (**Figure 1B, Figure 1-figure supplement 3B**). Unsurprisingly, as high-threshold nociceptors,
200 CIII md or CIV md neurons present relatively low responses upon photoconverting light
201 exposure *sans* cold (**Figure 1B, Figure 1-figure supplement 3B**). However, mechanosensitive
202 Ch neurons exhibit relatively high responses upon exposure to only photoconverting light but no
203 stimulus indicative of high baseline neuronal activity processing mechanosensory information
204 (**Figure 1B, Figure 1-figure supplement 3B**).
205 Similar to the analysis at cell bodies, in the dendrites of Ch neurons we observe marked
206 increases in CaMPARI2 response to photoconverting light (control), however, upon cold
207 exposure (experimental condition) there is a further increase in CaMPARI2 response (**Figure**
208 **1C**). Sholl intensity analysis (see methods) likewise reveals that CIII md neurons present
209 relatively low CaMPARI2 response in control conditions, however, there is a robust cold evoked
210 increase in CaMPARI2 response throughout the dendrites (**Figure 1C**). Interestingly, CIV md
211 neurons also exhibited significant increases in CaMPARI2 response upon cold exposure in the
212 cell body (**Figure 1B**). we measure a higher cold-evoked CIV md neuron CaMPARI2 response
213 closer to the soma (**Figure 1C**). However, there is no change in distal dendritic CIV md neuron
214 CaMPARI2 response between cold and no stimulus conditions (**Figure 1C**). CIII md have robust
215 cold evoked Ca^{2+} responses compared to Ch and CIV md neurons, which have relatively low
216 cold evoked Ca^{2+} increases (**Figure 1B,C**). Therefore, we identified CIII md neurons as the most
217 sensitive to noxious cold temperatures, and thus we focused our study on the neural circuits
218 postsynaptic to CIII md neurons.
219
220 3. <u>CIII md somatosensory neurons are necessary and sufficient for the cold response</u>
221 The analysis of neuronal activity responses to cold exposure revealed distinct patterns for
222 both central and somatosensory neurons, with most robust responses to stimuli evoked in CIII
223 md neurons.
224 We assessed the necessity of somatosensory neurons in noxious cold-evoked behavioral
225 responses (**Figure 1-figure supplement 4**) by expressing tetanus toxin light chain, which
226 inhibits neurotransmitter release (Sweeney et al., 1995). Based on Ca^{2+} imaging, we expected
227 both Ch and CIII md neurons may be necessary for cold evoked CT responses. Neural silencing
228 of Ch and CIII md neurons led to significant reductions in cold evoked CT responses compared
229 to either *w1118* (parental line) or $Empty^{GAL4}$ controls (a GAL4 construct lacking the promotor
230 sequence; **Figure 1D, E**). Instantaneous behavioral response curves also indicate lower cold
231 sensitivity when either Ch or CIII md neurons are silenced. However, inhibiting neurotransmitter
232 release in CIV md neurons alone did not result in significant reductions in cold evoked CT

233 responses (**Figure 1D, E**). Among the three somatosensory neuron types tested, neural silencing
234 of CIII md neurons resulted in the strongest impairment in cold evoked behavioral response.
235 Next, we evaluated whether neural activation of sensory neurons via optogenetics would
236 be sufficient to elicit the CT behavioral response (**Figure 1-figure supplement 5A**). We
237 expressed the engineered channelrhodopsin ChETA in individual sensory neuron subtypes and
238 assessed evoked behavioral responses (Gunaydin et al., 2010). When assessing evoked
239 responses, we first analyzed CT responses as measured by changes in surface area (**Figure 1-**
240 **figure supplement 5B**). Only neural activation of CIII md neurons led to CT responses in
241 *Drosophila* larvae (**Figure 1F, G**) consistent with our previously published work (Turner et al.,
242 2016). Additionally, we analyzed larval mobility, which refers to changes in larval postures as
243 measured by changes in occupied space (**Figure 1-figure supplement 5C**). Upon neural
244 activation of CIII md neurons, there is a large increase in *Drosophila* larval immobility
245 compared to controls (**Figure 1-figure supplement 6A-C**). However, there was no difference in
246 immobility when either Ch or CIV md neurons were optogenetically activated compared to
247 control (**Figure 1-figure supplement 6A-C**). Of the somatosensory neurons tested, only CIII
248 md neurons are sufficient to elicit the CT response.
249
250 4. <u>Effect of co-activating CIII md somatosensory neurons plus additional somatosensory</u>
251 <u>neuron classes</u>
252 Both Ch and CIV md neurons share common first order post-synaptic partners with CIII
253 md neurons and all three somatosensory present cold-evoked increases in calcium levels.
254 However, neither Ch nor CIV are sufficient to elicit a CT response. To further clarify the roles
255 of Ch and CIV in cold evoked behaviors, we simultaneously activated CIII md neurons plus
256 either Ch or CIV md neurons. We expected that co-activation of multiple sensory neuron
257 subtypes would facilitate optogenetically-evoked CT responses. Optogenetic activation of CIII
258 md neurons using two cell type specific driver lines (*19-12*^{GAL4} and *R83B04*^{GAL4}) led to sustained
259 increases in instantaneous CT responses compared to control, where only one driver line (*19-*
260 *12*^{GAL4}) was used to activate CIII md neurons (**Figure 1H, I**). The activation of CIII md neurons
261 using two driver lines (expressed in the same cell type, CIII md) led to a significant increase in
262 immobility compared to single *GAL4* driver-mediated activation of these neurons (**Figure 1-**
263 **figure supplement 6D-F**), suggesting a single GAL4 line does not exhaust the dynamic range of
264 the CT response. Co-activation of CIII md and Ch neurons, which are cold sensitive and required
265 for cold evoked CT responses, led to a subtle initial increase in instantaneous CT response
266 compared to CIII activation alone, however, the initial increase in evoked CT response was
267 quickly reduced to well below control (**Figure 1H, I**). Therefore the co-activation of two
268 somatosensory neuron types, Ch and CIII md, elicited a CT response that varied along the
269 temporal axis relative to the activation of CIII md alone. *Drosophila* larval immobility was
270 reduced during co-activation of Ch and CIII md neurons compared to CIII md neuron activation
271 alone suggesting that Ch neurons do not facilitate CIII md neuron mediated CT responses
272 (**Figure 1-figure supplement 6D-F**). CIV md and CIII md neurons share a large proportion of

273 common second order interneuron connectivity including multisensory integration neurons,
274 premotor and ascending neurons. We predicted that CIV md and CIII md neuron co-activation
275 might potentiate CT responses. Interestingly, simultaneous activation of CIII and CIV md
276 neurons led to small but insignificant reductions in instantaneous and peak CT responses
277 compared to CIII md neuron activation alone (**Figure 1H, I**). Similarly, co-activation of CIII md
278 and CIV md neurons did not alter larval immobility compared to only CIII md neuron activation
279 (**Figure 1-figure supplement 6D-F**). Ch neurons are cold sensitive and required for cold
280 nociceptive behaviors but do not facilitate CIII md neuron evoked behavioral responses.
281 Meanwhile, CIV md neurons are modestly cold sensitive but are not required for cold
282 nociception and do not facilitate CIII md neuron evoked CT responses. Collectively, CIII md
283 neurons have the strongest cold-evoked calcium response, are required for cold-evoked
284 behavioral response and sufficient for the CT response.
285
286
287

288

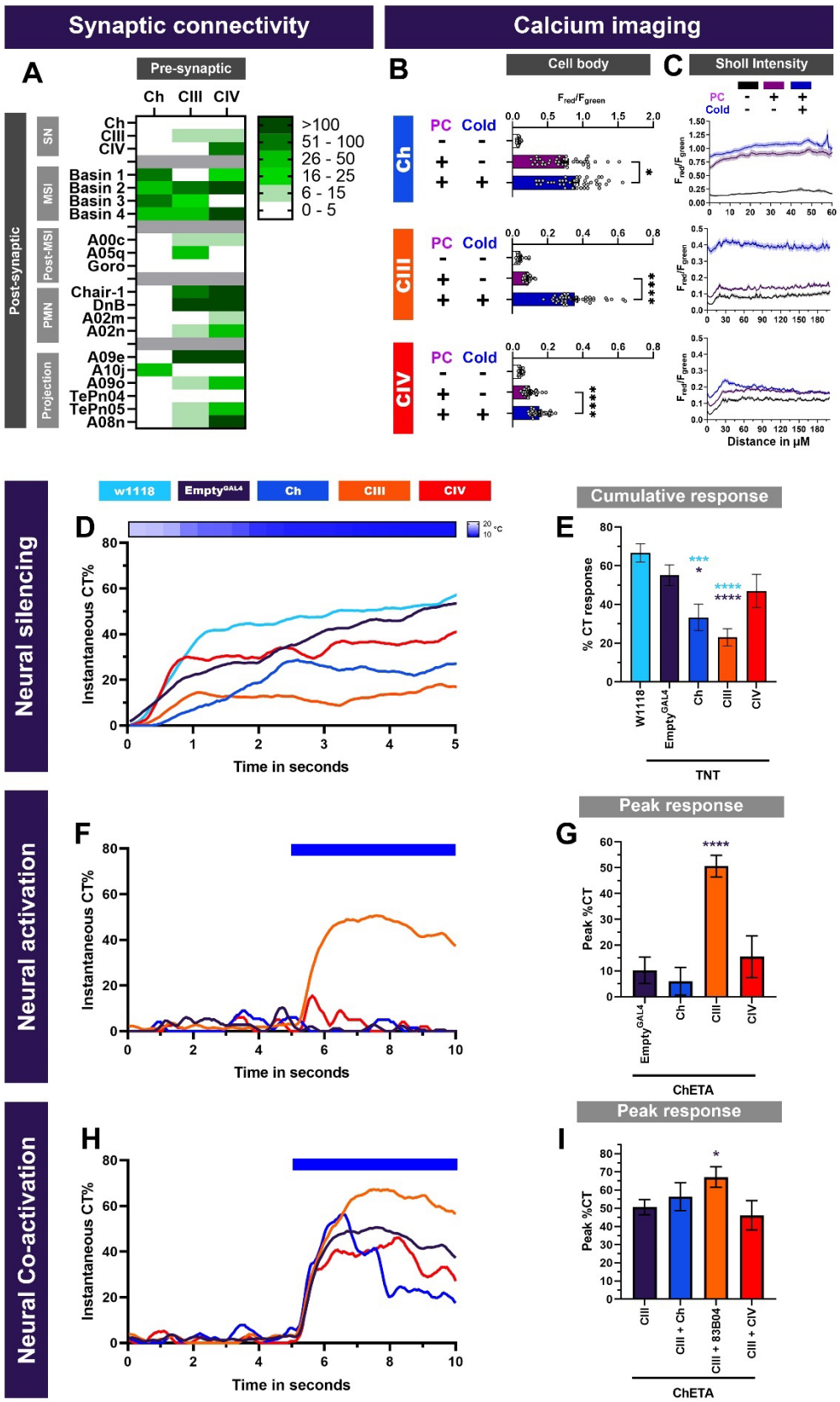
Synaptic connectivity
Calcium imaging
A
Pre-synaptic
Ch CIII CIV
Post-synaptic
SN
MSI
Post-MSI
PMN
Projection
Ch
CIII
CIV
Basin 1
Basin 2
Basin 3
Basin 4
A00c
A05q
Goro
Chair-1
DnB
A02m
A02n
A09e
A10j
A09o
TePn04
TePn05
A08n
>100
51 - 100
26 - 50
16 - 25
6 - 15
0 - 5
B
Cell body
C
Sholl Intensity
PC
Cold
Ch
CIII
CIV
Distance in µM
Neural silencing
w1118
EmptyGAL4
Ch
CIII
CIV
D
Instantaneous CT%
Time in seconds
Cumulative response
E
% CT response
W1118
EmptyGAL4
Ch
CIII
CIV
TNT
Neural activation
F
Instantaneous CT%
Time in seconds
Peak response
G
Peak %CT
EmptyGAL4
Ch
CIII
CIV
ChETA
Neural Co-activation
H
Instantaneous CT%
Time in seconds
Peak response
I
Peak %CT
CIII
CIII + Ch
CIII + 83B04
CIII + CIV
ChETA

289 **Figure 1: CIII md neurons are primary cold sensors and share common post-synaptic**
290 **partners with mechanosensory and nociceptive Ch and CIV md neurons**
291 **neurons**
292 **(A)** Sensory neuron second order connectome analyses. Heatmap plot of synaptic connections
293 between sensory neuron subtypes including chordotonal (Ch), class III (CIII) md, class IV (CIV)
294 md neurons and previously published centrally located neurons. Sensory neurons (SN) Ch, CIII
295 md, and CIV md were analyzed. Multisensory integrator (MSI) neurons include Basin-1, -2, -3,
296 and -4. Neurons downstream of MSI (Post-MSI) include A00c, A05q and Goro. Premotor
297 neurons (PMNs) include Chair-1 (A10a), Down and Back (DnB), A02m and A02n. Lastly,
298 sensory neurons are also connected to several projection neurons including A09e, A10j, A09o,
299 TePn04 and TePn05. Synaptic connectivity data was extracted from Neurophyla LMB
300 Cambridge. (https://neurophyla.mrc-lmb.cam.ac.uk/). (**B-C**) Calcium imaging of sensory
301 neurons including chordotonal (IAV^{GAL4}), class III md ($19\text{-}12^{GAL4}$) and class IV md (ppk^{GAL4})
302 neurons using CaMPARI2. There were three conditions for sensory neurons: No
303 photoconversion (PC) control (no stimulus and no photoconversion), photoconversion control
304 (photoconversion and no stimulus) and stimulus (Stim) condition (photoconversion and 6°C
305 stimulus). CaMPARI2 data are reported area normalized intensity ratios for F_{red}/F_{green} (mean ±
306 SEM). Average N for each cell type and each condition is n=32. (**B**) CaMPARI2 response
307 measured at the cell body for each neuron type. (**C**) Sholl intensity analysis performed using
308 custom FIJI scripts. CaMPARI2 response is measured radially away from the center of the soma.
309 (**D-E**) Cold-evoked responses of third instar *Drosophila* larva. Sensory neurons Ch, CIII md or
310 CIV md neurons were silenced by inhibiting neurotransmitter release via cell type specific
311 expression of tetanus toxin (TNT). (**D**) Instantaneous %CT over time. Heatmap on top represents
312 change in temperature over time. (**E**) Cumulative %CT response for a duration of 5 seconds.
313 Controls include *w1118* and $Empty^{GAL4}>TNT$. Significant stars: turquoise stars represent
314 comparison to *w1118* and purple stars represent comparison to $Empty^{GAL4}>TNT$. Average n=72.
315 (**F-G**) Neural activation of sensory neurons via cell type specific expression of ChETA relative
316 to $Empty^{GAL4}>ChETA$ control. $Empty^{GAL4}$ n=35. Ch n=20, CIV n=20. & CIII n=143. (**F**)
317 Instantaneous %CT over time. Blue bar represents optogenetic neural activation. (**G**) Peak %CT.
318 (**H-I**) Neural co-activation of sensory neurons and CIII md neurons. Here each condition
319 represents expression of *ChETA* in CIII md neurons and plus Ch (via *IAV-GAL4*), CIII (via
320 $R83B04^{GAL4}$) or CIV md neurons (via ppk^{GAL4}). (**H**) Instantaneous %CT over time. Blue bar
321 represents optogenetic neural activation. (**I**) Peak %CT response during optogenetic stimulation.
322 CIII n=143 and average experimental n=50 Significant differences indicated via asterisks, where
323 *p<0.05, ***p<0.001, and ****p<0.0001.
324
325
326
327
328

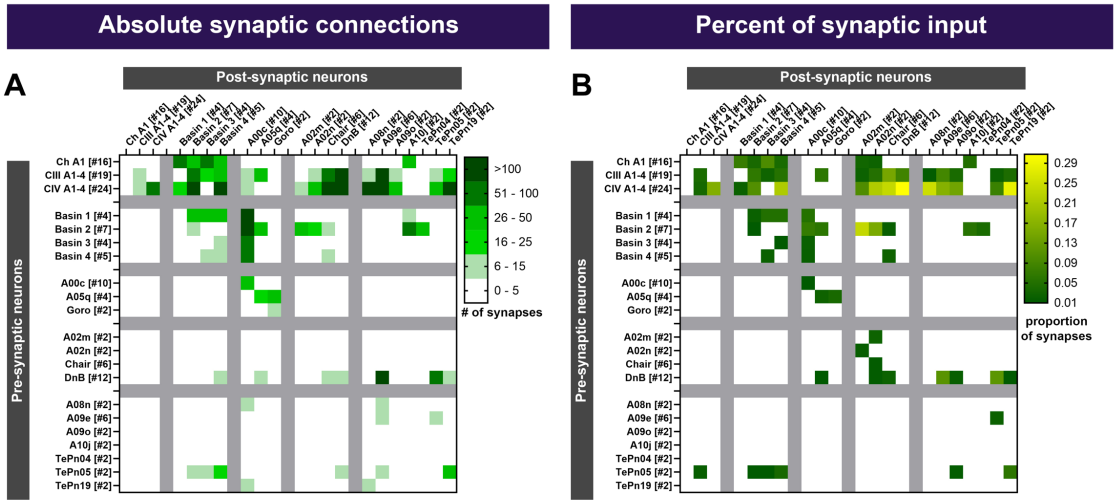

Figure 1-figure supplement 1: Sensory neuron connectivity matrix.
Synaptic connectivity matrix for neurons whose role in cold nociception was assessed. The number in brackets indicates the total number of neurons analyzed for each cell-type. (**A**) Absolute number of synaptic connections between pre- and post-synaptic neurons. (**B**) Connectivity represented as proportion of synaptic input to the post-synaptic neurons.

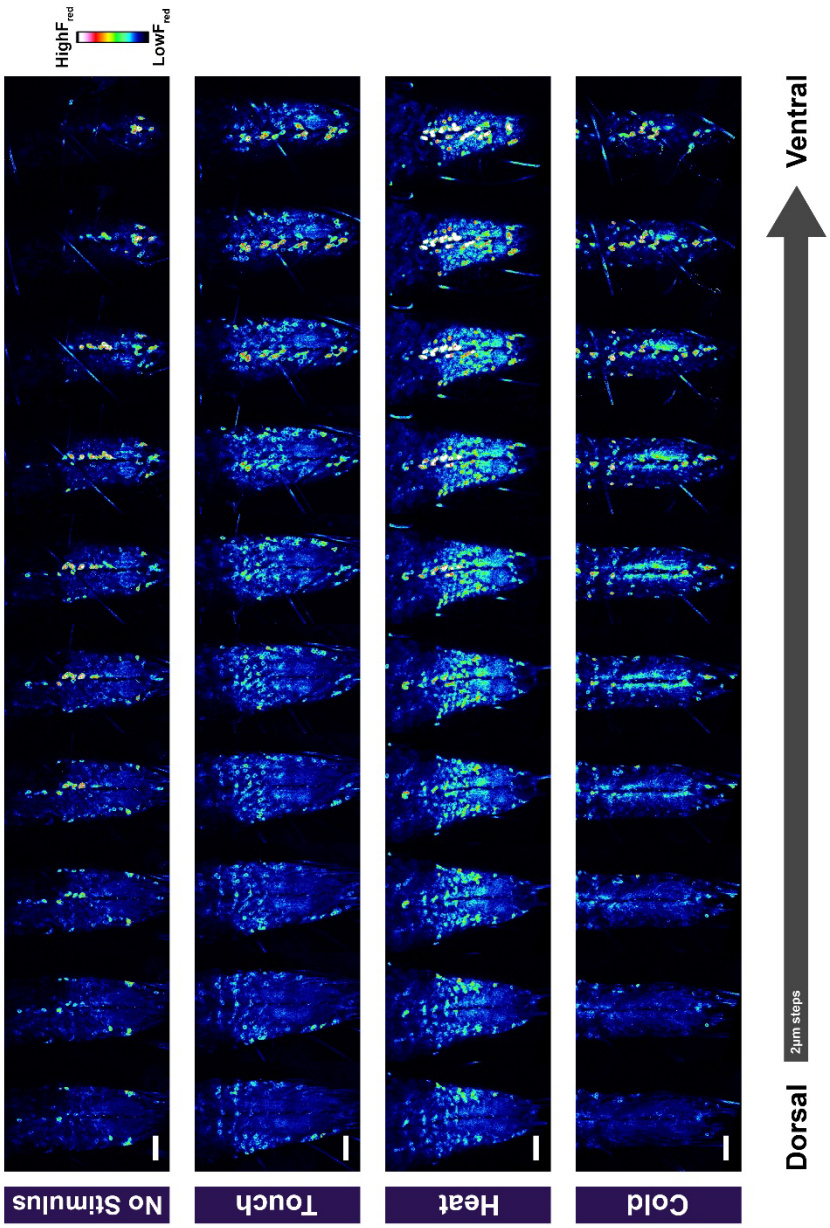

Figure 1-figure supplement 2: Stimulus evoked calcium responses of *Drosophila* larval ventral nerve cord.

Representative images of *Drosophila* larval *in vivo* intact animal ventral nerve cord calcium responses assessed via pan-neural CaMPARI expression. Freely moving larvae were exposed innocuous touch, noxious heat (45°C) or noxious cold (6°C) stimulus for 20 seconds and simultaneously exposed to 20 seconds of photo-converting light. Z-stacks of ventral nerve cord are shown with 2µm steps. Briefly, all animals were from the same batch, imaging was conducted using the same settings, and larvae were exposed to same levels of photo-converting light. For better visualization, only photoconverted red CaMPARI fluorescence is reported, and

346 images were pseudo-colored for enhancing signal-to-noise ratio, where highest intensity
347 represented as white and lowest intensity with dark blue. Scale bar represents 50µm.
348

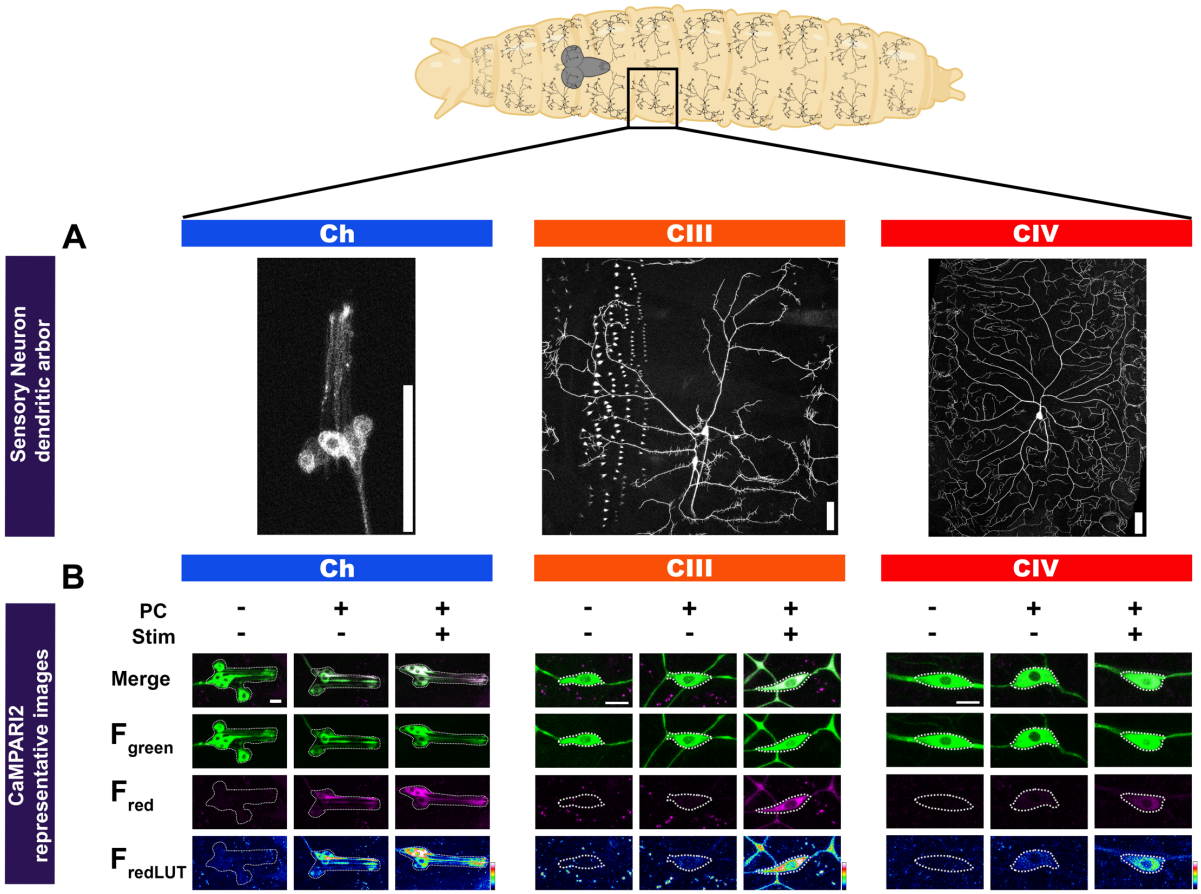

349
350
351 **Figure 1-figure supplement 3: Somatosensory neural dendritic morphology and**
352 **representative images of sensory neurons expressing CaMPARI2.**
353 (**A**) Representative images of somatosensory neurons (Ch, CIII md and CIV md). Note, all
354 images have separate magnification. Each image's scale bar represents 50µm. Drosophila larva
355 and larval brain graphic was created with BioRender.com. (**B**) Confocal images of chordotonal
356 (Ch: IAV^{GAL4}), class III md (CIII: $19\text{-}12^{GAL4}$) and class IV md (CIV: ppk^{GAL4}) neurons expressing
357 CaMPARI2. There were three conditions for sensory neurons: No photoconversion control (no
358 stimulus (Stim) and no photoconversion (PC)), photoconversion control (photoconversion and no
359 stimulus) and stimulus condition (photoconversion and 6°C stimulus). Top row shows merge of
360 F_{red} and F_{green}, second row is F_{green}, third row is F_{red} and last row contains F_{redLUT}, which is
361 pseudo-colored with highest intensity being white and lowest intensity being dark blue (color
362 scale bar on bottom right). Cell body and dendrites are outlined in white for Ch and cell body are
363 outline in white for CIII and CIV neurons. Scale bar represents 10µm.

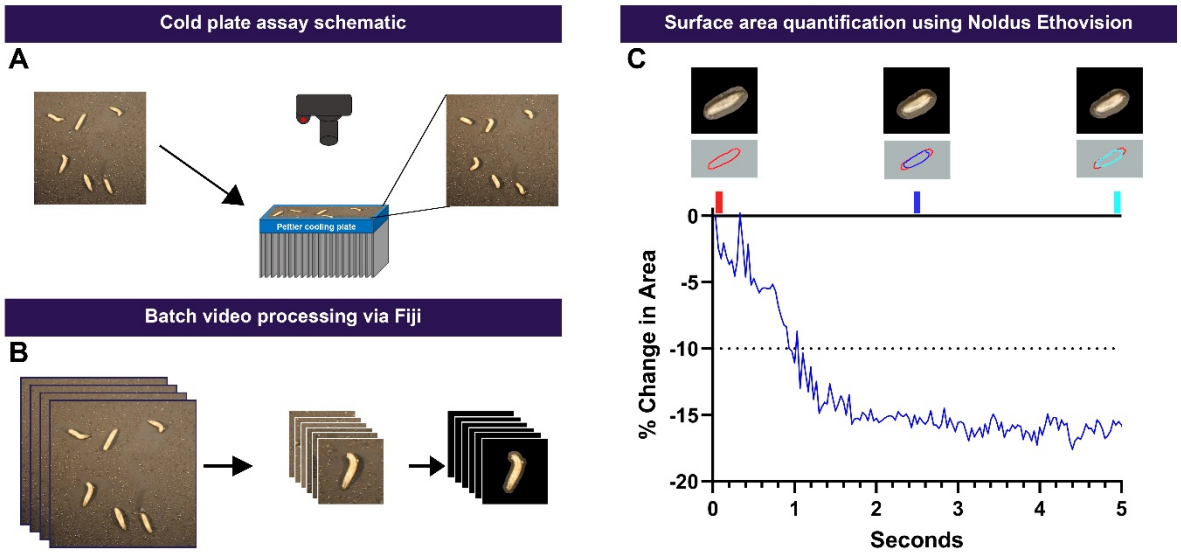

Figure 1-figure supplement 4: *Drosophila* larval cold plate assay and quantitative analysis. (**A**) A schematic of cold plate assay. Briefly, 3rd instar *Drosophila* larvae are plated on a thin metal plate, then we expose the larvae to noxious temperature by transferring the plate onto pre-chilled Peltier cold plate. (**B**) Behavior videos are automatically processed using custom macros in Fiji, where behavioral videos are cropped, and background is removed to improve quantitative analysis. (**C**) Larval surface is area is measured using Noldus Ethovision. The following larval cold evoked contraction (CT) behavioral metrics are calculated using r: Instantaneous CT%, cumulative CT%, CT duration and CT magnitude. We define CT behavioral response as a reduction in surface area less than -10%.

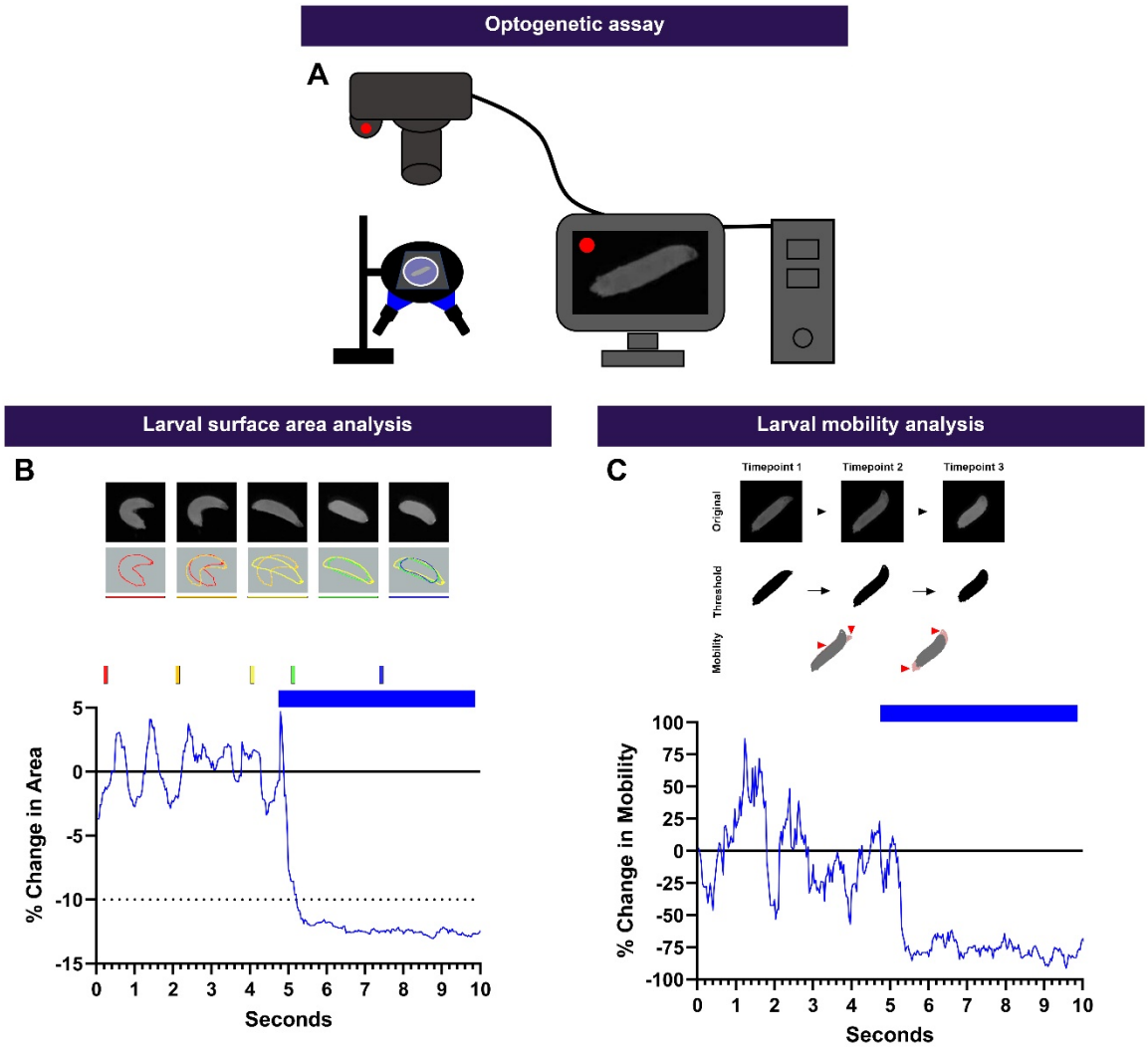

Figure 1-figure supplement 5: *Drosophila* larval neural activation assays using optogenetics. To perform neural activation experiments, we created a custom built optogenetic experimental setup, which has a very high spatial resolution and signal to noise ratio by using principles of dark field illumination. (**A**) Schematic of custom optogenetic rig, where stimulus and video recording are controlled via computer using Noldus Ehtovision. Individual *Drosophila* larva are plated on clear glass plate and illuminated from below with white light. Neuron activating blue light is also delivered from the below. Individual behavioral videos are automatically cropped and stabilized using custom Fiji macros. (**B-C**) We measured to two variables *Drosophila* larval surface area and mobility. (**B**) Top, image stills from various timepoints before and during optogenetic stimulation of cold sensitive CIII md neurons resulting in contraction (CT) behavioral response. Bottom, percent change in area over time of an individual animal. During baseline, larval locomotion and turns results brief changes in surface

area (±2-4%). Whereas upon neural stimulation, there is a distinct lasting reduction in surface area of less than -10%. (**C**) Larval mobility refers to changes in larval postures as measured by changes in occupied space. Since the amount of larval mobility is a function of various intrinsic and extrinsic factors, we normalized larval mobility to baseline period, where there was no neural activation. Top, conceptual framework of how larval mobility is measured. Original videos are motion stabilized in the XY axis and thresholded. Next, we perform image calculations (Mobility=$\text{Frame}_{\text{timepoint 2}} - \text{Frame}_{\text{timepoint 1}}$) to get just the red shaded portions denoting changes in postural locations (red arrowheads). *Drosophila* larval time series mobility data are reported as percent change in mobility, time spent being immobile and percent of immobile animals, or for a genotype percent of animals that are immobile over time, immobility is defined as -25% or more reduction in mobility.

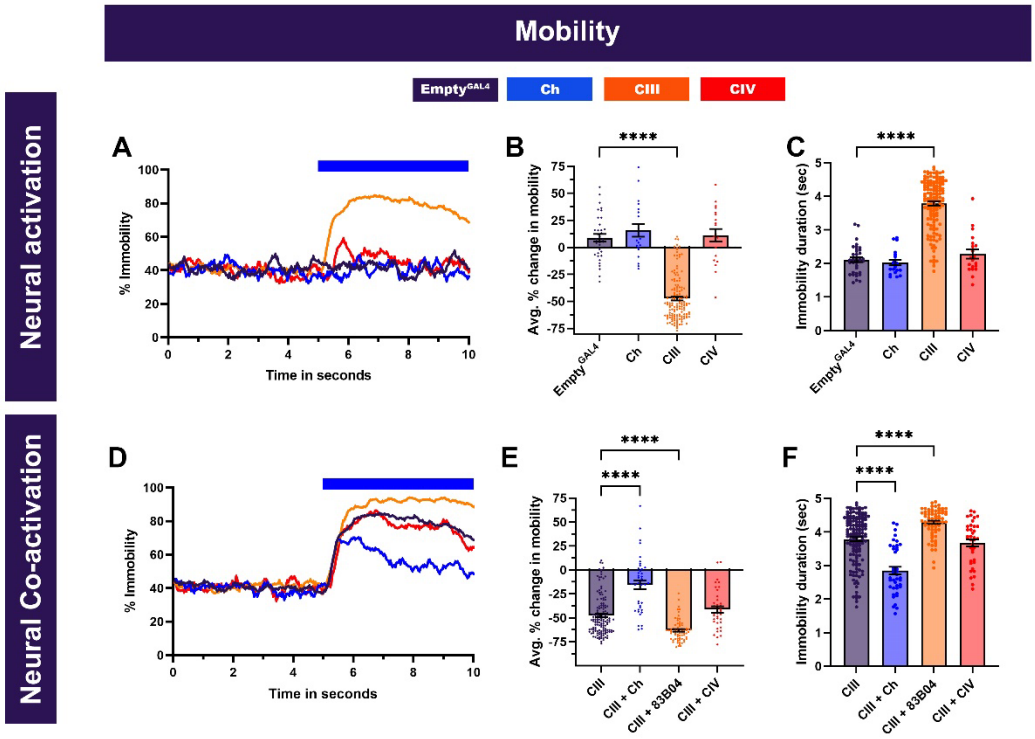

Figure 1-figure supplement 6: *Drosophila* larval mobility pipeline and effects of neural activation and co-activation of sensory neurons on larval mobility (**A-F**) *Drosophila* larval mobility following somatosensory neuron optogenetic activation (**A-C**) and CIII md neuron plus co-activation of Ch, additional CIII *GAL4* driver (*R83B04*^{GAL4}) or CIV md neurons (**D-F**). (**A, D**) Instantaneous percent immobility. Blue bar represents optogenetic neural activation. (**B, E**) Average percent change in mobility for each genotype, where greater percent immobility results in larger changes in average mobility. (**C, F**) Immobility duration in seconds during stimulation.

420 Neural activation: *Empty*^{GAL4} n=35. Ch n=20, CIV n=20. & CIII n=143. Neural co-activation:
421 CIII n=143 and average experimental n=50.Significant differences indicated via asterisks, where
422 ****p<0.0001.
423
424
425 **Multisensory integrators are required and facilitate cold nociception**
426
427 Basin interneurons function as multisensory integrators receiving convergent inputs from
428 mechano-, chemo- and thermo-sensitive peripheral sensory neurons (**Figure 2A, Figure 2-figure**
429 **supplement 1A**). Previous behavioral and functional studies have revealed that Basin
430 interneurons are required for nociceptive escape responses mediated by Ch and CIV md neurons
431 (Ohyama et al., 2015). Both Ch and CIV md neurons play roles in CIII md mediated behavioral
432 responses either in cold nociception and/or can detect cold stimuli. We hypothesized that Basin
433 interneuron function is required downstream of cold nociceptive somatosensory neurons. We
434 evaluated whether Basin interneurons are necessary and sufficient for cold nociception, exhibit
435 cold evoked increases in calcium response and function downstream of CIII md neurons.
436
437 <u>Silencing Basin interneurons reduces cold-evoked CT</u>
438 Basin interneurons receive somatosensory cues from CIII md neurons, thus we predicted
439 that inhibiting neurotransmitter release from Basin neurons will result in impaired cold evoked
440 behaviors (**Figure 2A**). We assessed the requirement of all Basin neurons using "pan-" Basin
441 driver lines and also assessed roles of individual Basin neurons using subtype specific driver
442 lines. Neural silencing of all Basin (1-4) neurons, using two independent driver lines
443 (*R72F11*^{GAL4} and *R57F07*^{GAL4}), led to significant reductions in cold-evoked CT responses
444 compared to genetic background (*w1118*) and *Empty*^{GAL4} controls (**Figure 2B**). *Drosophila*
445 larvae with impaired Basin (1-4) neuronal function had significant reductions in CT duration,
446 magnitude and cumulative %CT response compared to controls (**Figure 2C-E**). CIII neurons
447 have differential connectivity to individual Basin subtypes (**Figure 2A**). Therefore, we assessed
448 requirement of Basin-1, -2 or -4 neurons, for which there are previously validated independent
449 driver lines (Jovanic et al., 2016; Ohyama et al., 2015). Tetanus toxin mediated neural silencing
450 of Basin-2 or -4 led to significant reductions in cold evoked CT response, as measured by
451 cumulative %CT response, CT duration and CT magnitude, compared to controls (**Figure 2B-E**).
452 CIII md neurons do not synapse onto Basin-1 neurons according to the EM-mapped connectome
453 (**Figure 2A**) (Masson et al., 2020), however, Basin-1 & -2 neurons share synaptic connectivity to
454 both feedback and feedforward GABAergic interneurons, both of which are downstream of
455 sensory neurons (Jovanic et al., 2016). Furthermore, Basin-1 neural activation leads to
456 depolarizations in Basin-2 through GABAergic disinhibitory pathway (Jovanic et al., 2016).
457 Therefore, we expected that inhibiting neurotransmitter release in Basin-1 neurons would result
458 in reduced cold-evoked responses. Neural silencing of Basin-1 neurons resulted in modest, but
459 significant reductions in cold evoked responses (**Figure 2B-E**). Impaired Basin neuron signaling

460 results in at least 25% reduction in cold evoked responses with the strongest reductions for all-
461 Basin, Basin-2 or Basin-4 driver lines (**Figure 2J**).
462
463 Co-activation of Basin interneurons and CIII md somatosensory neurons enhances CT
464 Next, we evaluated whether neural activation of Basin neurons would impair or elicit a
465 CT response. Optogenetic activation of Basin neurons, either using all Basin or individual Basin
466 driver lines, did not elicit a CT response (**Figure 2-figure supplement 2**). But the simultaneous
467 co-activation of CIII md and Basin neurons led to sustained increases in CT responses compared
468 to controls, where only CIII md neurons were activated, across multiple behavioral metrics
469 (**Figure 2F-I**). Coactivation did not result in a change in larval immobility (**Figure 2-figure**
470 **supplement 1B-D**), whereas activation of all Basins led to significantly greater immobility
471 (**Figure 2-figure supplement 1B-D**). These results indicate that Basin neurons are not sufficient
472 for the CT response, but that the combined activation of CIII md and Basins not only suffices but
473 also elicits an even stronger CT response than activating CIII md neurons alone.
474 To parse the contribution of individual Basin neuronal subtypes, we next assessed the
475 role of Basin-1, -2 or -4, and all four Basin together, in either facilitating or suppressing CT
476 responses using our co-activation paradigm (**Figure 2F-I**). Co-activation of Basin-1 or Basin -2
477 with CIII md neurons led to an enhanced CT response compared to controls across all measures
478 of behavioral response including instantaneous %CT response, peak %CT response, CT duration
479 and CT magnitude (**Figure 2F-I**), with a subsequent significant increase in larval immobility
480 (**Figure 2-figure supplement 1B-D**). Basin-2 plus CIII md neuron co-activation led to strong
481 facilitation of CT responses, but surprisingly resulted in significantly reduced immobility
482 (**Figure 2-figure supplement 1B-D**). Unlike for all other Basin neurons tested, Basin-4 and CIII
483 md neuron co-activation led to a suppression of CT response, where peak instantaneous %CT
484 response was similar to controls, however, there was a rapid reduction in instantaneous %CT
485 response compared to controls (**Figure 2F-I**). Both CT duration and CT magnitude were
486 significantly impaired for Basin-4 plus CIII md neuron co-activation compared to controls
487 (**Figure 2H, I**), which also showed significantly lower immobility (**Figure 2-figure supplement**
488 **1B-D**). Interestingly, dual activation of CIII md and all Basin neurons led to weaker CT
489 enhancement compared to co-activation of either Basin-1 or -2 coupled with CIII md neurons
490 (**Figure 2J**), consistent with the finding that co-activation with Basin-4 reduced the CT response.
491 Collectively, second-order Basin neurons are required for cold evoked responses and specifically
492 Basin-1 and Basin-2 are able to enhance CIII md neuron evoked behavioral responses.
493
494 CaMPARI reveals Basin-2- and Basin-4 are activated in CT responses
495 To further explore how Basin interneurons function in cold nociception, we sought to
496 investigate cold-evoked Ca^{2+} responses of Basin neurons. Since somatosensory neurons are
497 cholinergic (Salvaterra & Kitamoto, 2001), we expected that Basin neurons postsynaptic to CIII
498 md neurons will exhibit cold-evoked increases in Ca^{2+}. Post-hoc imaging of evoked CaMPARI2
499 fluorescence revealed that Basin neurons have significantly higher F_{red}/F_{green} ratios compared to

500 their respective controls, as assessed by two independent all-Basin driver lines (**Figure 3A, B)**.
501 We further investigated Ca^{2+} responses in greater detail using individual driver lines for Basin-1,
502 -2 or -4. Basin-1 neurons are weakly required for cold-evoked CT responses (**Figure 2J**), and
503 coherently do not exhibit cold-evoked increases in Ca^{2+} response (**Figure 3C)**. In contrast,
504 Basin-2 and -4 neurons both exhibit significant increases in Ca^{2+} responses compared to their
505 respective controls (**Figure 3D-E)**. Collectively, Basin-2 and -4 neuron subtypes that are
506 required for cold-evoked CT responses (**Figure 2J**), also exhibit cold-evoked increases in Ca^{2+}.
507
508 <u>CIII md neurons and Basin-2 and -4 neurons are functionally connected</u>
509 Basin-2 and -4 are postsynaptic to CIII md neurons, are required for cold nociception and
510 have cold-evoked increases in Ca^{2+}. Next, we assessed whether CIII md neurons and Basin-2 or -
511 4 neurons are functionally connected. From the EM-reconstructed connectome we predicted that
512 the activation of CIII md neuron will result in increased Ca^{2+} levels of Basin-2 or -4. As
513 expected, optogenetic activation of CIII md neurons led to significant increases in Ca^{2+} levels in
514 Basin-2 neurons, and repeated stimulation of CIII md neurons did not lead to sensitization of
515 Basin-2 Ca^{2+} responses (**Figure 3F, G)**. Previously, it was shown that Ch and CIII md neurons
516 could elicit Ca^{2+} response in Basin-4 neurons (Kaneko et al., 2017), however, in this previous
517 study the authors were unable to determine which of the two sensory neuron cell types led to
518 increases in the Basin-4 Ca^{2+} response (Kaneko et al., 2017). Here, we show that upon
519 specifically activating CIII md neurons, Basin-4 neurons have large, rapid increases in cytosolic
520 Ca^{2+} followed by quick return to baseline levels. In contrast to Basin-2, Basin-4 neurons showed
521 reduced Ca^{2+} responses upon repetitive activations of CIII md neurons (**Figure 3H, I)**.
522 Therefore, CIII md neuron activation is differentially encoded by Basin-2 and -4 neurons, where
523 Basin-4 neurons have much larger CIII md neuron evoked increase in Ca^{2+} levels but exhibit
524 sensitization compared to Basin-2 neurons, which do not show any sensitization upon repetitive
525 stimulations. Collectively, our data demonstrate that Basin neurons are required for cold-evoked
526 behaviors and Basin-2 and -4 neurons functionally operate downstream of CIII md neurons
527 (**Figure 3-figure supplement 1**).
528
529
530
531
532
533
534
535

536

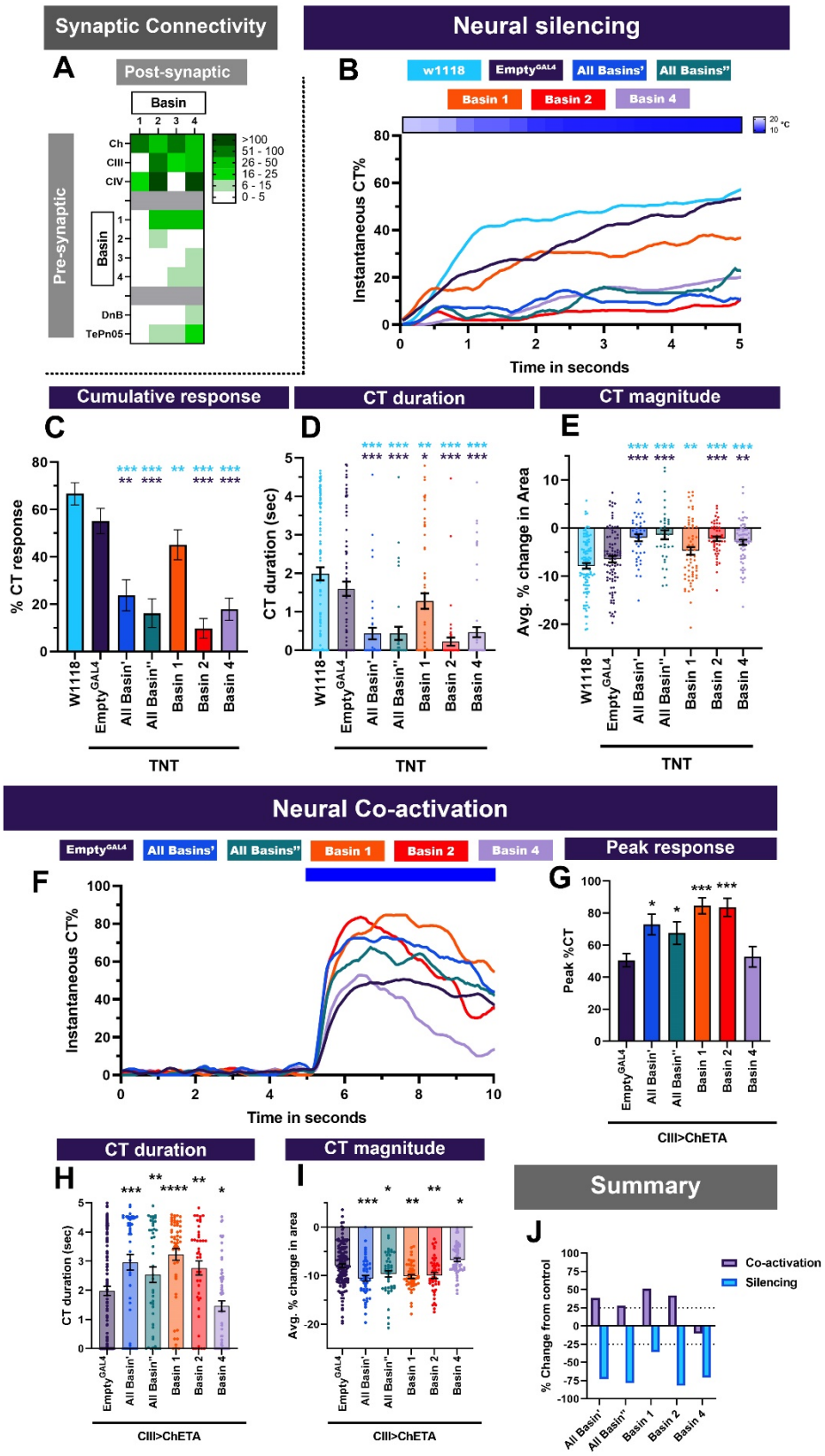
Synaptic Connectivity
Neural silencing
A
Post-synaptic
Basin
Pre-synaptic
Ch
CIII
CIV
DnB
TePn05
>100
51 - 100
26 - 50
16 - 25
6 - 15
0 - 5
B
w1118
Empty^GAL4
All Basins'
All Basins"
Basin 1
Basin 2
Basin 4
Instantaneous CT%
Time in seconds
Cumulative response
CT duration
CT magnitude
C
% CT response
D
CT duration (sec)
E
Avg. % change in Area
W1118
Empty^GAL4
All Basin'
All Basin"
Basin 1
Basin 2
Basin 4
TNT
Neural Co-activation
Peak response
F
G
Peak %CT
CIII>ChETA
CT duration
CT magnitude
H
I
Summary
J
Co-activation
Silencing
% Change from control

537 **Figure 2: Multisensory integrator second order neurons are required for cold-evoked**
538 **behaviors and facilitate CIII-evoked behaviors.**
539 (**A**) Basins (1-4) receive inputs from sensory neurons (Ch, CIII md and CIV md), Basins,
540 premotor neuron Down and Back (DnB) and projection neuron TePn05. Heatmap plot of pre-
541 synaptic connections to Basins. Synaptic connectivity data was extracted from Neurophyla LMB
542 Cambridge. (https://neurophyla.mrc-lmb.cam.ac.uk/). (**B-E**) Cold-evoked responses of third
543 instar *Drosophila*. Basin (1-4) neurons were silenced by inhibiting neurotransmitter release via
544 cell type specific expression of tetanus toxin (TNT), where All Basin' (*R72F11*^{GAL4}), All Basin''
545 (*R57F07*^{GAL4}), Basin-1 (*R20B01*^{GAL4}), Basin-2 (*SS00739*^{splitGAL4}) and Basin-4 (*SS00740*^{splitGAL4}).
546 (**B**) Instantaneous %CT over time. Heatmap on top represents change in temperature over time.
547 (**C**) Cumulative %CT response for a duration of 5 seconds. (**D**) CT duration in seconds. (**E**) CT
548 magnitude as average percent change in area for the duration of stimulus. Controls include
549 *w1118* and *Empty*^{GAL4}*>TNT*. Significant stars: turquoise stars represent comparison to *w1118* and
550 purple stars represent comparison to *Empty*^{GAL4}*>TNT*. Average n = 64. (**F-I**) Neural co-activation
551 of Basin neurons and CIII md neurons. Here each condition represents expression of ChETA in
552 CIII md neurons and plus Basin (1-4) neurons. (**F**) Instantaneous %CT over time. Blue bar
553 represents optogenetic neural activation. (**G**) Peak %CT response during optogenetic stimulation.
554 (**H**) CT duration in seconds during optogenetic stimulation. (**I**) CT magnitude as average percent
555 change in area for the duration of stimulus. Significant stars: purple stars represent comparison to
556 CIII md + *Empty*^{GAL4}*>ChETA*. Empty^{GAL4} n=143 and experimental condition average n =49. (**J**)
557 Overall percent change from control for either neural silencing or neural co-activation. The
558 metrics for neural silencing include cumulative %CT, CT magnitude, and CT duration. The
559 following metrics were used to calculate percent for neural co-activation: cumulative %CT, peak
560 %CT, CT duration and magnitude. Significant differences indicated via asterisks, where
561 *p<0.05, **p<0.01, ***p<0.001, and ****p<0.0001.
562
563
564
565
566
567
568
569
570
571
572

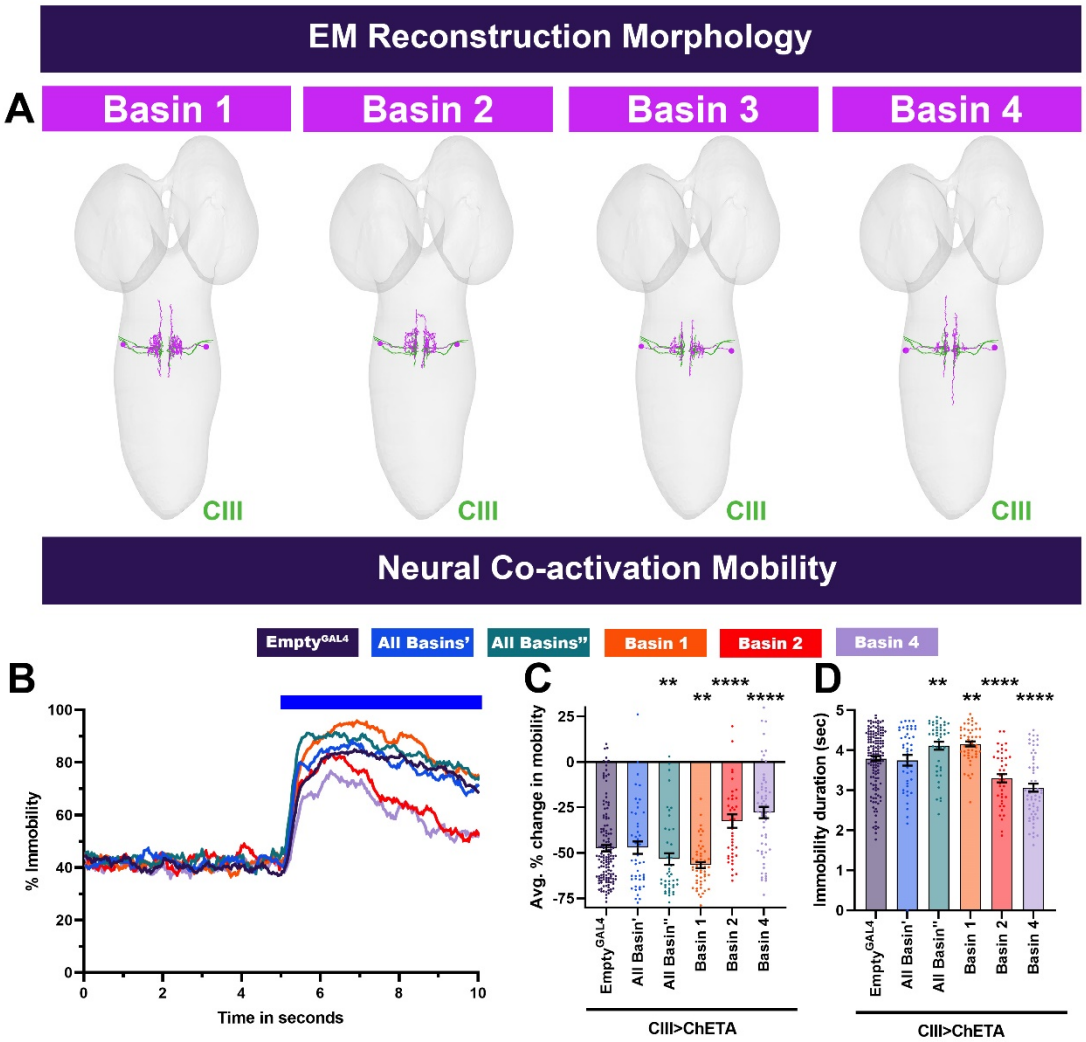

Figure 2-figure supplement 1: Neural reconstructions and larval mobility for multisensory integrator neurons.

(**A**) Individual Basin neuron subtypes (magenta) and CIII md neuron axons (blue). Neural reconstruction data was extracted from Neurophyla LMB Cambridge. (https://neurophyla.mrc-lmb.cam.ac.uk/). (**B-D**) *Drosophila* larval mobility for Basin plus CIII md neuron optogenetic co-activation. (**B**) Instantaneous percent immobility. Blue bar represents optogenetic neural activation. (**C**) Average percent change in mobility for each genotype, where greater percent immobility results in larger changes in average mobility. (**D**) Immobility duration in seconds during stimulation. *Empty^{GAL4}* n=143 and experimental condition n =49. Comparisons to *CIII md + Empty^{GAL4}>ChETA*. Significant differences indicated via asterisks, where **p<0.01, and ****p<0.0001.

584
585

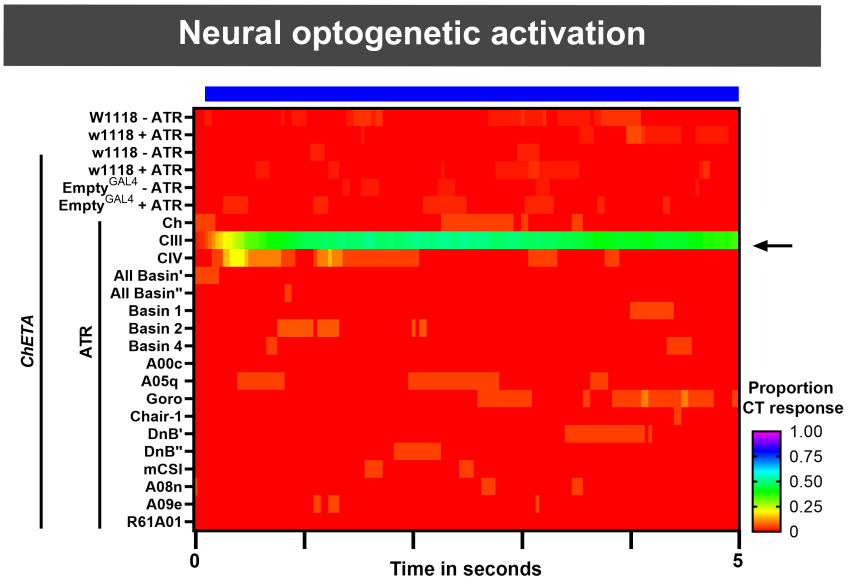

586
587 **Figure 2-figure supplement 2: Optogenetic activation of individual neuronal cell-types.**
588 Heatmap represents optogenetically evoked instantaneous contraction (CT) proportions of
589 *Drosophila* larvae. Individual neuronal cell-types were optogenetically activated using cell-type
590 specific expression of *ChETA*. Black arrow indicates optogenetic activation of primary cold
591 somatosensory CIII md neurons, which are the only the genotype with high proportions CT.
592 Average n= 31.
593
594
595
596
597
598
599
600
601
602
603
604
605

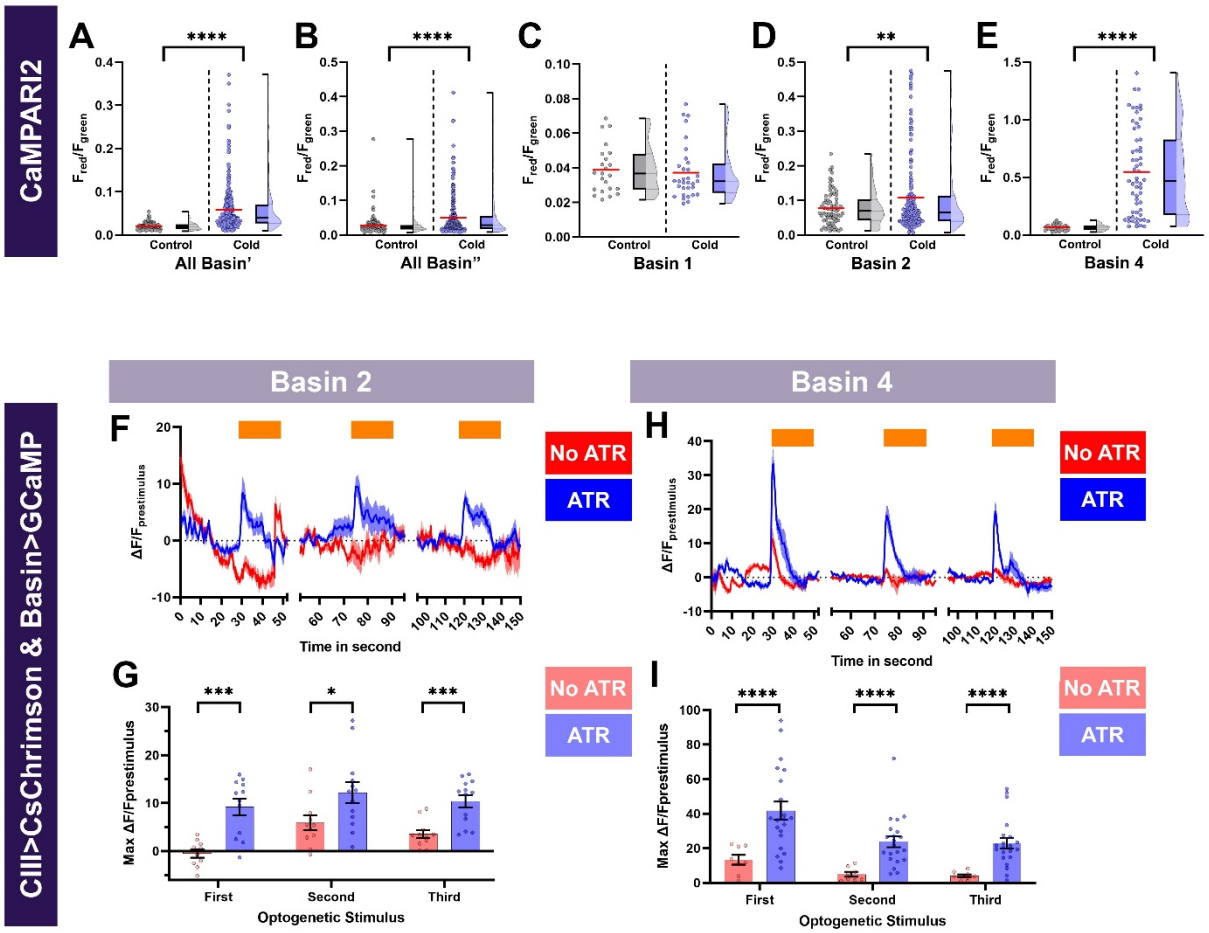

Figure 3: Cold- and CIII- evoked calcium responses of Basin neurons.
(**A-E**) Ca^{2+} responses of Basin neurons upon cold exposure vs. controls (room temperature). Neural responses (CaMPARI2) of Basin neuron cell bodies were analyzed using the following cell type driver lines (**A**) All Basin' (*R72F11*^{GAL4}) average n=197, (**B**) All Basin'' (*R57F07*^{GAL4}) average n = 182, (**C**) Basin-1 (*R20B01*^{GAL4}) average n=27, (**D**) Basin-2 (*SS00739*^{splitGAL4}) average n=119 and (**E**) Basin-4 (*SS00740*^{splitGAL4}) average n=46. CaMPARI2 fluorescence ratio is reported as F_{red}/F_{green}. We report the data as individual datapoints, where the red line represents mean, and hybrid plots (boxplot & violin) for visualizing the distribution and quartiles of data. Significant stars represent $p<0.05$, where comparisons were made to their respective no stimulus controls. (**F-I**) To functionally assess CIII md neuron to Basin-2 or Basin-4 connectivity, we optogenetically activated CIII md neurons (*83B04*^{lexA}*>CsChrimson*) and visualized changes in evoked Ca^{2+} using *Basin-2*^{splitGAL4} or *Basin-4*^{splitGAL4}*>GCaMP6m*. Control: No all *trans*-retinal (ATR) supplemented diet, which is required for optogenetic stimulation in *Drosophila*. Orange bars indicate optogenetic stimulation. (**F,H**) Basin-2 and Basin-4 changes in GCaMP reported as $\Delta F/F_{prestimulus}$, where prestimulus refers to 15 seconds prior to optogenetic stimulation. (**G,I**) Maximum Basin-2 and Basin-4 neuronal responses ($\Delta F/F_{prestimulus}$) upon optogenetic stimulation.

Average n for each genotype was 13. Comparisons made to relevant controls and significant differences indicated via asterisks, where *p<0.05, **p<0.01, ***p<0.001, and ****p<0.0001.

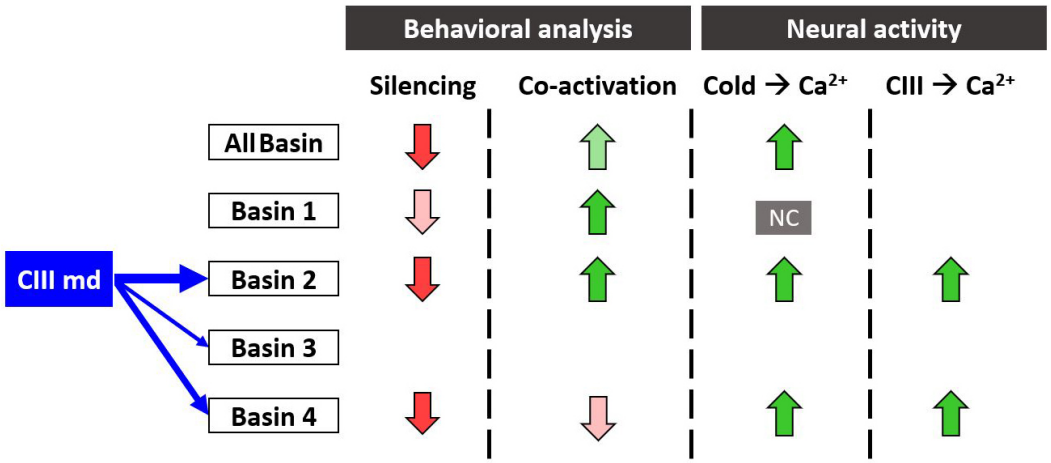

Figure 3-figure supplement 1: Summary of behavioral and functional roles of multisensory integrators in cold nociception.
Blue arrows indicate strength of synaptic connectivity between the CIII md neurons and second order neurons. In behavioral analysis column, the arrow direction indicates reduction or enhancement of CT response and shading indicates magnitude of change from control. In neural activity column: NC denotes no significant change in Ca^{2+} response, the arrow direction indicates reduction or enhancement in evoked Ca^{2+} response and shading indicates magnitude of change from control. Empty spaces indicate experimental analyses were not performed.

Multisensory integrators function independently of Goro pathway for cold nociception

Basin neurons innervate a set of projection neurons (A05q and A00c), which are upstream of a command neuron (Goro) that is responsible for initiating CIV md neuron-mediated nociceptive escape behaviors (**Figure 4A, Figure 4-figure supplement 1A**) (Ohyama et al., 2015). We set out to test whether cold-evoked behavioral responses mediated by CIII md and Basin neurons function through A00c, A05q, and/or Goro neurons. We first assessed whether these neurons are required for cold-evoked behavioral responses (**Figure 4B-E**). Neural silencing of A05q neurons via tetanus toxin led to mild, yet significant reductions in cold evoked responses, when compared to *w1118* genetic control (**Figure 4B-E**). Neural silencing of A00c neurons resulted in significantly lower cold-evoked cumulative CT response compared to *w1118* (**Figure 4B, C**). There were also significant reductions in CT duration and CT magnitude when A00c neurons were silenced compared to both controls (**Figure 4D, E**). In contrast, the Goro command neuron for nociceptive rolling behavior is not required for cold-evoked CT responses (**Figure 4B-E**). Next, we assessed whether neural activation of these neurons led to evoked CT responses. Like Basin neurons, single cell-type activation of A00c, A05q, or Goro neurons did

650 not lead to CT behavior (**Figure 2-figure supplement 2**). Similarly, optogenetic co-activation of
651 CIII md neurons and A05q or Goro neurons did not lead to significant facilitation of the CT
652 response (**Figure 4F-I**). However, simultaneously co-activating A00c and CIII md neurons led to
653 significant increases in CT duration and CT magnitude (**Figure 4H, I**). There were no changes in
654 *Drosophila* larval immobility upon co-activation of CIII md plus A00c, A05q or Goro neurons
655 (**Figure 4 - figure supplement 1B-D**). Only co-activation of A00c neurons leads to notable
656 enhancement of CIII md mediated CT response, whereas neural silencing of A00c or A05q
657 neurons led to greater than 25% impairment in cold evoked behavioral responses (**Figure 4J**). In
658 conclusion, the Basin to Goro polysynaptic pathway does not significantly contribute to the cold-
659 evoked CT response.

660

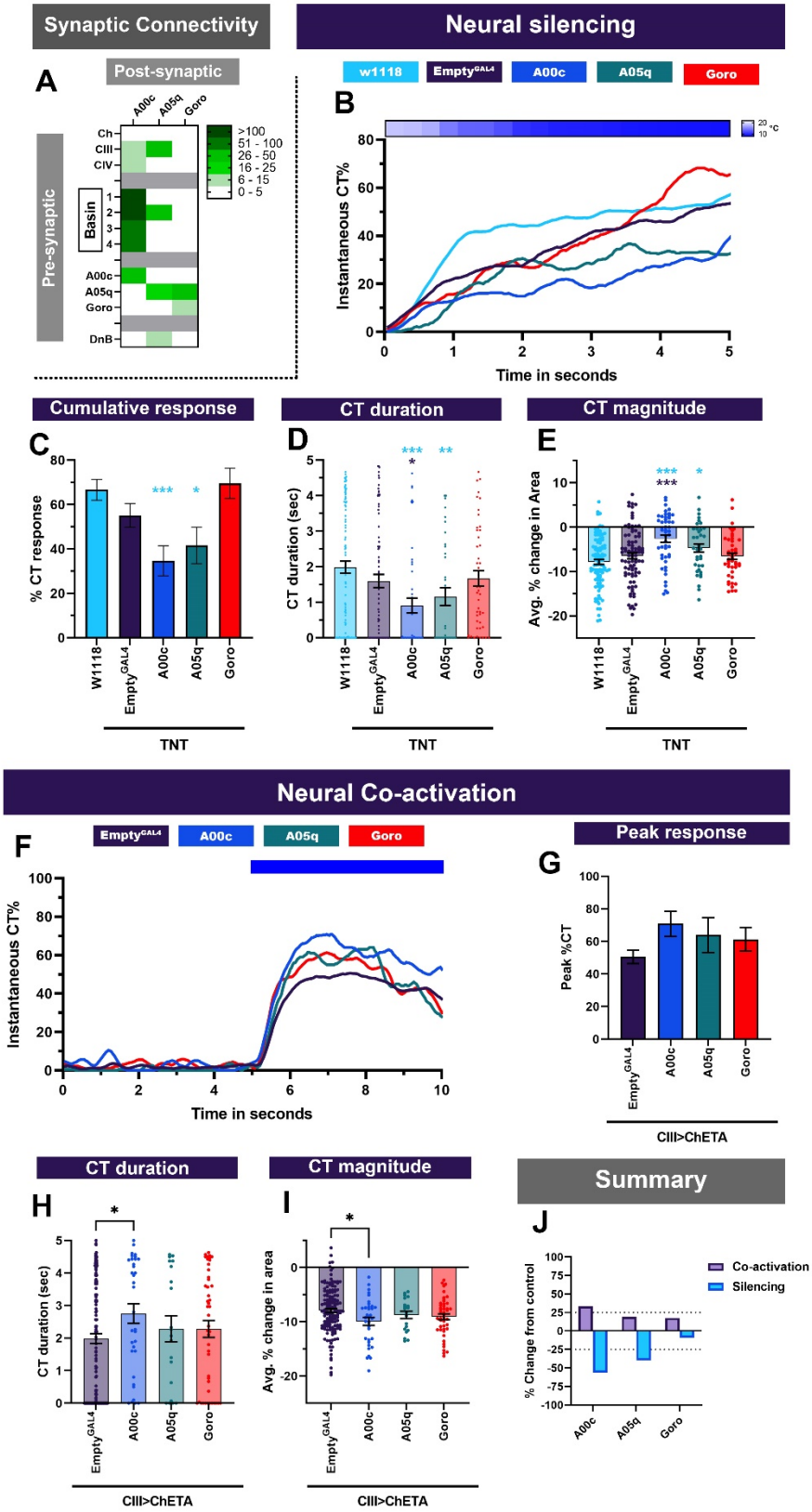
Synaptic Connectivity
Neural silencing
A
Post-synaptic
Pre-synaptic
A00c
A05q
Goro
Ch
CIII
CIV
Basin
1
2
3
4
DnB
>100
51 - 100
26 - 50
16 - 25
6 - 15
0 - 5
B
w1118
Empty^GAL4
A00c
A05q
Goro
Instantaneous CT%
Time in seconds
Cumulative response
CT duration
CT magnitude
C
% CT response
D
CT duration (sec)
E
Avg. % change in Area
W1118
Empty^GAL4
A00c
A05q
Goro
TNT
Neural Co-activation
F
Empty^GAL4
A00c
A05q
Goro
Instantaneous CT%
Time in seconds
Peak response
G
Peak %CT
CIII>ChETA
CT duration
H
CT duration (sec)
CT magnitude
I
Avg. % change in area
Summary
J
Co-activation
Silencing
% Change from control

Figure 4: Projection neurons downstream of Basins and sensory neurons function in cold evoked responses.

(**A**) A00c and A05q primarily receive inputs from Basins and premotor neuron Down and Back (DnB). Goro neurons primarily receive inputs from A05q neurons. Heatmap plot of pre-synaptic connections to downstream neurons. Synaptic connectivity data was extracted from Neurophyla LMB Cambridge. (https://neurophyla.mrc-lmb.cam.ac.uk/). (**B-E**) Cold-evoked responses of third instar *Drosophila*. We used cell-type specific driver lines for downstream neurons to drive expression of tetanus toxin (TNT): A00c ($R71A10^{GAL4}$), A05q ($R47D0^{GAL4}$) and Goro ($R69F06^{GAL4}$). (**B**) Instantaneous %CT over time. Heatmap on top represents change in temperature over time. (**C**) Cumulative %CT response for a duration of 5 seconds. (**D**) CT duration in seconds. (**E**) CT magnitude as average percent change in area for the duration of stimulus. Controls include *w1118* and $Empty^{GAL4}>TNT$. For each genotype average n=64. Significant stars: turquoise stars represent comparison to *w1118* and purple stars represent comparison to $Empty^{GAL4}>TNT$. (**F-I**) Neural co-activation of downstream neurons and CIII md neurons. Here each condition represents expression of ChETA in CIII md neurons plus A00c, A05q or Goro neurons. (**F**) Instantaneous %CT over time. Blue bar represents optogenetic neural activation. (**G**) Peak %CT response during optogenetic stimulation. (**H**) CT duration in seconds during optogenetic stimulation. (**I**) CT magnitude as average percent change in area for the duration of stimulus. Significant purple stars represent comparison to *CIII md* + $Empty^{GAL4}>ChETA$. $Empty^{GAL4}$ n=143 and experimental condition average n =33. (**J**) Overall percent change from control for either neural silencing or neural co-activation. The metrics for neural silencing include cumulative %CT, CT magnitude, and CT duration. The following metrics were used to calculate percent for neural co-activation: cumulative %CT, peak %CT, CT duration and magnitude. Significant differences indicated via asterisks, where *$p<0.05$, **$p<0.01$, and ***$p<0.001$.

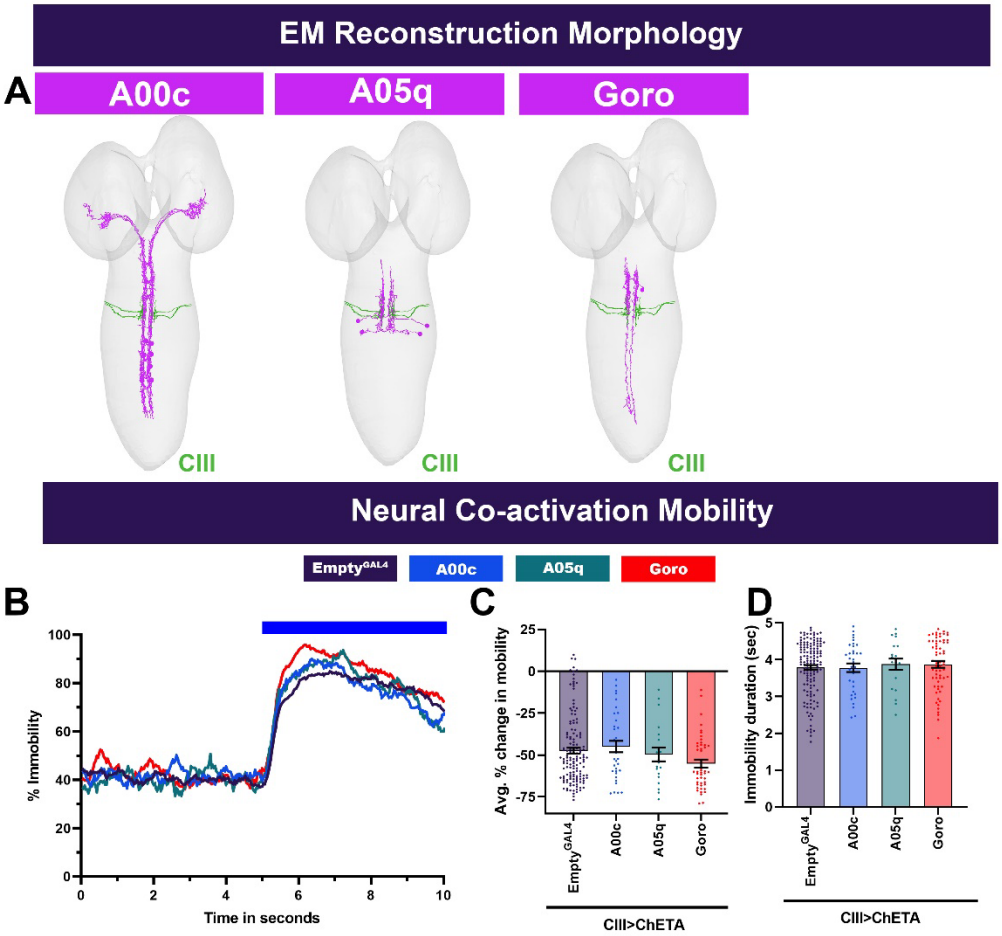

Figure 4-figure supplement 1: Neural reconstructions and larval mobility for A00c, A05q, and Goro neurons.

(**A**) Individual interneuron subtypes (magenta) and CIII md neuron axons (blue). Neural reconstruction data was extracted from Neurophyla LMB Cambridge. (https://neurophyla.mrc-lmb.cam.ac.uk/). (**B-D**) *Drosophila* larval mobility for A00c, A05q or Goro neurons plus CIII md neuron optogenetic coactivation. (**B**) Instantaneous percent immobility. Blue bar represents optogenetic neural activation. (**C**) Average percent change in mobility for each genotype, where greater percent immobility results in larger changes in average mobility. (**D**) Immobility duration in seconds during stimulation. Significant stars represent $p<0.05$, where stars represent comparison to CIII md + *Empty^{GAL4}>ChETA*. Empty^{GAL4} n=143 and experimental condition average n =33.

711 **Premotor neurons function downstream of CIII md neurons to mediate cold nociceptive**
712 **responses**
713
714 Select *Drosophila* larval premotor neurons were previously implicated in CIV-mediated
715 nociceptive escape responses. Specifically, DnB premotor neurons are involved in noxious
716 thermal stimulus-evoked c-bending and rolling behavior (Burgos et al., 2018; Lopez-Bellido et
717 al., 2019). *Drosophila* larvae also roll in response to activation of mCSI premotor neurons, which
718 are synaptically connected to CIV md neurons and predicted to be A02m/n neurons from EM
719 connectomes (Lopez-Bellido et al., 2019; Yoshino et al., 2017). Additionally, Chair-1 (A10a)
720 premotor neurons have been implicated in anemotaxis (Jovanic et al., 2019). Collectively, these
721 premotor neurons primarily receive inputs from both primary sensory neurons (CIII & CIV md)
722 and multisensory integrators (Basin-2 & -4) (**Figure 5A, Figure 5-figure supplement 1A**). We
723 predicted that premotor neurons are required for cold-evoked responses and function
724 downstream of CIII md neurons in a stimulus-specific manner.
725 Inhibition of neural transmission via cell type specific expression of tetanus toxin in
726 individual premotor neurons led to reduced cold evoked responses in *Drosophila* larvae (**Figure**
727 **5B-E**). Silencing Chair-1 neurons resulted in the strongest reduction of cold-evoked CT
728 responses, where instantaneous %CT was the lowest of all premotor neuron subtypes tested
729 (**Figure 5B**). CT duration, magnitude and cumulative percent response were all significantly
730 reduced compared to controls (**Figure 5B-E**). Impairment in Chair-1 neuronal signaling leads to
731 75% reduction from controls in cold-evoked behaviors (**Figure 5J**). We silenced DnB neurons
732 using two independent cell-type specific driver lines (DnB' ($IT4051^{GAL4}$) & DnB''($IT412^{GAL4}$)),
733 where both resulted in reduced instantaneous %CT response, along with significant reductions in
734 CT duration and magnitude compared to controls (**Figure 5B-E**). Silencing mCSI ($R94B10^{GAL4}$)
735 neurons also resulted in significantly reduced cold-evoked CT responses compared to controls
736 (**Figure 5B-E**). DnB or mCSI inhibition of neurotransmitter release leads to approximately 50%
737 reduction in cold-evoked CT responses (**Figure 5J**). Collectively, these premotor neurons are
738 required for cold-evoked behavioral responses.
739 Based on EM connectivity and neural silencing experiments, we predicted that activation
740 of these premotor neurons would be sufficient for *Drosophila* larval CT response. First, we
741 found that activation of premotor neurons alone did not evoke CT response (**Figure 2-figure**
742 **supplement 2**). Next, we performed optogenetic co-activation of CIII md and premotor neuron
743 subtypes. Chair-1 neuron co-activation with CIII md neuron did not have an effect on CT
744 responses (**Figure 5F-I**), however, there was a reduction in larval immobility, where average
745 mobility was increased and duration of immobility was reduced compared to when only CIII md
746 neurons are activated (**Figure 5-figure supplement 1B-D**). Simultaneous activation of CIII md
747 neurons and DnB or mCSI both led to significant increases in CT responses, as measured by
748 peak CT response, CT duration or magnitude, compared to CIII md neuron activation alone
749 (**Figure 5F-I**). DnB and CIII md neuron co-activation led to short lived, subtle but insignificant
750 increases in larval immobility (**Figure 5-figure supplement 1B-D**). Co-activation of mCSI and

751 CIII md neurons resulted in mild reductions in larval immobility (**Figure 5-figure supplement**
752 **1B-D**). These data reveal DnB and mCSI neuronal activity enhances CIII md neuron mediated
753 CT responses.
754 Since these premotor neurons are postsynaptic to CIII md neurons and their activity is
755 required for proper cold evoked behaviors, we predicted that activation of CIII md neurons
756 would elicit cold-evoked increases in Ca^{2+}. To test this prediction, we selectively expressed the
757 Ca^{2+} integrator CaMPARI2 in premotor neurons. Unexpectedly, there was no change in cold
758 evoked Ca^{2+} levels in mCSI or Chair-1 neurons (**Figure 6C-D**). Noxious cold exposure did
759 however lead to significant Ca^{2+} increases in DnB neurons (**Figure 6A-B**). To further assess how
760 CIII md neuronal activity affects DnB function, we optogenetically activated CIII md neurons
761 and assessed evoked Ca^{2+} levels of DnB using GCaMP6. Interestingly, *Drosophila* larvae raised
762 without all *trans*-retinal, a requisite light sensitive cofactor for optogenetic experiments, also had
763 a mild light evoked increase in Ca^{2+} (**Figure 6E, F**). CIII md neuron optogenetic activation led to
764 significant increases in DnB Ca^{2+} levels that slowly returned to baseline levels (**Figure 6E, F**).
765 Upon repeated CIII md neuron activations, DnB neurons exhibit a blunted Ca^{2+} response relative
766 to initial stimulation (**Figure 6E, F**). Taken together we find that premotor neuronal function is
767 required for cold nociception and premotor neuron activity can facilitate CIII md neuron
768 mediated CT responses (**Figure 6-figure supplement 1**).
769
770
771
772
773
774
775
776
777
778
779
780

781

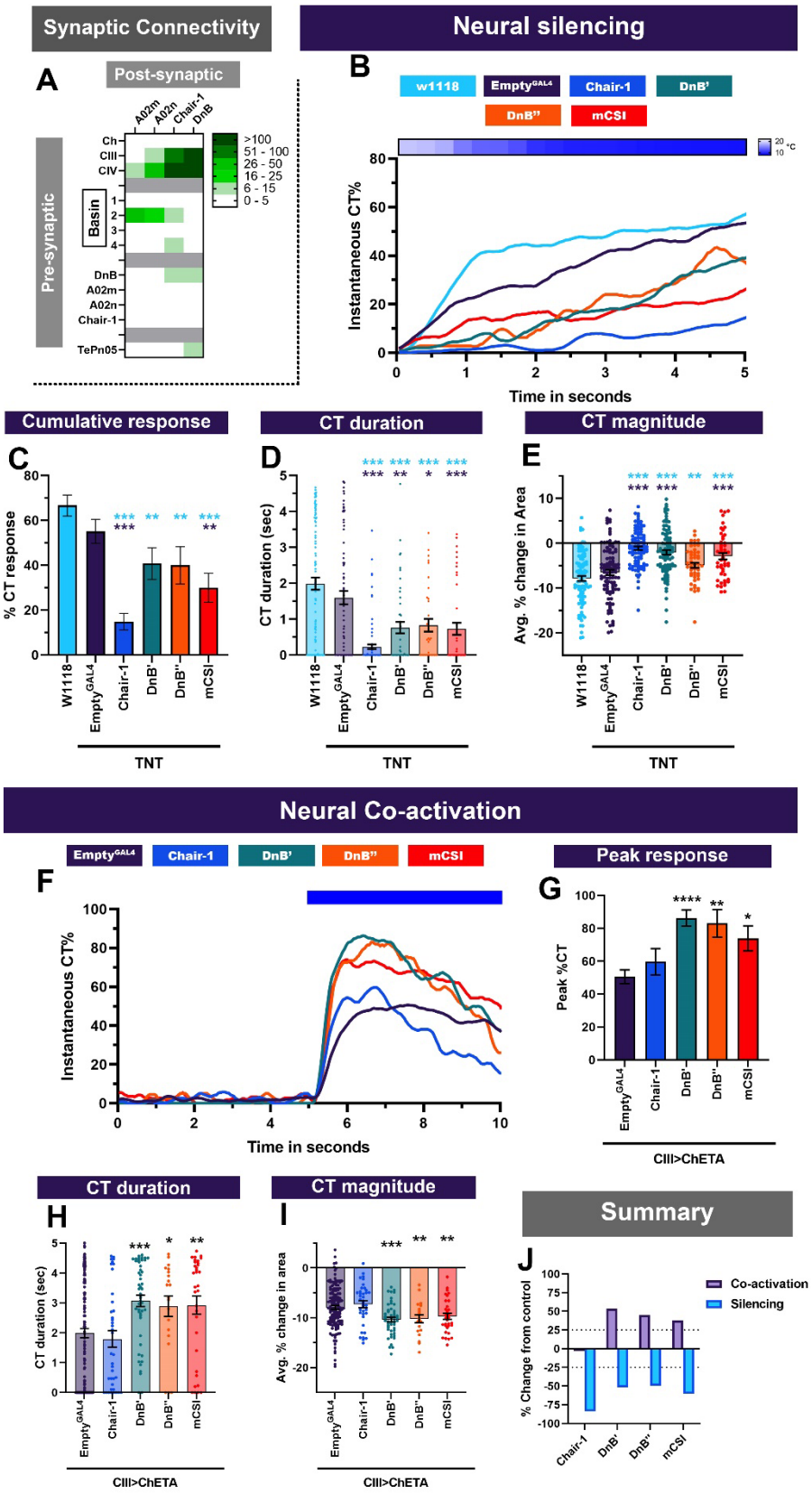
Synaptic Connectivity
Neural silencing
A
Post-synaptic
Pre-synaptic
A02m
A02n
Chair-1
DnB
Ch
CIII
CIV
Basin
1
2
3
4
DnB
A02m
A02n
Chair-1
TePn05
>100
51 - 100
26 - 50
16 - 25
6 - 15
0 - 5
B
w1118
Empty^GAL4
Chair-1
DnB'
DnB''
mCSI
Instantaneous CT%
Time in seconds
Cumulative response
CT duration
CT magnitude
C
% CT response
D
CT duration (sec)
E
Avg. % change in Area
W1118
Empty^GAL4
Chair-1
DnB'
DnB''
mCSI
TNT
Neural Co-activation
F
Instantaneous CT%
Time in seconds
Peak response
G
Peak %CT
CIII>ChETA
CT duration
H
CT duration (sec)
CT magnitude
I
Avg. % change in area
Summary
J
% Change from control
Co-activation
Silencing

Figure 5: Premotor neurons downstream of sensory neurons and Basin neurons are required for cold-evoked responses.

(**A**) Chair-1 (A10a), A02m/n (predicted to be mCSI neurons) and Down and Back (DnB, A09l) primarily receive inputs from Basins, CIII md and CIV md neurons. Heatmap plot of pre-synaptic connections to premotor neurons. Synaptic connectivity data was extracted from Neurophyla LMB Cambridge. (https://neurophyla.mrc-lmb.cam.ac.uk/). (**B-E**) Cold-evoked responses of third instar *Drosophila*. Premotor neurons were silenced by inhibiting neurotransmitter release via cell type specific expression of tetanus toxin (TNT), where Chair-1 (*SS00911*^{splitGAL4}), DnB' (*IT4015*^{GAL4}), DnB'' (*IT412*^{GAL4}) and mCSI (*R94B10*^{GAL4}). (**B**) Instantaneous %CT over time. Heatmap on top represents change in temperature over time. (**C**) Cumulative %CT response for a duration of 5 seconds. (**D**) CT duration in seconds. (**E**) CT magnitude as average percent change in area for the duration of stimulus. Controls include *w1118* and *Empty*^{GAL4}*>TNT*. Average n = 69. Significant stars: turquoise stars represent comparison to *w1118* and purple stars represent comparison to *Empty*^{GAL4}*>TNT*. (**F-I**) Neural co-activation of premotor neurons and CIII md neurons. Here each condition represents expression of ChETA in CIII md neurons plus premotor neurons. (**F**) Instantaneous %CT over time. Blue bar represents optogenetic neural activation. (**G**) Peak %CT response during optogenetic stimulation. (**H**) CT duration in seconds during optogenetic stimulation. (**I**) CT magnitude as average percent change in area for the duration of stimulus. Empty^{GAL4} n=143 and experimental condition average n =35. Significant stars represent $p<0.05$, where purple stars represent comparison to *CIII md + Empty*^{GAL4}*>ChETA*. (**J**) Overall percent change from control for either neural silencing or neural co-activation. The metrics for neural silencing include cumulative %CT, CT magnitude, and CT duration. The following metrics were used to calculate percent for neural co-activation: cumulative %CT, peak %CT, CT duration and magnitude. Significant differences indicated via asterisks, where *$p<0.05$, **$p<0.01$, ***$p<0.001$, and ****$p<0.0001$.

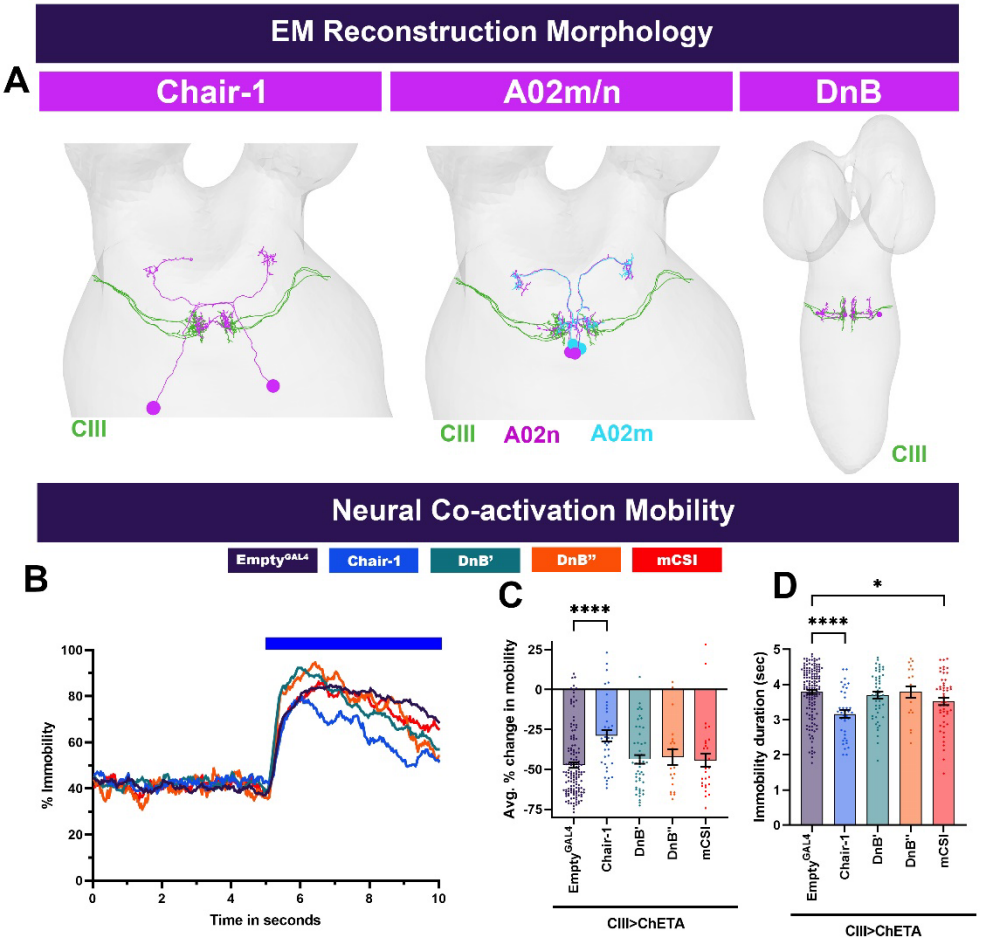

821
822
823 **Figure 5-figure supplement 1: Neural reconstructions and larval mobility for premotor**
824 **neurons.**
825 (**A**) Individual premotor neuron subtypes (magenta/green) and CIII md neuronal axons (blue).
826 Neural reconstruction data was extracted from Neurophyla LMB Cambridge.
827 (https://neurophyla.mrc-lmb.cam.ac.uk/). (**B-D**) *Drosophila* larval mobility observed with
828 premotor neurons plus CIII md neuron optogenetic coactivation. (**B**) Instantaneous percent
829 immobility. Blue bar represents optogenetic neural activation. (**C**) Average percent change in
830 mobility for each genotype, where greater percent immobility results in larger changes in average
831 mobility. (**D**) Immobility duration in seconds during stimulation. *Empty*^{GAL4} n=143 and
832 experimental condition average n =35. Comparison to *CIII md + Empty*^{GAL4}*>ChETA*. Significant
833 differences indicated via asterisks, where *p<0.05, and ****p<0.0001.
834

835

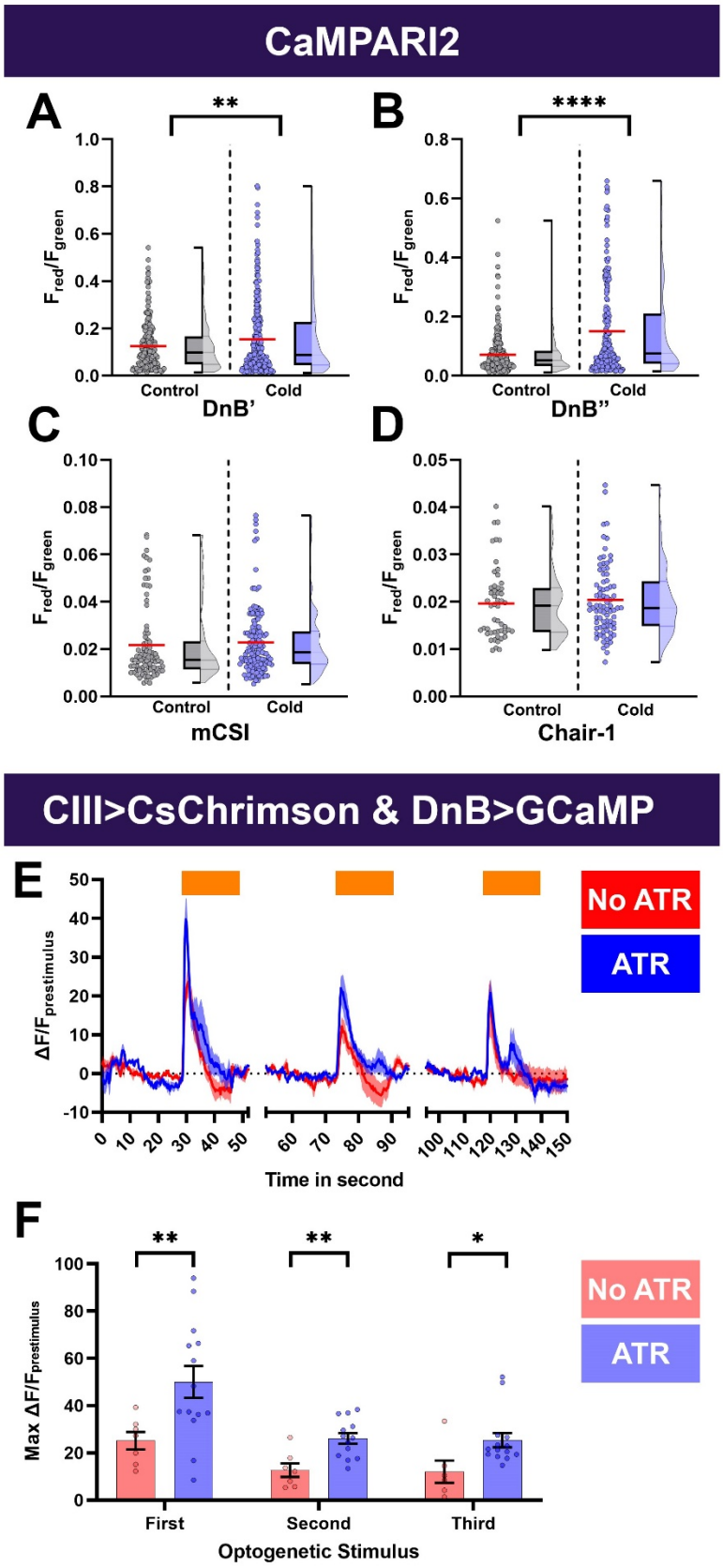
CaMPARI2
A
B
C
D
**
****
Fred/Fgreen
Control
Cold
DnB'
DnB''
mCSI
Chair-1
CIII>CsChrimson & DnB>GCaMP
E
F
No ATR
ATR
ΔF/Fprestimulus
Time in second
Max ΔF/Fprestimulus
First
Second
Third
Optogenetic Stimulus

836 **Figure 6: Cold- and CIII- evoked calcium responses of premotor neurons.**
837 (**A-D**) Ca^{2+} responses of premotor neurons upon cold exposure vs. controls (room temperature).
838 Neural responses (CaMPARI2) of premotor neuron cell bodies were analyzed using the
839 following cell type driver lines DnB' (*IT4015*^{GAL4}) average n=250, (**B**) DnB'' (*IT412*^{GAL4})
840 average n=245, (**C**) mCSI (*R94B10*^{GAL4}) average n=116, and (**D**) Chair-1 (*SS00911*^{GAL4}) DnB'
841 (*IT4015*^{GAL4}) average n=250, (**B**) DnB'' (*IT412*^{GAL4}) average n=245, (**C**) mCSI (*R94B10*^{GAL4})
842 average n=116, and (**D**) Chair-1 (*SS00911*^{splitGAL4}) average n=66. CaMPARI2 fluorescence ratio
843 is reported as F_{red}/F_{green}. We report the data as individual datapoints, where the red line represents
844 mean, and hybrid plots (boxplot & violin) for visualizing the distribution and quartiles of data.
845 Significant stars represent $p<0.05$, where comparisons were made to their respective no stimulus
846 controls. (**E-F**) To functionally assess CIII md neuron to DnB connectivity, we optogenetically
847 activated CIII md neurons (*83B04*^{lexA}*>CsChrimson*) and visualized changes in evoked Ca^{2+} using
848 *DnB-GAL4>GCaMP6m*. Control: No ATR supplemented diet, which is required for optogenetic
849 stimulation in *Drosophila*. Orange bars indicate optogenetic stimulation. (**E**) DnB changes in
850 GCaMP reported as $\Delta F/F_{prestimulus}$, where prestimulus refers to 15 seconds prior to optogenetic
851 stimulation. (**F**) Maximum DnB neuronal responses ($\Delta F/F_{prestimulus}$) upon optogenetic stimulation.
852 Average n=10. Significant differences indicated via asterisks, where *p<0.05, **p<0.01, and
853 ****p<0.0001.
854

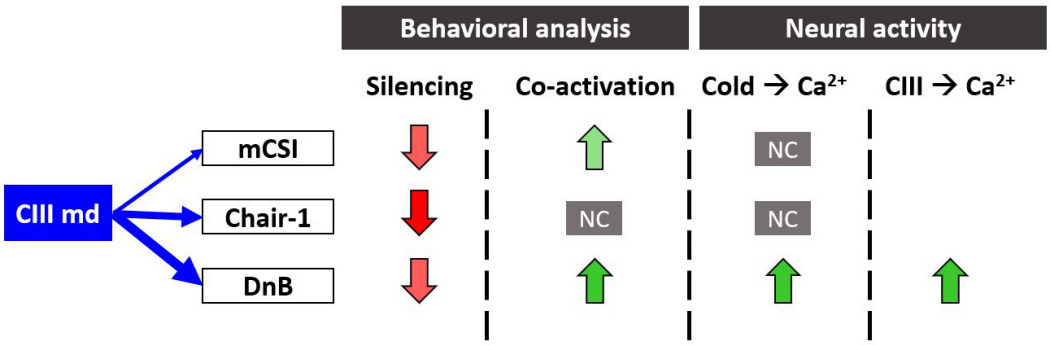

855
856
857
858 **Figure 6-figure supplement 1: Summary of behavioral and functional roles of premotor**
859 **neurons in cold nociception.**
860 Blue arrows indicate strength of synaptic connectivity between the CIII md neurons and second
861 order neurons. In behavioral analysis column, the arrow direction indicates reduction or
862 enhancement of CT response and shading indicates magnitude of change from control. In neural
863 activity column: NC denotes no significant change in Ca^{2+} response, the arrow direction
864 indicates reduction or enhancement in evoked Ca^{2+} response and shading indicates magnitude of
865 change from control. Empty spaces indicate experimental analyses were not performed.
866

867 **Ascending interneurons are required for cold nociceptive responses**
868
869 Sensory, second order multisensory integration neurons (Basins) and a premotor neuron
870 (DnB) have further direct synaptic connectivity to a set of projection neurons including A09e,
871 A08n, and *R61A01*^{GAL4} labeled neurons (labels: A10j, A09o, TePn04, TePn05) that have
872 previously been implicated in anemotaxis, mechanosensory or chemosensory evoked behavioral
873 responses (Hu et al., 2017; Jovanic et al., 2019; Kaneko et al., 2017; Masson et al., 2020;
874 Vogelstein et al., 2014). Briefly, A09e receives synaptic inputs from CIII md, CIV md, A08n,
875 DnB, and TePn05 (**Figure 7A, Figure 7-figure supplement 1A**). A09e and CIII md neurons are
876 both required for *Drosophila* larval anemotaxis (Jovanic et al., 2019; Masson et al., 2020). A08n
877 primarily receives inputs from CIV md neurons and very few inputs from CIII md neurons
878 (**Figure 7A, Figure 7-figure supplement 1A**). However, *Drosophila* third instar larval synaptic
879 connectivity visualization using GFP reconstituted across synaptic partners (GRASP) revealed
880 that A08n are not synaptic partners of CIII md neurons (Kaneko et al., 2017). A08n neurons
881 function downstream of CIV md neurons for noxious chemical and mechanical nociception (Hu
882 et al., 2017; Kaneko et al., 2017) and neural activation of Ch and CIII md neurons does not lead
883 to activation of A08n neurons (Tenedini et al., 2019). *R61A01*^{GAL4} labeled neurons receive inputs
884 from Ch, CIII md, CIV md, Basins, DnB, and A09e (**Figure 7A, Figure 7-figure supplement**
885 **1A**). Neurons labeled by *R61A01*^{GAL4} have been implicated in mechanosensation (Masson et al.,
886 2020). We assessed whether the following projection neurons A09e, A08n, and neurons in the
887 expression pattern of the GAL4 line *R61A01* (A10j, A09o, TePn04, TePn05) are required for
888 cold evoked behaviors and function in conjunction with CIII md neurons for generating CT
889 behavioral response.
890 Neural silencing of projection neurons using cell specific expression of tetanus toxin led
891 to impairments in cold evoked behaviors. Neurotransmission inhibition in projection neurons
892 (A09e and *R61A01*) that receive strong connectivity from CIII md neurons led to significant
893 reductions in all the CT behavioral metrics that we analyzed (**Figure 7B-E**). As expected, A08n
894 neurons, which primarily receive inputs form CIV md neurons, are not required for cold-evoked
895 CT response (**Figure 7B-E**). Whereas neural silencing of A09e or *R61A01* neurons led to greater
896 than 50% reduction in cold evoked responses from controls (**Figure 7J**).
897 Next, we assessed whether these projection neurons were able to elicit a CT response
898 upon neural stimulation. Optogenetic stimulation of projection neurons alone did not lead to any
899 CT response (**Figure 2-figure supplement 2**). Simultaneous co-activation of CIII md and
900 *R61A01*^{GAL4} or A08n neurons led to mild but statistically insignificant increases in CT responses
901 (**Figure 7F-I, J**). Co-activation of A09e and CIII md neurons led to facilitation of CT behavior,
902 where compared to controls there were significant increases across all behavioral metrics that we
903 analyzed (**Figure 7F, G-I**). There were mild, statistically insignificant, reductions in larval
904 immobility when these projection neurons were co-activated with CIII md neurons, however,
905 they were significant for A08n (**Figure 7-figure supplement 1B-D**). A09e, which has receives

906 substantial inputs from CIII md neuron, was sufficient to facilitate CIII md neuron evoked
907 behavioral responses (**Figure 7J**).
908 Our neural silencing analyses suggest that A09e and *R61A01*^{GAL4} (A10j, A09o, TePn04,
909 TePn05) neurons are required for cold evoked responses. We hypothesized that these neurons are
910 cold sensitive and function downstream of CIII md neurons. We predicted that these neurons will
911 have increases in Ca^{2+} upon cold stimulation or optogenetic activation of CIII md neurons. A09e
912 neurons present indeed significant increases in Ca^{2+} levels upon cold stimulation, as measured by
913 cell type-specific expression of CaMPARI2 (**Figure 8A**). Optogenetic activation of CIII md
914 neurons led to significant increases in evoked Ca^{2+} levels of A09e neurons (**Figure 8B, C**).
915 Multiple stimulations of CIII md neurons did lead to slightly lower levels of evoked Ca^{2+} but
916 overall Ca^{2+} response was largely similar between stimulations (**Figure 8B, C**). For *R61A01*^{GAL4}
917 Ca^{2+} imaging experiments, we restricted our analyses to TePn04 and TePn05 neurons, which
918 were reliably identifiable in an intact *Drosophila* larval preparation. There were significant
919 increases in CaMPARI2 response of TePn04/05 neurons upon cold stimulation (**Figure 8E**).
920 Optogenetic stimulation of CIII md neurons led to strong increases in Ca^{2+} levels of TePn04/05
921 neurons, however, Ca^{2+} levels rapidly returned to baseline levels (**Figure 8F, G**). Repeated
922 stimulations of CIII md neurons led to a blunted Ca^{2+} response in TePn04/05 neurons following
923 the initial stimulation (**Figure 8F, G**). Combined, these data indicate A09e and *R61A01*^{GAL4}
924 neurons function downstream of CIII md neurons for cold nociception (**Figure 8-figure**
925 **supplement 1**), indicating that ascending neurons relay cold somatosensation to the brain.

926

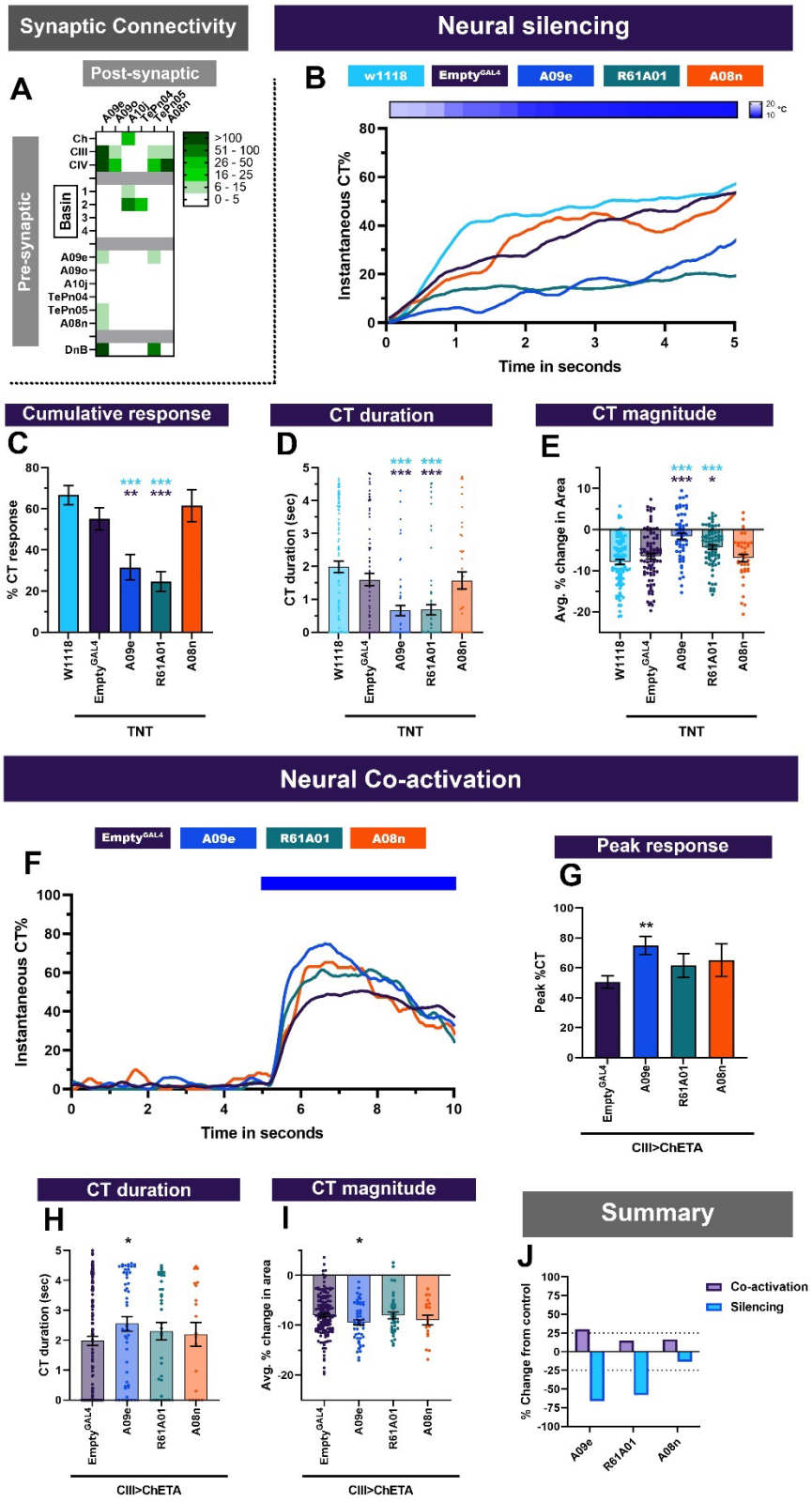
Synaptic Connectivity
Neural silencing
Post-synaptic
Pre-synaptic
A
B
w1118
Empty^GAL4
A09e
R61A01
A08n
Instantaneous CT%
Time in seconds
Cumulative response
CT duration
CT magnitude
C
D
E
% CT response
CT duration (sec)
Avg. % change in Area
TNT
Neural Co-activation
F
G
Peak response
Peak %CT
CIII>ChETA
H
I
Summary
J
Co-activation
Silencing
% Change from control

927 **Figure 7: Projection neurons downstream of CIII md neurons are required for cold-evoked**
928 **responses.**
929 (**A**) A09e, A09o, A10j, TePn04, TePn05 and A08n primarily receive inputs from CIII
930 md, CIV md, Basin-1, Basin-2 and DnB neurons. Heatmap plot of pre-synaptic connections to
931 projection neurons. Synaptic connectivity data was extracted from Neurophyla LMB Cambridge.
932 (https://neurophyla.mrc-lmb.cam.ac.uk/). (**B-E**) Cold evoked responses of third instar
933 *Drosophila*. Projection neurons were silenced by inhibiting neurotransmitter release via cell type
934 specific expression of tetanus toxin (TNT), where A09e ($SS00878^{splitGAL4}$), $R61A01^{GAL4}$ (labels
935 A09o, A10j, TePn04, and TePn05) and A08n ($R82E12^{GAL4}$). (**B**) Instantaneous %CT over time.
936 Heatmap on top represents change in temperature over time. (**C**) Cumulative %CT response for a
937 duration of 5 seconds. (**D**) CT duration in seconds. (**E**) CT magnitude as average percent change
938 in area for the duration of stimulus. Controls include *w1118* and $Empty^{GAL4}>TNT$. Average n=73.
939 Significant stars: turquoise stars represent comparison to *w1118* and purple stars represent
940 comparison to $Empty^{GAL4}>TNT$. (**F-I**) Neural co-activation of projection neurons and CIII md
941 neurons. Here each condition represents expression of ChETA in CIII md neurons plus
942 projection neurons. (**F**) Instantaneous %CT over time. Blue bar represents optogenetic neural
943 activation. (**G**) Peak %CT response during optogenetic stimulation. (**H**) CT duration in seconds
944 during optogenetic stimulation. (**I**) CT magnitude as average percent change in area for the
945 duration of stimulus. $Empty^{GAL4}$ n=143 and experimental condition average n =35. Significant
946 purple stars represent comparison to *CIII md* + $Empty^{GAL4}>ChETA$. (**J**) Overall percent change
947 from control for either neural silencing or neural co-activation. The metrics for neural silencing
948 include cumulative %CT, CT magnitude, and CT duration. The following metrics were used to
949 calculate percent for neural co-activation: cumulative %CT, peak %CT, CT duration and
950 magnitude. Significant differences indicated via asterisks, where *$p<0.05$, **$p<0.01$, and
951 ***$p<0.001$.
952

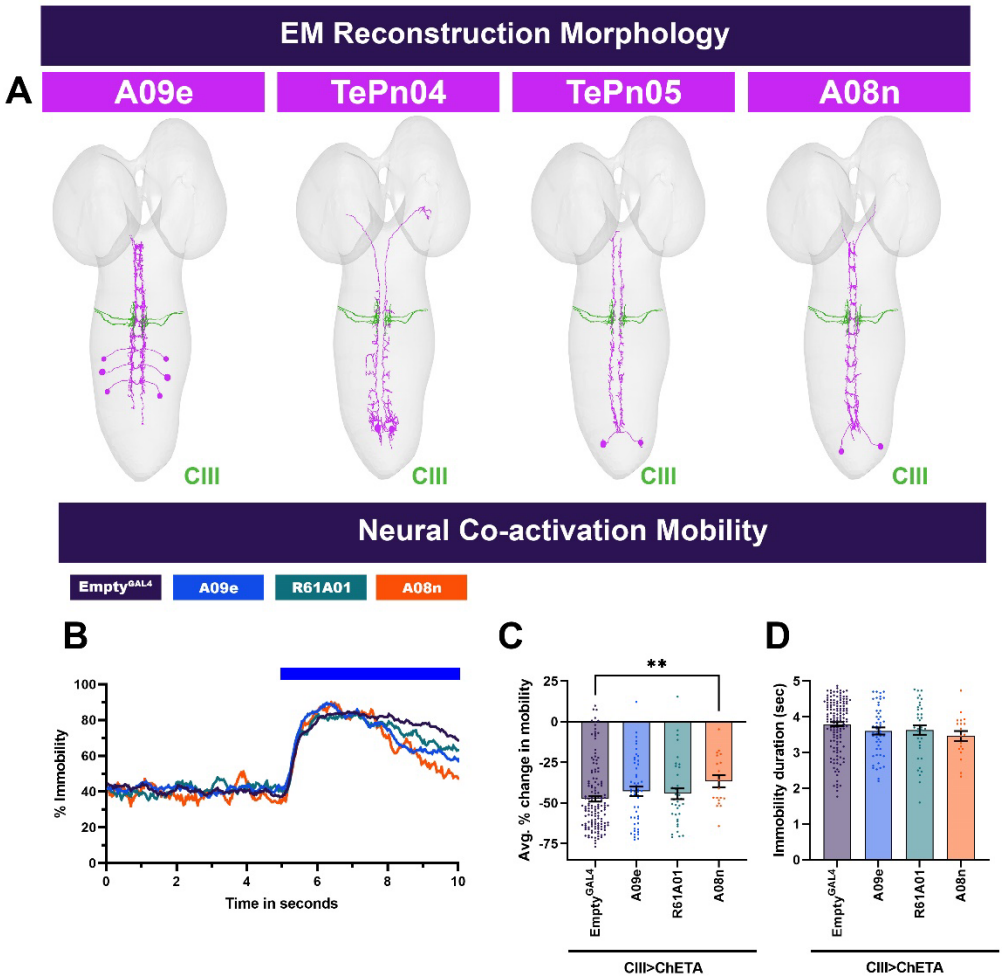

953 **Figure 7-figure supplement 1: Neural reconstructions and larval mobility for projection**
954 **neurons.**
955 (**A**) Individual projection neuron subtypes (magenta) and CIII md neuron axons (blue). Neural
956 reconstruction data was extracted from Neurophyla LMB Cambridge. (https://neurophyla.mrc-
957 lmb.cam.ac.uk/). (**B-D**) *Drosophila* larval mobility observed with projection neurons plus CIII
958 md neuron optogenetic coactivation. (**B**) Instantaneous percent immobility. Blue bar represents
959 optogenetic neural activation. (**C**) Average percent change in mobility for each genotype, where
960 greater percent immobility results in larger changes in average mobility. (**D**) Immobility duration
961 in seconds during stimulation. Significant stars represent $p<0.05$, where stars represent
962 comparison to *CIII md + Empty^{GAL4}>ChETA*. Empty^{GAL4} n=143 and experimental condition
963 average n =35. Significant differences indicated via asterisks, where **$p<0.01$.
964

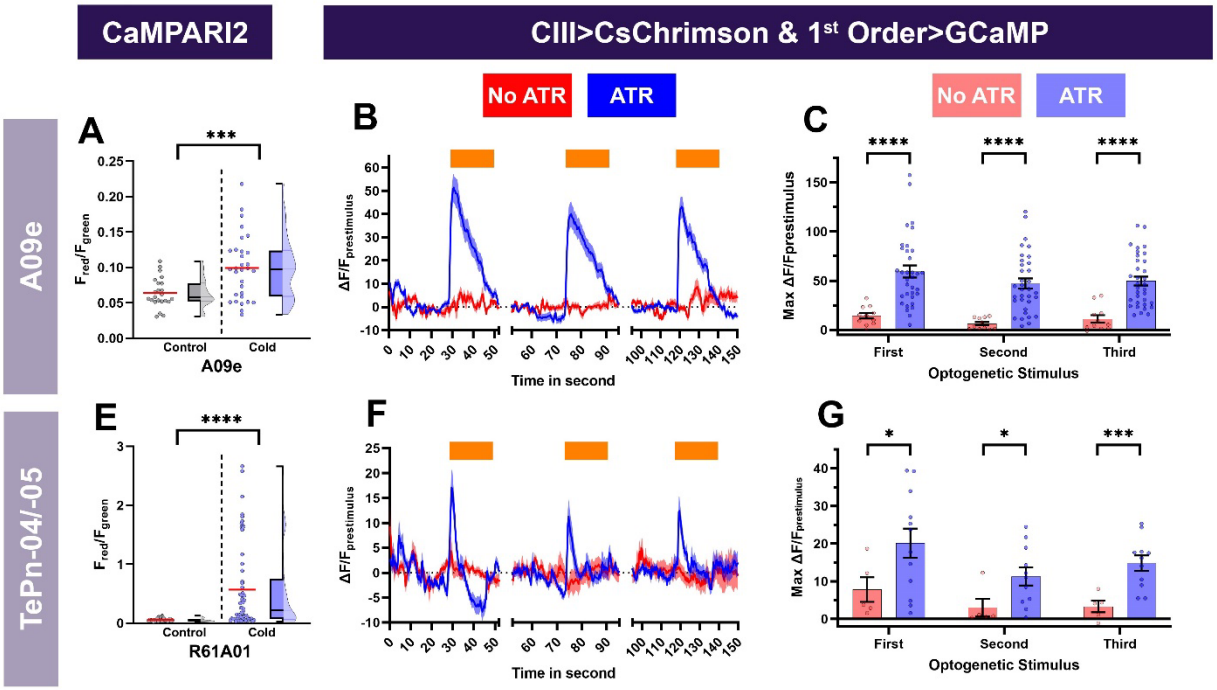

Figure 8: Cold- and CIII- evoked calcium responses of projection neurons. Neural responses of A09e (*SS00878*^{GAL4}) (**A-C**) and terminally located TePns (-04, -05) were analyzed using *R61A01*^{GAL4}(**E-G**). (**A,E**) Ca^{2+} responses of projection neurons upon cold exposure vs. controls (room temperature). Cold evoked neural responses (CaMPARI2) of projection neuron cell bodies were analyzed for (**A**) A09e (n=27) and (**E**) TePns04, & TePn05 (n=42). CaMPARI2 fluorescence ratio is reported as F_{red}/F_{green}. We report the data as individual datapoints, where the red line represents mean, and hybrid plots (boxplot & violin) for visualizing the distribution and quartiles of data. Significant stars represent $p<0.05$, where comparisons were made to their respective no stimulus controls. (**B-C, F-G**) To assess, if A09e or TePns functions downstream of CIII md neurons, we optogenetically activated CIII md neurons (*83B04*^{lexA}*>CsChrimson*) and visualized changes in evoked Ca^{2+} using projection neuron specific *GAL4>GCaMP6m*. Control: No ATR supplemented diet, which is required for optogenetic stimulation in *Drosophila*. Orange bars indicate optogenetic stimulation. (**B, F**) Changes in GCaMP reported as $\Delta F/F_{prestimulus}$, where prestimulus refers to 15 seconds prior to optogenetic stimulation. (**F**) Maximum neuronal responses ($\Delta F/F_{prestimulus}$) upon optogenetic stimulation. A09e average n=22. TePns average n=8. Significant differences indicated via asterisks, where *$p<0.05$, ***$p<0.001$, and ****$p<0.0001$.

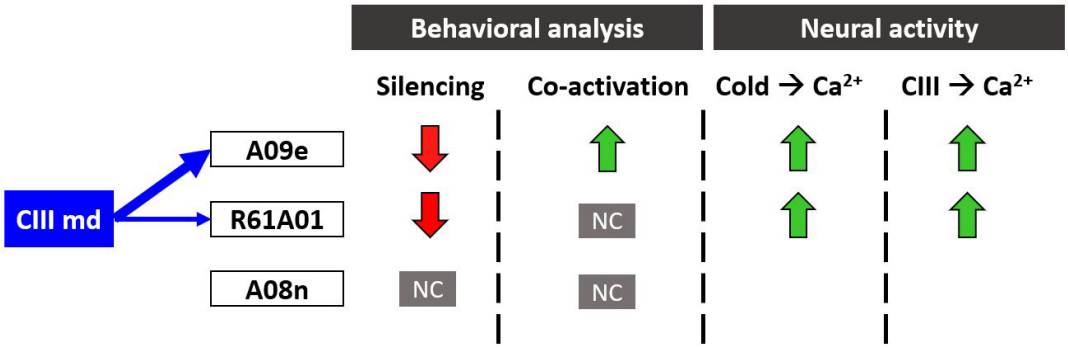

983 **Figure 8-figure supplement 1: Summary of behavioral and functional roles of projection**
984 **neurons in cold nociception.**
985 Blue arrows indicate strength of synaptic connectivity between the CIII md neurons and second
986 order neurons. In behavioral analysis column, the arrow direction indicates reduction or
987 enhancement of CT response and shading indicates magnitude of change from control. In neural
988 activity column: NC denotes no significant change in Ca^{2+} response, the arrow direction
989 indicates reduction or enhancement in evoked Ca^{2+} response and shading indicates magnitude of
990 change from control. Empty spaces indicate experimental analyses were not performed.
991
992 **Comparative analyses of cold sensitive neurons**
993
994 Thus far, data were presented in logical groups based on their previously known cell-
995 types and functions, however, these neurons function in an interconnected network and
996 behavioral and functional imaging data must be assessed collectively to study circuit function.
997 As discussed in previous sections, of all the cell types we tested only optogenetic activation of
998 CIII md neurons alone is sufficient to elicit CT responses (**Figure 2-figure supplement 2**).
999 Neural co-activation of CIII md neurons plus additional cell types resulted in marked increases in
1000 CT responses compared to only CIII md neuron activation (**Figure 9A**). Neural silencing of cell
1001 types downstream of CIII md neurons led to significant reductions in cold-evoked CT (**Figure**
1002 **9B**). To understand how these behavioral phenotypes are interrelated, we performed t-distributed
1003 stochastic neighbor embedding (t-SNE) analysis on both neural silencing and co-activation
1004 behavioral datasets. We identified five different clusters that exhibit varying impacts on
1005 behavioral phenotypes upon either neural co-activation or silencing (**Figure 9C, D**). The first
1006 group clusters together with the control genotype and includes CIV, A05q, Goro, and A08n
1007 neurons. This group on average had less than 25% change in behavioral phenotypes in either
1008 neural co-activation or silencing experiments (**Figure 9C, D**). Basin-1 and DnB neurons
1009 clustered together, where on average they had 49% enhancement of CT response upon neural co-
1010 activation and 45% reduction in cold evoked CT response upon neural silencing (**Figure 9C, D**).
1011 *R61A01* and CIII md neurons formed a cluster, where neural silencing resulted in nearly 60%
1012 reduction cold evoked behavior and 20% enhancement of CIII evoked behaviors upon neural co-
1013 activation (**Figure 9C, D**). A group of neurons including Chair-1, Basin-4 and Ch were required

1014 for cold evoked behavioral responses, however, these neurons did not facilitate CIII evoked CT
1015 responses (**Figure 9C, D**). In the last group, neural silencing of all Basins, Basin-2, mCSI, A00c
1016 or A09e led to an overall 69% reduction in cold evoked behaviors and 34% enhancement in CIII
1017 evoked CT response (**Figure 9C, D**).
1018 Analyses of *Drosophila* larval behavioral phenotypes revealed distinct roles for
1019 downstream neurons in cold nociceptive circuitry. Mapping synaptic connectivity of a particular
1020 circuit is only the first step in understanding how individual behaviors arise. Here, we draw
1021 attention to select CIII md neuron first-order neurons (Basins (-2 & -4), DnB, TePns and A09e)
1022 that showed robust requirements for cold nociceptive behaviors and had functional connectivity
1023 to CIII md neurons (**Figure 9E**). TePns synapse onto Basin-4 and form reciprocal connections to
1024 Basin-2, DnB, and A09e (**Figure 9E)**. DnB further synapses onto Basin-4 and A09e. Within this
1025 circuit motif one might predict that A09e neurons function as the master integrators, where they
1026 might be computing synaptic information from various sources (**Figure 9E)**. Consistent with EM
1027 connectivity, A09e neurons have the highest CIII md neuron evoked Ca^{2+} responses of the tested
1028 cell types (**Figure 9F, G)**. Compared to Basin-4 neurons, Basin-2 neurons receive greater
1029 synaptic input from CIII md neurons (**Figure 9E**). However, CIII md neuron activation leads to
1030 nearly twice as much Ca^{2+} response in Basin-4 neurons than Basin-2 (**Figure 9F, G)**. DnB
1031 neurons receive the second highest synaptic input from CIII md neuron and have the second
1032 highest CIII md neuron evoked Ca^{2+} response (**Figure 9F, G)**. TePns receive significantly lower
1033 synaptic input compared to Basin-2 neurons, however, they both exhibit similar levels of CIII
1034 evoked Ca^{2+} response (**Figure 9F, G)**. Comparative analyses reveal that synaptic connectivity is
1035 informative about functional neural activity, however, additional molecular and functional
1036 studies are required to fully understand roles of these neurons in cold nociception. Collectively,
1037 our findings on neural substrates of cold nociception indicate that second order multisensory
1038 integration by Basin neurons, select pre-motor neurons and projection neurons are preferentially
1039 activated in a stimulus specific manner to elicit appropriate behavioral responses.
1040
1041
1042
1043
1044

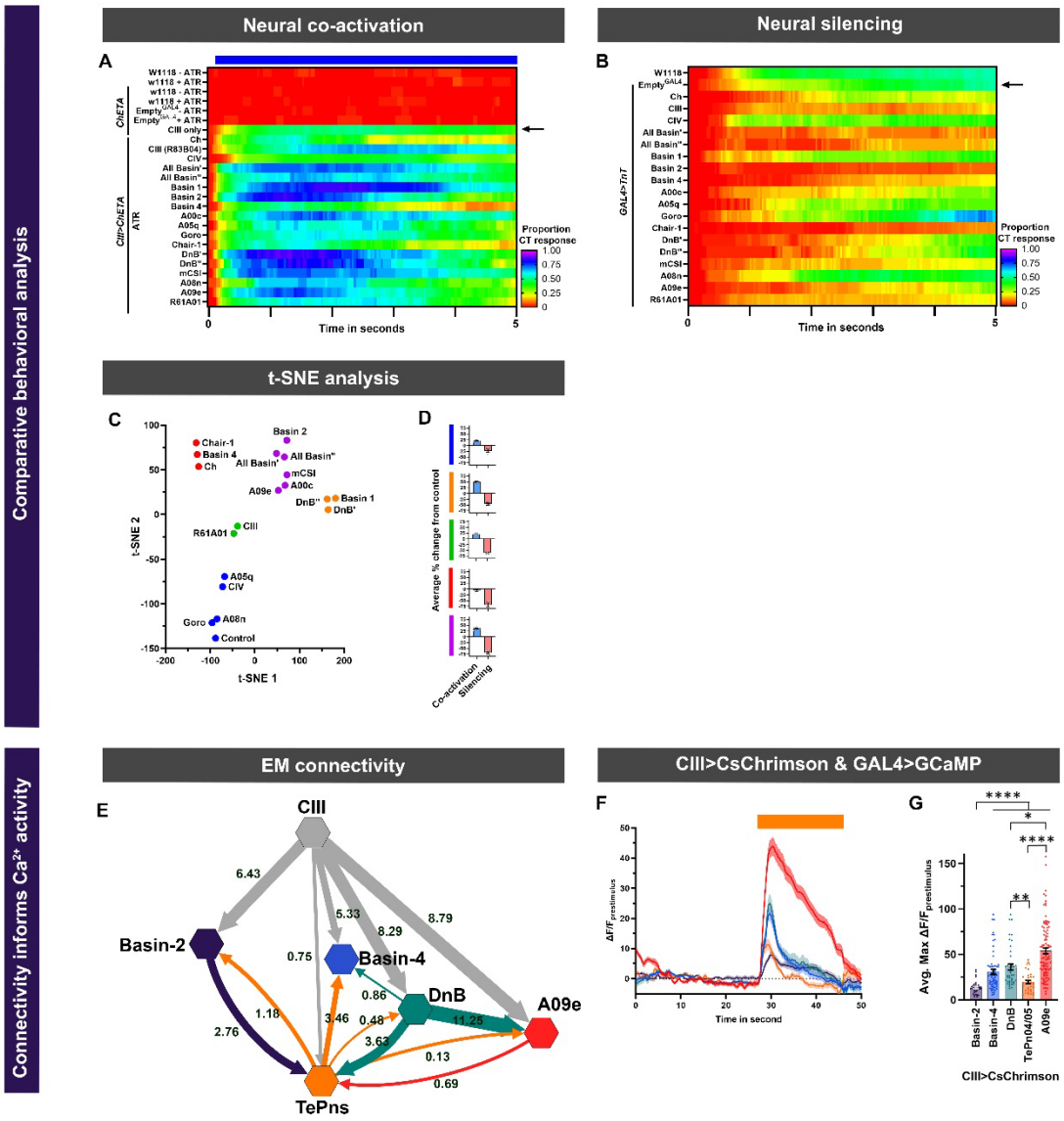

1045 **Figure 9: Dimensional reduction analysis of *Drosophila* larval behavioral responses and**
1046 **synaptic connectivity informs functional connectivity assessed via Ca^{2+} imaging**
1047 (**A-B**) Instantaneous CT proportions for all genotypes in this study. (**A**) Neural co-activation
1048 experiments, where CIII plus additional neuronal types were simultaneously optogenetically
1049 activated. Controls for optogenetic experiments were tested with or without ATR supplement
1050 and include the following conditions: background strain (*w1118*), background strain crossed to
1051 *UAS-ChETA*, and *Empty*^{GAL4} crossed to *UAS-ChETA*. Blue bar represents optogenetic

1052 stimulation. (**B**) Neurotransmitter release inhibition of individual neuronal types using cell-type
1053 specific expression of TnT. (**C-D**) t-distributed stochastic neighbor embedding (t-SNE) analysis
1054 of all neuronal subtypes role in both cold nociception (neural silencing data) and CIII md neuron
1055 evoked CT facilitation (co-activation data). (**C**) 2D plot of t-SNE analysis, where post-hoc
1056 clustering analysis based on "Euclidian complete" method revealed 5 unique groups. The
1057 following percent change from control (*Empty*^{GAL4}) data were included in the analysis: For neural
1058 co-activation (peak % CT response, cumulative % CT response, average % change in area, and
1059 CT duration) and for neural silencing (cumulative % CT response, average % change in area, and
1060 CT duration). (**D**) Average percent change from control for each cluster in '**C**' across all neural
1061 co-activation or neural silencing metrics. (**E-G**) Analyses of connectivity upon select circuit
1062 components and comparative CIII md neuron evoked calcium responses in post-synaptic
1063 neurons. (**E**) Proportion of synaptic inputs amongst neurons are plotted. A09e neurons integrate
1064 responses from multiple pathways originating from CIII md neurons. Network map created using
1065 Cytoscape (Shannon et al., 2003) (**F-G**) CIII md neuron evoked calcium responses in post-
1066 synaptic neurons. (**F**) $\Delta F/F_{baseline}$ over time. (**G**) Average max $\Delta F/F_{baseline}$. Averages ± SEM of all
1067 trial are plotted. Significant differences indicated via asterisks, where *$p<0.05$, **$p<0.001$, and
1068 ****$p<0.0001$.
1069
1070 **Discussion**
1071
1072 Environmental stimuli are detected by peripheral sensory neurons, which transduce
1073 relevant cues to downstream central circuitry responsible for processing multisensory input and
1074 generating stimulus-relevant behavioral responses. The study of the diverse molecular and
1075 cellular mechanisms involved in sensory discrimination have yielded key insights into how
1076 animals interact with their environment (Arnadóttir et al., 2011; Bandell & Patapoutian, 2009;
1077 Cho & Oh, 2013; Corfas & Vosshall, 2015; Coste et al., 2010; Derby et al., 2016; Dietrich et al.,
1078 2022; Fowler & Montell, 2013; Freeman & Dahanukar, 2015; Himmel et al., 2017; Leung &
1079 Montell, 2017; Montell, 2021; Wu et al., 2018; Xiao & Xu, 2021). However, how animals
1080 distinguish between innocuous and noxious stimuli at molecular, cellular and circuit level
1081 remains an important question in modern neuroscience (Bushnell et al., 1985; Dannhauser et al.,
1082 2020; Himmel et al., 2023; Imambocus et al., 2022; Moehring et al., 2018; Patel et al., 2022;
1083 Turner et al., 2016; Ward et al., 1996).
1084 Here, we assessed the downstream circuitry of a multimodal sensory (CIII md) neuron
1085 that detects both innocuous mechanical and noxious cold temperatures. In CIII md neurons,
1086 detection of innocuous cues occurs via low threshold activation and noxious cues are detected
1087 via high threshold activation leading to stimulus-relevant behaviors (Turner et al., 2016).
1088 Transduction of nociceptive cold stimulus is predominantly mediated by multimodal (innocuous
1089 and noxious) sensitive Ch and CIII md neurons. However, nociceptive peripheral sensory
1090 neurons, CIII md and CIV md neurons, function through shared downstream neural circuitry. We
1091 describe the behavioral and functional requirements of multisensory integration (Basins)

1092 neurons, premotor (DnB and mCSI) neurons and projection (A09e and TePns) neurons in
1093 noxious cold evoked behavioral responses. We identified circuit components that play a role in
1094 amplifying noxious cues and differentiating between opposing noxious (heat versus cold)
1095 stimuli-evoked behaviors at various levels of sensory processing. Our findings provide key
1096 insights into how environmental cues are processed by multiplexed networks for multisensory
1097 integration and decision making.
1098
1099 **Basin-1 neurons function across sensory modalities as gain modulators for noxious stimuli-**
1100 **evoked escape responses.**
1101
1102 Accurately responding to potentially harmful stimuli by appropriately executing
1103 energetically expensive escape behaviors is critical for animal survival. Incorrectly performing
1104 escape responses in absence of dangerous stimuli can have long-term detrimental consequences.
1105 Therefore the need for neural mechanisms responsible for integrating various noxious and
1106 innocuous sensory stimuli for accurately executing stimulus-appropriate escape responses. Here,
1107 we focus on the role of Basin neurons, known to mediate various escape responses (Jovanic et
1108 al., 2016; Masson et al., 2020; Ohyama et al., 2015).
1109 EM connectome analyses revealed that somatosensory (Ch, CIII md and CIV md)
1110 neurons all synapse onto multisensory integrating Basin neurons, and that amongst the Basins
1111 subtypes, Basin-1 neurons are presynaptic to Basin-2,-3 and -4 neurons (Masson et al., 2020;
1112 Ohyama et al., 2015). On the basis of the known connectome, we analyzed the function of Basin
1113 neurons in cold-evoked escape behaviors. Our findings indicate that optogenetic activation of
1114 Basin-1 is not sufficient to evoke noxious cold evoked behavioral response (**Figure 2 –**
1115 **Supplement 2**) and it was known that thermogenetic activation of Basin-1 is also not sufficient
1116 for evoked rolling escape (Ohyama et al., 2015). Therefore, Basin-1 neuron activity alone is not
1117 sufficient to elicit a noxious stimuli-evoked behavioral response. However, due to intricate
1118 connectivity amongst the Basins, the total integrated output of multiple Basin neurons may lead
1119 to threshold activation of noxious stimulus evoked escape responses. And indeed, thermogenetic
1120 co-activation assays found that Basin-1 neural activity could facilitate a Basin-4 -mediated
1121 rolling response (Ohyama et al., 2015), and also the activation of Basin-1 neurons leads to the
1122 activation of Basin-2 neurons through lateral disinhibition (Jovanic et al., 2016).. Here, we found
1123 that co-activation of Basin-1 plus CIII md neurons led to strong evoked CT responses (**Figure 2**).
1124 Taken together, these studies concluded that Basin-1 facilitates the activation of other Basin
1125 neurons, and our results also provide additional support for the role of Basin-1 neurons in fine-
1126 tuning behavioral outcomes and enhancing cumulative output of multisensory integration Basin
1127 neurons leading stimulus specific escape responses.
1128
1129 **Multisensory integration neurons drive behavioral selection downstream of sensory**
1130 **neurons.**
1131

1132 In order to evaluate the functional and behavioral roles of neurons within a circuit, a
1133 comprehensive analysis of both upstream and downstream synaptic connectivity is necessary.
1134 Basin-2 and -4 neurons integrate different amounts of synaptic input from somatosensory
1135 neurons, other Basin neurons, feedforward inhibitory local neurons, and projection neurons.
1136 Basin-4 neurons receive greater excitatory synaptic input compared to Basin-2 neurons, which
1137 have greater connectivity with local inhibitory neurons (Jovanic et al., 2016; Masson et al., 2020;
1138 Ohyama et al., 2015). Larger inhibitory connectivity of Basin-2 neurons likely arises from much
1139 broader downstream connectivity including several projection neurons, premotor neurons and
1140 feedback inhibitory local neurons, whereas Basin-4 downstream connectivity is restricted to
1141 limited set of neurons. These synaptic level differences in multisensory integration neurons
1142 underlie noxious stimuli-specific evoked responses, and suggest that CIII md neuron mediated
1143 responses primarily function through Basin-2 neurons and CIV md neuron mediated
1144 environmental cues are processed via Basin-4 neurons.
1145
1146 Chemical nociception in *Drosophila* larvae primarily functions via CIV md. Among the
1147 md neurons, CIII md neurons are the least sensitive to noxious chemical stimulus (Lopez-Bellido
1148 et al., 2019). Analyses of Basin neuron requirement in chemical nociception revealed that all
1149 Basins are necessary for chemical-evoked rolling, where comparative analyses of Basin subtypes
1150 revealed that chemical nociception is primarily mediated through Basin-4 with weaker
1151 behavioral phenotypes of Basin-1 or -2 (Lopez-Bellido et al., 2019). Our work shows that
1152 inhibition of neurotransmission in Basin-2 or Basin-4 neurons leads to significant reductions in
1153 cold nociceptive responses, where across the analyzed behavioral metrics Basin-2 had stronger
1154 deficits in cold evoked responses (**Figure 2**). Furthermore, neural co-activation analyses revealed
1155 that Basin-2 plus CIII md led to enhanced CT response, whereas Basin-4 plus CIII md co-
1156 activation did not facilitate but rather suppressed the CT response (**Figure 2**). Basin-2 neural
1157 activity likely has cascading effects on functions of downstream neurons, which we also found to
1158 be required for cold nociception. Behavioral assessment of multisensory integration neurons
1159 supports the notion that CIII md neuron sensory input is processed primarily by Basin-2 and CIV
1160 md neuron sensory cues are processed via Basin-4 neurons.
1161
1162 Despite the accumulating evidence that cold-evoked responses are primarily mediated by
1163 Basin-2, our Ca^{2+} analyses revealed that compared to Basin-2, Basin-4 neurons have much
1164 greater cold- or CIII md neuron- evoked Ca^{2+} responses. There are a few possible explanations
1165 for greater Basin-4 activity levels. Firstly, greater Basin-4 Ca^{+2} activity could be due to greater
1166 synaptic input from projection neurons (TePn04/05) and premotor neurons (DnB), which are
1167 both required for cold nociception and exhibit cold- or CIII md neuron- evoked Ca^{2+} responses
1168 (**Figure 7, Figure 8 – Supplement 1**) (Masson et al., 2020). Secondly, reduced Basin-2 Ca^{2+}
1169 responses could be due to greater connectivity with feedback/feedforward inhibitory local
1170 neurons (Jovanic et al., 2016; Masson et al., 2020), therefore suggesting that Basin-2 could be
1171 mediating an onset response rather than a sustained response. Additional comparative Ca^{2+}

imaging or electrophysiological analyses are required to further determine how Basin-2 and -4 neurons integrate sensory information across somatosensory modalities leading to distinct behavioral responses. However, to date, synaptic connectivity and behavioral analyses collectively indicate an initial sensory discrimination node amongst the Basin neurons, where downstream processing of CIII mediated sensory input is conveyed through Basin-2 and its downstream connectivity, meanwhile CIV somatosensory information is transduced through Basin-4 neuronal pathway.

Differential roles of pre-motor neurons lead to behavioral selection.

Animal locomotive behavioral responses are implemented through neurosecretory systems and muscle contractions evoked by motor neuron activity. Motor neurons integrate a conglomerate of neural impulses from premotor neurons, leading to appropriate muscle activation patterns to implement specific behavioral responses (Bellardita & Kiehn, 2015; Berkowitz et al., 2010; Carreira-Rosario et al., 2018; Green & Soffe, 1996; Huang & Zarin, 2022; Liao & Fetcho, 2008; Talpalar et al., 2013; Zarin et al., 2019). Recent work in premotor and motor neuron connectomics has provided evidence for both labeled line and combinatorial connectivity between promotor and motor neurons that give rise to co-active motor neurons states leading to selective muscle group activation (Huang & Zarin, 2022; Zarin et al., 2019). Various *Drosophila* larval premotor neuron subtypes and/or motor pools have been implicated in locomotion, nociception, and innocuous mechanosensation (Burgos et al., 2018; Huang & Zarin, 2022; Jovanic et al., 2019; Kohsaka et al., 2017; Kohsaka et al., 2014; Kohsaka et al., 2019; Yoshino et al., 2017; Zarin et al., 2019). Neural reconstruction efforts in *Drosophila* larvae have revealed that somatosensory (CIII md and CIV md) neurons are not directly connected to motor neurons, but rather feed into polysynaptic pathways leading to motor neurons via premotor neurons (such as the DnB, mCSI, & Chair-1 neurons studied here) (Jovanic et al., 2019; Ohyama et al., 2015; Winding et al., 2022). Premotor neurons (DnB, mCSI, and Chair-1) that receive synaptic input from CIII md neurons are required for cold-evoked responses. However, only premotor neurons previously implicated in nociceptive escape responses, DnB and mCSI, can facilitate CIII evoked CT responses (Burgos et al., 2018; Lopez-Bellido et al., 2019; Yoshino et al., 2017). Meanwhile, Chair-1 neurons, which are required for innocuous mechanosensation, do not facilitate CIII md neuron mediated CT responses (Jovanic et al., 2019). We showed, with Ca^{2+} imaging, that Chair-1 neurons are not activated upon cold exposure. It remains unclear whether Chair-1 neuronal function is sufficient to drive specific sensory evoked behaviors or requires a combinatorial pre-motor neuronal activity for generating evoked behavioral responses. Given the data, we speculate that Chair-1 neurons likely gate innocuous-to-noxious stimulus evoked behaviors; however, additional functional studies are required to tease out how Chair-1 neurons function in behavioral selection.

1212 **Heterogeneity in thermosensory processing reflects variety of thermal stimuli.**
1213
1214 Animals detect changes in temperature through a variety of sensors that occupy and
1215 function in different spatiotemporal timescales. Thermosensory systems function to detect
1216 changes at the epidermal, brain and visceral levels, and these broad thermosensory inputs must
1217 be integrated to generate appropriate behavioral responses (Nakamura, 2018). The underlying
1218 neural circuitry for thermosensation differs based on body plan and type of thermosensation. In
1219 mice, cool and warm sensory signals, which are detected by TRP channels, are transmitted to the
1220 spinal dorsal horn, where distinct cool/warm pathways relay epidermal changes in temperature to
1221 thalamocortical regions for perception and discrimination (Nakamura, 2018). In *Drosophila*
1222 larvae and adults, thermotaxis occurs through temperature detection via dorsal organ ganglion
1223 (DOG) and antennal thermoreceptors, respectively (Frank et al., 2015; Gallio et al., 2011; Klein
1224 et al., 2015; Liu et al., 2003). Investigations of circuit bases of thermotaxis have revealed
1225 different strategies for larval and adult systems. Adult antennal thermoreceptors have distinct hot
1226 or cold sensors, which project to the proximal antennal lobe (PAL), where hot and cold
1227 information is segregated into discrete regions (Gallio et al., 2011; Macpherson et al., 2015).
1228 Thermal coding properties of thermosensory projections neurons (tPNs), whose dendrites are
1229 located in PAL, include both slow/fast adapting tPNs and broadly/narrowly tuned tPNs (Frank et
1230 al., 2017). *Drosophila* larval thermosensory DOG contains both warm- and cool- sensing cells
1231 that are connected to individual cool or warm projection neurons (Hernandez-Nunez et al.,
1232 2021). DOG thermosensory information is further integrated by integration projection neurons
1233 (iPNs), which receive inputs from both warm and cool projection neurons (Hernandez-Nunez et
1234 al., 2021). The *Drosophila* larval noxious thermosensory system has distinct hot (CIV md) or
1235 cold (CIII md) sensing neurons (Babcock et al., 2009; Tracey et al., 2003; Turner et al., 2016).
1236 Larval somatosensory thermal inputs mediated by CIII md neurons are heavily integrated by
1237 second order neurons (Basins, DnB, A09e, etc.), where population coding leads to cold-evoked
1238 behavioral response. Noxious cold stimulus is encoded downstream of CIII md neurons by
1239 ascending neurons (A09e and TePns) that allow for systems-level integration of multiple thermal
1240 inputs including those from cool/warm sensitive larval DOG neural circuits and cold/heat
1241 information from CIII/CIV md neurons, respectively. Thermal information from the larval DOG
1242 and somatosensory neurons converges onto the mushroom body, where cool or warm projection
1243 neurons downstream of DOG and feed-forward projection neurons downstream of ascending
1244 neurons (A09e) synapse onto the same mushroom body output neuron (Eichler et al., 2017;
1245 Hernandez-Nunez et al., 2021; Winding et al., 2023). Thus far, ascending pathways into the brain
1246 have been characterized for larval cold nociception, however, descending output neurons
1247 responsible for cold-evoked behaviors remains unidentified. Diversity in processing
1248 thermosensory stimuli reflects heterogeneity at molecular, cellular, and circuit levels that
1249 collectively function to maintain proper thermal homeostasis and ultimately behavioral action
1250 selection. The *Drosophila* larval thermosensory system is well-suited to dissect mechanisms
1251 underlying central nervous system integration of varying spatial and functional thermosensory

information by utilizing various molecules, sensory systems, and interconnected circuits for appropriate behavioral responses.

Methods

Fly Strains

All *Drosophila melanogaster* strains used in this study are listed in (**Table 1**). All *Drosophila* reagents were maintained on standard cornmeal-molasses-agar diet in 12:12 hour light-dark cycle at ~22°C. All experimental crosses were raised in 12:12 hour light-dark cycle at 29°C, unless otherwise stated. The following strains were a gift from Marta Zlatic: Basin-2 ($SS00739^{splitGAL4}$), Basin-4 ($SS00740^{splitGAL4}$), A09e ($SS00878^{splitGAL4}$), and Chair-1 ($SS00911^{splitGAL4}$). We used two separate CIII md neuron driver lines in this study:$19\text{-}12^{GAL4}$ and $R83B04^{lexA}$.

Molecular cloning and transgenic generation of $CIII^{lexA}$

$GMR83B04^{GAL4}$ was characterized as CIII md neuron driver using both optogenetics and visualization using membrane markers (Himmel et al., 2023; Patel et al., 2022). The R83B04 enhancer containing entry vector was a gift from FlyLight team at Janelia Research Campus, Ashburn, VA. We performed Gateway cloning to insert R83B04 enhancer upstream of lexA. LR reaction was performed using R83B04 containing entry vector and lexA containing (pBPLexA::p65Uw) destination vector (Addgene: 26231). Transgenic fly generation was conducted by GenetiVision. $R83B04^{lexA}$ was inserted in VK20 docking site using PhiC31 integrase mediated transformation.

EM connectomics

All data for synaptic connectivity, circuit diagrams and wire frame projections of neural cell types were extracted from Neurophyla LMB Cambridge (https://neurophyla.mrc-lmb.cam.ac.uk/). Relevant primary literature sources are cited within the main text. Sensory neurons from abdominal segments 1-4 were analyzed and for the remaining cell types, all reconstructed neurons were included (date accessed: March 04, 2022).

Cold Plate Assay

We assessed requirements of neurons downstream from peripheral sensory neurons in cold evoked responses using the cold plate assay (Patel & Cox, 2017; Patel et al., 2022; Turner et al., 2016). *GAL4* drivers for select neuronal subtypes were used to express the light chain of tetanus toxin (*UAS-TNT*). We used two sets of controls: *w1118*, genetic background control, and $Empty^{GAL4}$, which contains a GAL4 construct but no regulatory promoter (*GAL4* only control). Genetic crosses were raised on standard cornmeal-molasses-agar diet and at 29°C. To assess cold evoked behavioral responses of age matched *Drosophila* third instar larvae, we exposed the ventral surface to noxious cold (10°C) temperatures. Briefly, using a brush we remove third

1292 instar larvae from food and place them on wet Kimwipe. Food debris is removed passively by
1293 allowing the larvae to freely locomote on wet Kimwipe. We place 6-8 larvae on a thin black
1294 metal plate that is subsequently placed on a pre-chilled (10°C) Peltier plate TE technologies
1295 Peltier plate (CP-031, TC-48-20, RS-100-12). Larval responses are recorded from above using
1296 Nikon DSLR (D5300). Changes in larval surface area were extracted using FIJI and Noldus
1297 Ethovision XT (https://github.com/CoxLabGSU/CaMPARI-intensity-and-cold-plate-assay-
1298 analysis/branches) (Patel et al., 2022). Next, we isolated individual larva from each video,
1299 removed background and used Ethovision to measure larval surface area. Using custom built r
1300 scripts, we compiled data from each larva and each genotype. Utilizing r, we calculated percent
1301 change in larval surface area (Area change= ($Area_N$ – $Average_Area_{baseline}$)/
1302 $Average_Area_{baseline}$*100). From the percent change in area dataset, we report three behavioral
1303 metrics: Average change in area, which is average percent change in area for the stimulus
1304 duration. We defined cold evoked CT response as change in area of -10% or less for at least 0.5
1305 consecutive seconds. CT duration, time spent at or below -10% change in area. Lastly, percent
1306 CT response, which is cumulative percent of animals that CT for at least 0.5 consecutive
1307 seconds.
1308 Statistical analysis: We preformed following statistical tests for all cold plate assay data
1309 analysis. %CT response: Fisher's exact with Benjamini-Hochberg for multiple comparison. We
1310 used r for performing comparisons of percent behavior response between genotypes, we used
1311 Benjamini-Hochberg multiple comparison correction. CT duration: Kruskal-Wallis with
1312 Benjamini, Krieger and Yekutieli for multiple comparisons. CT duration data are not normal. CT
1313 magnitude: One-way ANOVA with Holm-Šídák's for multiple comparisons.
1314
1315 **Neural activation via optogenetics**
1316 We performed two types of neural activations to assess sufficiency for CT response:
1317 single downstream neural activation and co-activation, where we simultaneously activated CIII
1318 md neurons and individual downstream neurons. For optogenetic experiments in *Drosophila*, a
1319 light sensitive co-factor all *trans*-retinal (ATR) is required. For all conditions, all adult animals in
1320 the genetic cross were placed in ATR (1500µM) supplemented food and subsequently F1
1321 progeny were also raised in food containing ATR and raised in dark. For control condition, we
1322 used an $Empty^{GAL4}$ containing GAL4 construct but no regulatory promoter. Optogenetic
1323 experiments were conducted using a similar setup as previously described (Patel et al., 2022).
1324 Briefly, we used principles of dark field microscopy to enhance signal to noise ratio and capture
1325 high resolution larval videos. We created a custom dark field stage, where a Canon DSLR T3i
1326 camera captures video from above. Neural activation is performed by two blue led lights that are
1327 controlled remotely using the Noldus control box (Thorlabs: DC4100, DC4100-hub, and two
1328 M470L3-C4 led light. Noldus: mini-IO box). Larval behaviors are directly captured using
1329 Noldus Ethovision XT software, which also controls blue led activation. All optogenetic
1330 experiments were conducted in a dimly lit room. Third instar *Drosophila* larva were removed
1331 from food plug and placed onto wet Kimwipe, where larval locomotion allowed for passive

removal of food debris. We lightly sprayed water onto a thin glass plate, then placed a single larva for optogenetic stimulation. The glass plate was manually moved on XY-axis to keep larva in the field of view. The following stimulus paradigm was used: 5 seconds of baseline (light off) and 5 seconds of neural activation (blue led lights on).

We performed video processing and behavioral analysis using FIJI and data compilation and analysis using r (https://github.com/CoxLabGSU/Drosophila_larval_optogenetic_analysis-area_and_mobility). In order to analyze *Drosophila* larval behavioral responses, we first automatically stabilized (XY axis) and then measured changes in larval surface area and mobility (described below).

Raw videos from Noldus Ethovision XT were uncompressed using video-to-video convertor (https://www.videotovideo.org/). The following steps were scripted in FIJI macro language for automatic video processing and data acquisition. For increasing processing speed, the uncompressed videos were automatically cropped to dimensions to contain all of the larva's movement. Next, using a pre-determined threshold, we created a mask followed by background removal using erode, remove outlier and dilate functions. We then used the 'Analyze Particles' function to obtain XY coordinates of the larva in each frame. Larval movements were stabilized using XY coordinates and the 'Translate' function was used to create a highly stabilized video. Next, we measured larval surface area using automatic thresholding 'Huang method' and 'Analyze Particles' to obtain area. We define *Drosophila* larval mobility as changes in occupied pixels between two frames. We used our stabilized larval video to measure larval mobility, where larval peristaltic movements (XY displacement) are not captured. However, changes in occupied pixels resulting from turning and head sweeps are captured. Specifically, larval mobility was measured by subtracting thresholded larva in each frame from the previous frame (Raw mobility = Thresholded $larva_{Frame\ N}$ - Thresholded $larva_{Frame\ N-1}$).

Data compilation and analysis was performed in r using custom scripts. Optogenetically evoked changes in behavior were analyzed independently for mobility and changes in area. For each larva, we calculated percent change in area (Area change= ($Area_N$ – $Average_Area_{baseline}$)/ $Average_Area_{baseline}$*100). We measured CT duration as the amount of time the larva has -10% or lower change in area. We also measure CT magnitude by analyzing average change area for stimulus duration. We report percent instantaneous CT over time as percent of animals that are at or below -10% change in area. Additionally, we report peak %CT from percent instantaneous CT dataset for each genotype. For analysis of mobility, we calculated percent change in mobility (Mobility change= ($Mobility_N$ – $Average_ Mobility_{baseline}$)/ $Average_ Mobility_{baseline}$*100). We report average percent change in mobility during stimulus for each genotype. We also plot percent immobility, which is calculated by the percent of animals with -25% or more reduction in mobility. Immobility duration is calculated based on amount of time individual animals spend at or below -25% mobility.

Statistical analysis: We preformed following statistical tests for all behavioral optogenetic data analysis. %CT peak response: Fisher's exact with Benjamini-Hochberg for multiple comparison. We used r for performing comparisons of percent behavior response between

genotypes, we used Benjamini-Hochberg multiple comparison correction. CT/immobility duration: Kruskal-Wallis with Benjamini, Krieger and Yekutieli for multiple comparisons. CT duration data are not normal. CT/immobility magnitude: One-way ANOVA with Holm-Šídák's for multiple comparisons.

CaMPARI Imaging

Post-synaptic neuron CaMPARI2 imaging: For assessing cold-evoked Ca^{2+} responses of sensory neurons and CIII md neuron downstream neurons, we utilized CaMPARI2, which upon photoconverting light and high intracellular Ca^{2+} stably photoconverts fluorescence from green to red. We performed the cold plate assay as described above. For stimulus condition, the Peltier plate was set to noxious cold (6°C) temperature and for control condition, the Peltier plate was turned off (room temperature). We placed individual third instar larvae onto the Peltier plate and simultaneously exposed the animal to photoconverting light for 20 seconds. CaMPARI2 fluorescence was imaged in live, intact larvae via confocal microscopy. Zeiss LSM 780 Axio examiner microscope, Plan-Apochromat 20x objective, and excitation wavelengths of 561nm and 488nm were used to image larval ventral nerve cord or peripheral sensory neurons. We mounted live intact larva onto microscope slide and immobilized the larva by placing a coverslip, as previously described (Im et al., 2018; Patel & Cox, 2017; Patel et al., 2022; Turner et al., 2016). Three dimensional CaMPARI2 fluorescence in ventral nerve cord localized downstream neurons was imaged at 607.28µm x 607.28µm (XY resolution) and 2µm z-slices. Regions of interests were identified and area normalized fluorescence intensity for red & green signals were obtained via Imaris 9.5 software. CaMPARI responses are reported as ratio of F_{red}/F_{green}. Statistical comparisons: Parametric data – Welch's t-test and non-parametric data – Mann-Whitney test.

PNS CAMPARI2 imaging: Sensory neuron CaMPARI2 responses were analyzed using custom FIJI macros that automatically detected cell bodies and sholl intensity analyses were performed using semi-automated custom FIJI macros (https://github.com/CoxLabGSU/CaMPARI-intensity-and-cold-plate-assay-analysis/branches) (Patel et al., 2022).

Cell body analysis – We created a set of three sequential macros that draw ROIs around the cell body, user verification of the ROIs and lastly quantification of fluorescence intensities. The first custom FIJI script generates maximum intensity projections of z-stacks, image masks were created by thresholding (Moments method) GFP signal, and next, background and dendritic branches removed using erode and dilate functions. At the end of background clearing only cell bodies remain, where Analyze particle function is used to draw ROIs around soma. The second FIJI script is used for manual verification of each ROI and manually redrawing any incorrect ROIs. Lastly, upon ROI verification, area normalized F_{red} and F_{green} intensities are quantified. As previously described (Fosque et al., 2015; Im et al., 2018; Patel & Cox, 2017; Patel et al., 2022; Turner et al., 2016), we report evoked photoconverted CaMPARI signal as F_{red}/F_{green} ratio. Statistical comparisons: Non-parametric data – Mann-Whitney test.

1412 Sholl intensity analysis – Sholl intensity analysis was performed using a set of two
1413 custom FIJI scripts as previously described (Patel et al., 2022). Briefly, we first perform
1414 background clearing by manually thresholding the GFP signal and select all branches and soma
1415 of neuron of interest using the "Wand Tool" in FIJI and then a mask of neuron of interest is
1416 created. The second FIJI script draws five-pixel wide radial ROIs at a single pixel interval, here
1417 only the dendrites and soma from the neuron of interest are selected at each radial interval. After
1418 Sholl ROIs are drawn, area and area normalized F_{red} and F_{green} fluorescence intensities are
1419 extracted for each radial step away from the soma. Similar to CaMPARI cell body analysis, we
1420 CaMPARI2 signal as F_{red}/F_{green} ratios away from the soma.
1421
1422 Ventral nerve cord CaMPARI imaging: We utilized Pan-neural (*R57C10*^{GAL4}*>CaMPARI*) driver
1423 to visualize ventral nerve cord Ca^{2+} responses to various stimuli including innocuous touch,
1424 noxious heat (45°C) and noxious cold (6°C). Stimulus and photoconverting light were delivered
1425 for 20 seconds. Whole ventral nerve cord was imaged at 607.28µm x 607.28µm (XY resolution)
1426 and 2µm z-slices. The rest of the stimulus delivery and imaging was similar to previously
1427 described CaMPARI experiments. No statistical analyses were performed.
1428
1429 **CIII activation and second order neuron GCaMP imaging**
1430 CIII md neuron-evoked responses in downstream neurons were evaluated by using
1431 optogenetics and GCaMP. We expressed *lexAop-CsCrimson* in CIII md neurons using
1432 *R83B04*^{lexA} and used downstream neuron specific *GAL4* to drive expression of *GCaMP6m*. For
1433 experimental condition, all adult animals in the genetic cross were reared in ATR (1500µM)
1434 supplemented food and subsequently F1 progeny were also raised in food containing ATR. For
1435 control condition, adult flies and F1 progeny were raised in standard cornmeal-molasses-agar
1436 diet. Both control and experimental crosses were reared in 24hr dark. We mounted live intact
1437 third instar larva in between microscope slide and a coverslip. Larval ventral nerve cord and cells
1438 of interest were located using epifluorescence on Zeiss LSM 780 confocal microscope. Larval
1439 GCaMP6 responses were allowed to return to baseline for at least 2 minutes. Time-lapse
1440 acquisition was imaged at 250.06µm x 250.06µm x 307.2ms using 488nm laser wavelength. CIII
1441 md neural activation was performed using two oblique 617nm leds (Thorlabs M617F2 and
1442 M79L01) that were manually operated using Thorlabs led controller (Thorlabs DC4100 and
1443 DC4100-hub). We performed three sequential neural activations using the following paradigm
1444 was used: Baseline light off (30 seconds)-> neural activation (617nm for 15 seconds)-> light off
1445 (30 seconds)-> neural activation (617nm for 15 seconds)-> light off (30 seconds)-> neural
1446 activation (617nm for 15 seconds)-> light off (30 seconds). Time-lapse videos were stabilized
1447 using Stack reg – Rigid transformation in FIJI (Linkert et al., 2010; Schindelin et al., 2012;
1448 Thevenaz et al., 1998). Regions of interest were manually drawn and area normalized GCaMP
1449 fluorescence over time was exported. We report changes in GCaMP6m fluorescence as $\Delta F/F$
1450 $=(F-F_{prestimulus})/ F_{prestimulus}*100$ and max $\Delta F/F$ for each of the three neural activation epochs.

Statistical comparisons: Parametric data – Welch's t-test and non-parametric data – Mann-Whitney test.

Statistics and data visualization

Statistical analyses were performed using r (Fisher's exact test) and GraphPad Prism. All graphical visualization of the data were created using Prism GraphPad. Details on specific statistical tests are listed in the respective methods section.

Table 1: Drosophila melanogaster strains used in this study

Designation	Nomenclature	Source or reference	Identifier
w1118		BDSC	3605
ChETA	*UAS-ChETA::YFP*	BDSC	36495
CaMPARI2	*UAS-CaMPARI2*	BDSC	78317
TnT	*UAS-TeTxLC.tnt-E2*	BDSC	28837
CsChrimson	*LexAop2-CsChrimson.tdTomato*	BDSC	82183
GCaMP6m	*UAS-GCaMP6m*	BDSC	42748
Pan-neural CaMPARI	*R57C10^{GAL4}, UAS-CaMPARI*	BDSC	58763
CIII>ChETA	*19-12^{GAL4}, UAS-ChETA::YFP*	BDSC	36495
CIII	*19-12 - GAL4*		
CIII	*R83B04 - lexA*	This Study	
Ch	*IAV - GAL4*	BDSC	52273
CIV	*ppk - GAL4*	BDSC	32079
Empty - GAL4	*pBDPGAL4Uw*	BDSC	68384
All Basin'	*R72F11 - GAL4*	BDSC	39786
All Basin''	*R57F07 - GAL4*	BDSC	46389
Basin-1	*R20B01 - GAL4*	BDSC	48873
Basin-2	*SS00739 - splitGAL4*	Zlatic Lab	
Basin-4	*SS00740 - splitGAL4*	Zlatic Lab	
A00c	*R71A10 - GAL4*	BDSC	39562
A05q	*R47D07 - GAL4*	BDSC	50304
Goro	*R69F06 - GAL4*	BDSC	39497
Chair-1	*SS00911 - splitGAL4*	Zlatic Lab	
DnB'	*IT4051 - GAL4*	Grueber Lab	
DnB''	*IT412 - GAL4*	BDSC	63300
mCSI	*R94B10 - GAL4*	BDSC	41325
A09e	*SS00878 - splitGAL4*	Zlatic Lab	
A08n	*R82E12 - GAL4*	BDSC	40153
R61A01/TePns	*R61A01 - GAL4*	BDSC	39269

Data availability statement

The original contributions presented in the study are included in the article/Supplementary material, further inquiries can be directed to the corresponding author.

Conflict of Interest

The authors declare that the research was conducted in the absence of any commercial or financial relationships that could be construed as a potential conflict of interest.

Author Contributions

Conceptualization: AAP and DNC. Methodology: AAP, and DNC. Cold-plate assays: AAP; Optogenetics, AAP; Calcium imaging: AAP. Statistics and other formal analyses: AAP. EM Connectome analysis: AAP and AC. Writing – Original Draft: AAP and DNC; Writing – Review & Editing: AAP, AC and DNC. Visualization: AAP. Supervision: DNC. Funding acquisition: DNC.

Funding

This work was supported by NIH R01 NS115209 (to DNC). AAP was supported by a Brains & Behavior Fellowship, a 2CI Neurogenomics Fellowship, and a Kenneth W. and Georganne F. Honeycutt Fellowship from Georgia State University. AC thanks the Wellcome Trust (award 205038/Z/16/Z and 205038/A/16/Z) and the HHMI Janelia Research Campus for funding.

Acknowledgments

We thank members of Cox Lab and Michael J. Galko (MD Anderson Cancer Center) for critical comments on the manuscript. We thank the Janelia Visiting Scientist program hosted by HHMI Janelia Research Campus for providing critical training in EM connectomics. We acknowledge the Imaging Core Facility of Georgia State University for training and instrument support associated with this work.

References

Andrade, I. V., Riebli, N., Nguyen, B. M., Omoto, J. J., Cardona, A., & Hartenstein, V. (2019, Feb 4). Developmentally Arrested Precursors of Pontine Neurons Establish an Embryonic Blueprint of the Drosophila Central Complex. *Curr Biol, 29*(3), 412-425 e413. https://doi.org/10.1016/j.cub.2018.12.012

Arnadóttir, J., O'Hagan, R., Chen, Y., Goodman, M. B., & Chalfie, M. (2011, 2011/8//). The DEG/ENaC protein MEC-10 regulates the transduction channel complex in Caenorhabditis elegans touch receptor neurons. *The Journal of neuroscience : the official journal of the Society for Neuroscience, 31*(35), 12695-12704. https://doi.org/10.1523/JNEUROSCI.4580-10.2011

Babcock, D. T., Landry, C., & Galko, M. J. (2009, 2009/5//). Cytokine signaling mediates UV-induced nociceptive sensitization in Drosophila larvae. *Current biology : CB, 19*(10), 799-806. https://doi.org/10.1016/j.cub.2009.03.062

Babcock, Daniel T., Shi, S., Jo, J., Shaw, M., Gutstein, Howard B., & Galko, Michael J. (2011, 2011/9//). Hedgehog Signaling Regulates Nociceptive Sensitization. *Current Biology, 21*(18), 1525-1533. https://doi.org/10.1016/j.cub.2011.08.020

Bandell, M., & Patapoutian, A. (2009, 2009/12//). Itching for insight. *Cell, 139*(7), 1224-1226. https://doi.org/10.1016/j.cell.2009.12.012

Bellardita, C., & Kiehn, O. (2015, Jun 1). Phenotypic characterization of speed-associated gait changes in mice reveals modular organization of locomotor networks. *Curr Biol, 25*(11), 1426-1436. https://doi.org/10.1016/j.cub.2015.04.005

Bentley, B., Branicky, R., Barnes, C. L., Chew, Y. L., Yemini, E., Bullmore, E. T., Vértes, P. E., & Schafer, W. R. (2016, 2016/12//). The Multilayer Connectome of Caenorhabditis elegans. *PLOS Computational Biology, 12*(12), e1005283-e1005283. https://doi.org/10.1371/journal.pcbi.1005283

Berck, M. E., Khandelwal, A., Claus, L., Hernandez-Nunez, L., Si, G., Tabone, C. J., Li, F., Truman, J. W., Fetter, R. D., Louis, M., Samuel, A. D. T., & Cardona, A. (2016). The wiring diagram of a glomerular olfactory system. https://doi.org/10.7554/eLife.14859.001

Berkowitz, A., Roberts, A., & Soffe, S. R. (2010). Roles for multifunctional and specialized spinal interneurons during motor pattern generation in tadpoles, zebrafish larvae, and turtles. *Front Behav Neurosci, 4*, 36. https://doi.org/10.3389/fnbeh.2010.00036

Burgos, A., Honjo, K., Ohyama, T., Qian, C. S., Shin, G. J.-e., Gohl, D. M., Silies, M., Tracey, W. D., Zlatic, M., Cardona, A., & Grueber, W. B. (2018, 2018/3//). Nociceptive interneurons control modular motor pathways to promote escape behavior in Drosophila. *eLife, 7*. https://doi.org/10.7554/eLife.26016

Bushnell, M. C., Duncan, G. H., Dubner, R., Jones, R. L., & Maixner, W. (1985, May). Attentional influences on noxious and innocuous cutaneous heat detection in humans and monkeys. *J Neurosci, 5*(5), 1103-1110. https://doi.org/10.1523/JNEUROSCI.05-05-01103.1985

Caldwell, J. C., Miller, M. M., Wing, S., Soll, D. R., & Eberl, D. F. (2003, 2003/12/23). Dynamic analysis of larval locomotion in Drosophila chordotonal organ mutants. *Proceedings of the National Academy of Sciences, 100*(26), 16053-16058. https://doi.org/10.1073/pnas.2535546100

Carreira-Rosario, A., Zarin, A. A., Clark, M. Q., Manning, L., Fetter, R. D., Cardona, A., & Doe, C. Q. (2018, 2018/8//). MDN brain descending neurons coordinately activate backward and inhibit forward locomotion. *eLife, 7*. https://doi.org/10.7554/eLife.38554

Cho, H., & Oh, U. (2013, 2013/12//). Anoctamin 1 mediates thermal pain as a heat sensor. *Current neuropharmacology, 11*(6), 641-651. https://doi.org/10.2174/1570159X113119990038

Clark, M. Q., Zarin, A. A., Carreira-Rosario, A., & Doe, C. Q. (2018, 2018/12//). Neural circuits driving larval locomotion in Drosophila. *Neural Development, 13*(1), 6-6. https://doi.org/10.1186/s13064-018-0103-z

Cooney, P. C., Li, W., Huang, Y., Hormigo, R., Tabachnik, T., Hillman, E. M. C., Grueber, W. B., & Zarin, A. A. (2023). Neuromuscular Basis of Drosophila larval escape behavior. *bioRxiv*, 2023.2002.2001.526733. https://doi.org/10.1101/2023.02.01.526733

Corfas, R. A., & Vosshall, L. B. (2015, 2015/12//). The cation channel TRPA1 tunes mosquito thermotaxis to host temperatures. *eLife, 4*. https://doi.org/10.7554/eLife.11750

Coste, B., Mathur, J., Schmidt, M., Earley, T. J., Ranade, S., Petrus, M. J., Dubin, A. E., & Patapoutian, A. (2010, 2010/10//). Piezo1 and Piezo2 are essential components of distinct mechanically activated cation channels. *Science (New York, N.Y.), 330*(6000), 55-60. https://doi.org/10.1126/science.1193270

Dannhauser, S., Lux, T. J., Hu, C., Selcho, M., Chen, J. T., Ehmann, N., Sachidanandan, D., Stopp, S., Pauls, D., Pawlak, M., Langenhan, T., Soba, P., Rittner, H. L., & Kittel, R. J. (2020, Sep 30). Antinociceptive modulation by the adhesion GPCR CIRL promotes mechanosensory signal discrimination. *eLife, 9*. https://doi.org/10.7554/eLife.56738

Derby, C. D., Kozma, M. T., Senatore, A., & Schmidt, M. (2016, Jun). Molecular Mechanisms of Reception and Perireception in Crustacean Chemoreception: A Comparative Review. *Chem Senses, 41*(5), 381-398. https://doi.org/10.1093/chemse/bjw057

Dietrich, S., Company, C., Song, K., Lowenstein, E. D., Riedel, L., Birchmeier, C., Gargiulo, G., & Zampieri, N. (2022, Nov 11). Molecular identity of proprioceptor subtypes innervating

different muscle groups in mice. *Nat Commun, 13*(1), 6867. https://doi.org/10.1038/s41467-022-34589-8

Eichler, K., Li, F., Litwin-Kumar, A., Park, Y., Andrade, I., Schneider-Mizell, C. M., Saumweber, T., Huser, A., Eschbach, C., Gerber, B., Fetter, R. D., Truman, J. W., Priebe, C. E., Abbott, L. F., Thum, A. S., Zlatic, M., & Cardona, A. (2017, 2017/8//). The complete connectome of a learning and memory centre in an insect brain. *Nature, 548*(7666), 175-182. https://doi.org/10.1038/nature23455

Eschbach, C., Fushiki, A., Winding, M., Schneider-Mizell, C. M., Shao, M., Arruda, R., Eichler, K., Valdes-Aleman, J., Ohyama, T., Thum, A. S., Gerber, B., Fetter, R. D., Truman, J. W., Litwin-Kumar, A., Cardona, A., & Zlatic, M. (2020, Apr). Recurrent architecture for adaptive regulation of learning in the insect brain. *Nat Neurosci, 23*(4), 544-555. https://doi.org/10.1038/s41593-020-0607-9

Eschbach, C., & Zlatic, M. (2020, Dec). Useful road maps: studying Drosophila larva's central nervous system with the help of connectomics. *Curr Opin Neurobiol, 65*, 129-137. https://doi.org/10.1016/j.conb.2020.09.008

Fosque, B. F., Sun, Y., Dana, H., Yang, C. T., Ohyama, T., Tadross, M. R., Patel, R., Zlatic, M., Kim, D. S., Ahrens, M. B., Jayaraman, V., Looger, L. L., & Schreiter, E. R. (2015, 2015/2//). Labeling of active neural circuits in vivo with designed calcium integrators. *Science, 347*(6223), 755-760. https://doi.org/10.1126/science.1260922

Fowler, M. A., & Montell, C. (2013, 2013/3//). Drosophila TRP channels and animal behavior. *Life sciences, 92*(8-9), 394-403. https://doi.org/10.1016/j.lfs.2012.07.029

Frank, D. D., Enjin, A., Jouandet, G. C., Zaharieva, E. E., Para, A., Stensmyr, M. C., & Gallio, M. (2017, 2017/8//). Early Integration of Temperature and Humidity Stimuli in the Drosophila Brain. *Current Biology, 27*(15), 2381-2388.e2384. https://doi.org/10.1016/j.cub.2017.06.077

Frank, D. D., Jouandet, G. C., Kearney, P. J., Macpherson, L. J., & Gallio, M. (2015, 2015/3//). Temperature representation in the Drosophila brain. *Nature, 519*(7543), 358-361. https://doi.org/10.1038/nature14284

Freeman, E. G., & Dahanukar, A. (2015). Molecular neurobiology of Drosophila taste. *Current Opinion in Neurobiology, 34*, 140-148. https://doi.org/10.1016/j.conb.2015.06.001

Fushiki, A., Zwart, M. F., Kohsaka, H., Fetter, R. D., Cardona, A., & Nose, A. (2016, 2016/2//). A circuit mechanism for the propagation of waves of muscle contraction in Drosophila. *eLife, 5*. https://doi.org/10.7554/eLife.13253

Gallio, M., Ofstad, T. A., Macpherson, L. J., Wang, J. W., & Zuker, C. S. (2011, Feb 18). The coding of temperature in the Drosophila brain. *Cell, 144*(4), 614-624. https://doi.org/10.1016/j.cell.2011.01.028

Gerhard, S., Andrade, I., Fetter, R. D., Cardona, A., & Schneider-Mizell, C. M. (2017, 2017/10//). Conserved neural circuit structure across Drosophila larval development revealed by comparative connectomics. *eLife, 6*. https://doi.org/10.7554/eLife.29089

Green, C. S., & Soffe, S. R. (1996, 1996/02/01). Transitions between two different motor patterns in Xenopus embryos. *Journal of Comparative Physiology A, 178*(2), 279-291. https://doi.org/10.1007/BF00188169

Gunaydin, L. A., Yizhar, O., Berndt, A., Sohal, V. S., Deisseroth, K., & Hegemann, P. (2010, 2010/3//). Ultrafast optogenetic control. *Nature Neuroscience, 13*(3), 387-392. https://doi.org/10.1038/nn.2495

He, L., Gulyanon, S., Skanata, M. M., Karagyozov, D., Heckscher, E., Krieg, M., Tschekpenakis, G., Gershow, M., & Tracey, D. (2018, 2018/11//). Proprioceptive neurons of larval Drosophila melanogaster show direction selective activity requiring the mechanosensory channel TMC. *bioRxiv*, 463216-463216. https://doi.org/10.1101/463216

Heckscher, Ellie S., Zarin, Aref A., Faumont, S., Clark, Matthew Q., Manning, L., Fushiki, A., Schneider-Mizell, Casey M., Fetter, Richard D., Truman, James W., Zwart, Maarten F., Landgraf, M., Cardona, A., Lockery, Shawn R., & Doe, Chris Q. (2015, 2015/10//). Even-Skipped+ Interneurons Are Core Components of a Sensorimotor Circuit that Maintains Left-Right Symmetric Muscle Contraction Amplitude. *Neuron, 88*(2), 314-329. https://doi.org/10.1016/J.NEURON.2015.09.009

Herculano-Houzel, S. (2009). The human brain in numbers: a linearly scaled-up primate brain. *Front Hum Neurosci, 3*, 31. https://doi.org/10.3389/neuro.09.031.2009

Hernandez-Nunez, L., Chen, A., Budelli, G., Berck, M. E., Richter, V., Rist, A., Thum, A. S., Cardona, A., Klein, M., Garrity, P., & Samuel, A. D. T. (2021). Synchronous and opponent thermosensors use flexible cross-inhibition to orchestrate thermal homeostasis. *Science Advances, 7*(35), eabg6707. https://doi.org/doi:10.1126/sciadv.abg6707

Himmel, N. J., Letcher, J. M., Sakurai, A., Gray, T. R., Benson, M. N., & Cox, D. N. (2019, Nov 11). Drosophila menthol sensitivity and the Precambrian origins of transient receptor potential-dependent chemosensation. *Philos Trans R Soc Lond B Biol Sci, 374*(1785), 20190369. https://doi.org/10.1098/rstb.2019.0369

Himmel, N. J., Patel, A. A., & Cox, D. N. (2017). *Invertebrate Nociception* (Vol. 1). Oxford University Press. https://doi.org/10.1093/acrefore/9780190264086.013.166

Himmel, N. J., Sakurai, A., Patel, A. A., Bhattacharjee, S., Letcher, J. M., Benson, M. N., Gray, T. R., Cymbalyuk, G. S., & Cox, D. N. (2023, Jan 23). Chloride-dependent mechanisms of multimodal sensory discrimination and nociceptive sensitization in Drosophila. *eLife, 12*. https://doi.org/10.7554/eLife.76863

Hiramoto, A., Jonaitis, J., Niki, S., Kohsaka, H., Fetter, R. D., Cardona, A., Pulver, S. R., & Nose, A. (2021, May 19). Regulation of coordinated muscular relaxation in Drosophila larvae by a pattern-regulating intersegmental circuit. *Nat Commun, 12*(1), 2943. https://doi.org/10.1038/s41467-021-23273-y

Hu, C., Petersen, M., Hoyer, N., Spitzweck, B., Tenedini, F., Wang, D., Gruschka, A., Burchardt, L. S., Szpotowicz, E., Schweizer, M., Guntur, A. R., Yang, C.-H., & Soba, P. (2017, 2017/8//). Sensory integration and neuromodulatory feedback facilitate Drosophila mechanonociceptive behavior. *Nature Neuroscience, 20*(8), 1085-1095. https://doi.org/10.1038/nn.4580

Hu, Y., Wang, C., Yang, L., Pan, G., Liu, H., Yu, G., & Ye, B. (2020, Dec 21). A Neural Basis for Categorizing Sensory Stimuli to Enhance Decision Accuracy. *Curr Biol, 30*(24), 4896-4909 e4896. https://doi.org/10.1016/j.cub.2020.09.045

Huang, Y., & Zarin, A. A. (2022). A premotor microcircuit to generate behavior-specific muscle activation patterns in Drosophila larvae. *bioRxiv*, 2022.2008.2018.504452. https://doi.org/10.1101/2022.08.18.504452

Huckesfeld, S., Schlegel, P., Miroschnikow, A., Schoofs, A., Zinke, I., Haubrich, A. N., Schneider-Mizell, C. M., Truman, J. W., Fetter, R. D., Cardona, A., & Pankratz, M. J. (2021, Jun 4). Unveiling the sensory and interneuronal pathways of the neuroendocrine connectome in Drosophila. *eLife, 10*. https://doi.org/10.7554/eLife.65745

Hwang, R. Y., Zhong, L., Xu, Y., Johnson, T., Zhang, F., Deisseroth, K., & Tracey, W. D. (2007, 2007/12//). Nociceptive Neurons Protect Drosophila Larvae from Parasitoid Wasps. *Current Biology, 17*(24), 2105-2116. https://doi.org/10.1016/j.cub.2007.11.029

Im, S. H., Patel, A. A., Cox, D. N., & Galko, M. J. (2018, 2018/5//). Drosophila Insulin receptor regulates the persistence of injury-induced nociceptive sensitization. *Disease Models & Mechanisms, 11*(5), dmm034231-dmm034231. https://doi.org/10.1242/dmm.034231

Im, S. H., Takle, K., Jo, J., Babcock, D. T., Ma, Z., Xiang, Y., & Galko, M. J. (2015). Tachykinin acts upstream of autocrine Hedgehog signaling during nociceptive sensitization in Drosophila. *eLife, 4*. https://doi.org/10.7554/eLife.10735

Imambocus, B. N., Zhou, F., Formozov, A., Wittich, A., Tenedini, F. M., Hu, C., Sauter, K., Macarenhas Varela, E., Heredia, F., Casimiro, A. P., Macedo, A., Schlegel, P., Yang, C. H., Miguel-Aliaga, I., Wiegert, J. S., Pankratz, M. J., Gontijo, A. M., Cardona, A., & Soba, P. (2022, Jan 10). A neuropeptidergic circuit gates selective escape behavior of Drosophila larvae. *Curr Biol, 32*(1), 149-163 e148. https://doi.org/10.1016/j.cub.2021.10.069

Imura, E., Shimada-Niwa, Y., Nishimura, T., Huckesfeld, S., Schlegel, P., Ohhara, Y., Kondo, S., Tanimoto, H., Cardona, A., Pankratz, M. J., & Niwa, R. (2020, Jun 8). The

Corazonin-PTTH Neuronal Axis Controls Systemic Body Growth by Regulating Basal Ecdysteroid Biosynthesis in Drosophila melanogaster. *Curr Biol, 30*(11), 2156-2165 e2155. https://doi.org/10.1016/j.cub.2020.03.050

Jenett, A., Rubin, Gerald M., Ngo, T.-T. B., Shepherd, D., Murphy, C., Dionne, H., Pfeiffer, Barret D., Cavallaro, A., Hall, D., Jeter, J., Iyer, N., Fetter, D., Hausenfluck, Joanna H., Peng, H., Trautman, Eric T., Svirskas, Robert R., Myers, Eugene W., Iwinski, Zbigniew R., Aso, Y., DePasquale, Gina M., Enos, A., Hulamm, P., Lam, Shing Chun B., Li, H.-H., Laverty, Todd R., Long, F., Qu, L., Murphy, Sean D., Rokicki, K., Safford, T., Shaw, K., Simpson, Julie H., Sowell, A., Tae, S., Yu, Y., & Zugates, Christopher T. (2012, 2012/10//). A GAL4-Driver Line Resource for Drosophila Neurobiology. *Cell Reports, 2*(4), 991-1001. https://doi.org/10.1016/j.celrep.2012.09.011

Jovanic, T., Schneider-Mizell, C. M., Shao, M., Masson, J.-B., Denisov, G., Fetter, R. D., Mensh, B. D., Truman, J. W., Cardona, A., & Zlatic, M. (2016, 2016/10//). Competitive Disinhibition Mediates Behavioral Choice and Sequences in Drosophila. *Cell, 167*(3), 858-870.e819. https://doi.org/10.1016/j.cell.2016.09.009

Jovanic, T., Winding, M., Cardona, A., Truman, J. W., Gershow, M., & Zlatic, M. (2019, Feb 18). Neural Substrates of Drosophila Larval Anemotaxis. *Curr Biol, 29*(4), 554-566 e554. https://doi.org/10.1016/j.cub.2019.01.009

Kaneko, T., Macara, A. M., Li, R., Hu, Y., Iwasaki, K., Dunnings, Z., Firestone, E., Horvatic, S., Guntur, A., Shafer, O. T., Yang, C.-H., Zhou, J., & Ye, B. (2017, 2017/8//). Serotonergic Modulation Enables Pathway-Specific Plasticity in a Developing Sensory Circuit in Drosophila. *Neuron, 95*(3), 623-638.e624. https://doi.org/10.1016/j.neuron.2017.06.034

Klein, M., Afonso, B., Vonner, A. J., Hernandez-Nunez, L., Berck, M., Tabone, C. J., Kane, E. A., Pieribone, V. A., Nitabach, M. N., Cardona, A., Zlatic, M., Sprecher, S. G., Gershow, M., Garrity, P. A., & Samuel, A. D. (2015, Jan 13). Sensory determinants of behavioral dynamics in Drosophila thermotaxis. *Proc Natl Acad Sci U S A, 112*(2), E220-229. https://doi.org/10.1073/pnas.1416212112

Kohsaka, H., Guertin, P. A., & Nose, A. (2017, 2017/5//). Neural Circuits Underlying Fly Larval Locomotion. *Current Pharmaceutical Design, 23*(12), 1722-1733. https://doi.org/10.2174/1381612822666161208120835

Kohsaka, H., Takasu, E., Morimoto, T., & Nose, A. (2014, 2014/11//). A Group of Segmental Premotor Interneurons Regulates the Speed of Axial Locomotion in Drosophila Larvae. *Current Biology, 24*(22), 2632-2642. https://doi.org/10.1016/j.cub.2014.09.026

Kohsaka, H., Zwart, M. F., Fushiki, A., Fetter, R. D., Truman, J. W., Cardona, A., & Nose, A. (2019, 2019/06/14). Regulation of forward and backward locomotion through intersegmental feedback circuits in Drosophila larvae. *Nature Communications, 10*(1), 2654. https://doi.org/10.1038/s41467-019-10695-y

Larderet, I., Fritsch, P. M. J., Gendre, N., Larisa Neagu-Maier, G., Fetter, R. D., Schneider-Mizell, C. M., Truman, J. W., Zlatic, M., Cardona, A., & Sprecher, S. G. (2017). Organization of the Drosophila larval visual circuit. https://doi.org/10.7554/eLife.28387.001

Leung, N. Y., & Montell, C. (2017, Oct 6). Unconventional Roles of Opsins. *Annu Rev Cell Dev Biol, 33*, 241-264. https://doi.org/10.1146/annurev-cellbio-100616-060432

Liao, J. C., & Fetcho, J. R. (2008, Nov 26). Shared versus specialized glycinergic spinal interneurons in axial motor circuits of larval zebrafish. *J Neurosci, 28*(48), 12982-12992. https://doi.org/10.1523/JNEUROSCI.3330-08.2008

Linkert, M., Rueden, C. T., Allan, C., Burel, J. M., Moore, W., Patterson, A., Loranger, B., Moore, J., Neves, C., Macdonald, D., Tarkowska, A., Sticco, C., Hill, E., Rossner, M., Eliceiri, K. W., & Swedlow, J. R. (2010, May 31). Metadata matters: access to image data in the real world. *J Cell Biol, 189*(5), 777-782. https://doi.org/10.1083/jcb.201004104

Liu, L., Yermolaieva, O., Johnson, W. A., Abboud, F. M., & Welsh, M. J. (2003, Mar). Identification and function of thermosensory neurons in Drosophila larvae. *Nat Neurosci, 6*(3), 267-273. https://doi.org/10.1038/nn1009

Lopez-Bellido, R., Himmel, N. J., Gutstein, H. B., Cox, D. N., & Galko, M. J. (2019, Nov 11). An assay for chemical nociception in Drosophila larvae. *Philos Trans R Soc Lond B Biol Sci, 374*(1785), 20190282. https://doi.org/10.1098/rstb.2019.0282

Macpherson, L. J., Zaharieva, E. E., Kearney, P. J., Alpert, M. H., Lin, T.-Y., Turan, Z., Lee, C.-H., & Gallio, M. (2015, 2015/12//). Dynamic labelling of neural connections in multiple colours by trans-synaptic fluorescence complementation. *Nature Communications, 6*(1), 10024-10024. https://doi.org/10.1038/ncomms10024

Maertens, T., Schöll, E., Ruiz, J., & Hövel, P. (2021, 2021/02/28/). Multilayer network analysis of C. elegans: Looking into the locomotory circuitry. *Neurocomputing, 427*, 238-261. https://doi.org/https://doi.org/10.1016/j.neucom.2020.11.015

Marder, E. (2012, Oct 4). Neuromodulation of neuronal circuits: back to the future. *Neuron, 76*(1), 1-11. https://doi.org/10.1016/j.neuron.2012.09.010

Mark, B., Lai, S. L., Zarin, A. A., Manning, L., Pollington, H. Q., Litwin-Kumar, A., Cardona, A., Truman, J. W., & Doe, C. Q. (2021, May 11). A developmental framework linking neurogenesis and circuit formation in the Drosophila CNS. *eLife, 10*. https://doi.org/10.7554/eLife.67510

Masson, J. B., Laurent, F., Cardona, A., Barre, C., Skatchkovsky, N., Zlatic, M., & Jovanic, T. (2020, Feb). Identifying neural substrates of competitive interactions and sequence

transitions during mechanosensory responses in Drosophila. *PLoS Genet, 16*(2), e1008589. https://doi.org/10.1371/journal.pgen.1008589

Miroschnikow, A., Schlegel, P., Schoofs, A., Hueckesfeld, S., Li, F., Schneider-Mizell, C. M., Fetter, R. D., Truman, J., Cardona, A., & Pankratz, M. J. (2018, 2018/7//). The Feeding Connectome: Convergence of Monosynaptic and Polysynaptic Sensory Paths onto Common Motor Outputs. *bioRxiv*, 368878-368878. https://doi.org/10.1101/368878

Moehring, F., Cowie, A. M., Menzel, A. D., Weyer, A. D., Grzybowski, M., Arzua, T., Geurts, A. M., Palygin, O., & Stucky, C. L. (2018, Jan 16). Keratinocytes mediate innocuous and noxious touch via ATP-P2X4 signaling. *eLife, 7*. https://doi.org/10.7554/eLife.31684

Montell, C. (2021, Mar 3). Drosophila sensory receptors-a set of molecular Swiss Army Knives. *Genetics, 217*(1), 1-34. https://doi.org/10.1093/genetics/iyaa011

Nakamura, K. (2018). Afferent pathways for autonomic and shivering thermoeffectors. *Handb Clin Neurol, 156*, 263-279. https://doi.org/10.1016/B978-0-444-63912-7.00016-3

Ohyama, T., Schneider-Mizell, C. M., Fetter, R. D., Aleman, J. V., Franconville, R., Rivera-Alba, M., Mensh, B. D., Branson, K. M., Simpson, J. H., Truman, J. W., Cardona, A., & Zlatic, M. (2015, 2015/4//). A multilevel multimodal circuit enhances action selection in Drosophila. *Nature, 520*(7549), 633-639. https://doi.org/10.1038/nature14297

Patel, A., & Cox, D. (2017). Behavioral and Functional Assays for Investigating Mechanisms of Noxious Cold Detection and Multimodal Sensory Processing in Drosophila Larvae. *BIO-PROTOCOL, 7*(13). https://doi.org/10.21769/BioProtoc.2388

Patel, A. A., Sakurai, A., Himmel, N. J., & Cox, D. N. (2022). Modality specific roles for metabotropic GABAergic signaling and calcium induced calcium release mechanisms in regulating cold nociception. *bioRxiv*, 2022.2005.2012.491647. https://doi.org/10.1101/2022.05.12.491647

Pfeiffer, B. D., Jenett, A., Hammonds, A. S., Ngo, T. T., Misra, S., Murphy, C., Scully, A., Carlson, J. W., Wan, K. H., Laverty, T. R., Mungall, C., Svirskas, R., Kadonaga, J. T., Doe, C. Q., Eisen, M. B., Celniker, S. E., & Rubin, G. M. (2008, Jul 15). Tools for neuroanatomy and neurogenetics in Drosophila. *Proc Natl Acad Sci U S A, 105*(28), 9715-9720. https://doi.org/10.1073/pnas.0803697105

Saalfeld, S., Cardona, A., Hartenstein, V., & Tomancak, P. (2009, Aug 1). CATMAID: collaborative annotation toolkit for massive amounts of image data. *Bioinformatics, 25*(15), 1984-1986. https://doi.org/10.1093/bioinformatics/btp266

Salvaterra, P. M., & Kitamoto, T. (2001, Aug). Drosophila cholinergic neurons and processes visualized with Gal4/UAS-GFP. *Brain Res Gene Expr Patterns, 1*(1), 73-82. https://doi.org/10.1016/s1567-133x(01)00011-4

Saumweber, T., Rohwedder, A., Schleyer, M., Eichler, K., Chen, Y.-c., Aso, Y., Cardona, A., Eschbach, C., Kobler, O., Voigt, A., Durairaja, A., Mancini, N., Zlatic, M., Truman, J. W., Thum, A. S., & Gerber, B. (2018, 2018/12//). Functional architecture of reward learning in mushroom body extrinsic neurons of larval Drosophila. *Nature Communications, 9*(1), 1104-1104. https://doi.org/10.1038/s41467-018-03130-1

Scheffer, L. K., Xu, C. S., Januszewski, M., Lu, Z., Takemura, S. Y., Hayworth, K. J., Huang, G. B., Shinomiya, K., Maitlin-Shepard, J., Berg, S., Clements, J., Hubbard, P. M., Katz, W. T., Umayam, L., Zhao, T., Ackerman, D., Blakely, T., Bogovic, J., Dolafi, T., Kainmueller, D., Kawase, T., Khairy, K. A., Leavitt, L., Li, P. H., Lindsey, L., Neubarth, N., Olbris, D. J., Otsuna, H., Trautman, E. T., Ito, M., Bates, A. S., Goldammer, J., Wolff, T., Svirskas, R., Schlegel, P., Neace, E., Knecht, C. J., Alvarado, C. X., Bailey, D. A., Ballinger, S., Borycz, J. A., Canino, B. S., Cheatham, N., Cook, M., Dreher, M., Duclos, O., Eubanks, B., Fairbanks, K., Finley, S., Forknall, N., Francis, A., Hopkins, G. P., Joyce, E. M., Kim, S., Kirk, N. A., Kovalyak, J., Lauchie, S. A., Lohff, A., Maldonado, C., Manley, E. A., McLin, S., Mooney, C., Ndama, M., Ogundeyi, O., Okeoma, N., Ordish, C., Padilla, N., Patrick, C. M., Paterson, T., Phillips, E. E., Phillips, E. M., Rampally, N., Ribeiro, C., Robertson, M. K., Rymer, J. T., Ryan, S. M., Sammons, M., Scott, A. K., Scott, A. L., Shinomiya, A., Smith, C., Smith, K., Smith, N. L., Sobeski, M. A., Suleiman, A., Swift, J., Takemura, S., Talebi, I., Tarnogorska, D., Tenshaw, E., Tokhi, T., Walsh, J. J., Yang, T., Horne, J. A., Li, F., Parekh, R., Rivlin, P. K., Jayaraman, V., Costa, M., Jefferis, G. S., Ito, K., Saalfeld, S., George, R., Meinertzhagen, I. A., Rubin, G. M., Hess, H. F., Jain, V., & Plaza, S. M. (2020, Sep 7). A connectome and analysis of the adult Drosophila central brain. *eLife, 9*. https://doi.org/10.7554/eLife.57443

Schindelin, J., Arganda-Carreras, I., Frise, E., Kaynig, V., Longair, M., Pietzsch, T., Preibisch, S., Rueden, C., Saalfeld, S., Schmid, B., Tinevez, J. Y., White, D. J., Hartenstein, V., Eliceiri, K., Tomancak, P., & Cardona, A. (2012, Jun 28). Fiji: an open-source platform for biological-image analysis. *Nat Methods, 9*(7), 676-682. https://doi.org/10.1038/nmeth.2019

Schlegel, P., Texada, M. J., Miroschnikow, A., Schoofs, A., Hückesfeld, S., Peters, M., Schneider-Mizell, C. M., Lacin, H., Li, F., Fetter, R. D., Truman, J. W., Cardona, A., & Pankratz, M. J. (2016, 2016/11//). Synaptic transmission parallels neuromodulation in a central food-intake circuit. *eLife, 5*. https://doi.org/10.7554/eLife.16799

Schneider-Mizell, C. M., Gerhard, S., Longair, M., Kazimiers, T., Li, F., Zwart, M. F., Champion, A., Midgley, F. M., Fetter, R. D., Saalfeld, S., & Cardona, A. (2016, 2016/3//). Quantitative neuroanatomy for connectomics in Drosophila. *eLife, 5*. https://doi.org/10.7554/eLife.12059

Scholz, N., Gehring, J., Guan, C., Ljaschenko, D., Fischer, R., Lakshmanan, V., Kittel, R. J., & Langenhan, T. (2015, 2015/05/12/). The Adhesion GPCR Latrophilin/CIRL Shapes Mechanosensation. *Cell Reports, 11*(6), 866-874. https://doi.org/https://doi.org/10.1016/j.celrep.2015.04.008

Scholz, N., Guan, C., Nieberler, M., Grotemeyer, A., Maiellaro, I., Gao, S., Beck, S., Pawlak, M., Sauer, M., Asan, E., Rothemund, S., Winkler, J., Promel, S., Nagel, G., Langenhan, T., & Kittel, R. J. (2017, Aug 8). Mechano-dependent signaling by Latrophilin/CIRL quenches cAMP in proprioceptive neurons. *eLife, 6*. https://doi.org/10.7554/eLife.28360

Shannon, P., Markiel, A., Ozier, O., Baliga, N. S., Wang, J. T., Ramage, D., Amin, N., Schwikowski, B., & Ideker, T. (2003, Nov). Cytoscape: a software environment for integrated models of biomolecular interaction networks. *Genome Res, 13*(11), 2498-2504. https://doi.org/10.1101/gr.1239303

Sweeney, S. T., Broadie, K., Keane, J., Niemann, H., & O'Kane, C. J. (1995, Feb). Targeted expression of tetanus toxin light chain in Drosophila specifically eliminates synaptic transmission and causes behavioral defects. *Neuron, 14*(2), 341-351. https://doi.org/10.1016/0896-6273(95)90290-2

Taghert, P. H., & Nitabach, M. N. (2012, Oct 4). Peptide neuromodulation in invertebrate model systems. *Neuron, 76*(1), 82-97. https://doi.org/10.1016/j.neuron.2012.08.035

Takagi, S., Cocanougher, B. T., Niki, S., Miyamoto, D., Kohsaka, H., Kazama, H., Fetter, R. D., Truman, J. W., Zlatic, M., Cardona, A., & Nose, A. (2017, 2017/12//). Divergent Connectivity of Homologous Command-like Neurons Mediates Segment-Specific Touch Responses in Drosophila. *Neuron, 96*(6), 1373-1387.e1376. https://doi.org/10.1016/j.neuron.2017.10.030

Talpalar, A. E., Bouvier, J., Borgius, L., Fortin, G., Pierani, A., & Kiehn, O. (2013, Aug 1). Dual-mode operation of neuronal networks involved in left-right alternation. *Nature, 500*(7460), 85-88. https://doi.org/10.1038/nature12286

Tastekin, I., Khandelwal, A., Tadres, D., Fessner, N. D., Truman, J. W., Zlatic, M., Cardona, A., & Louis, M. (2018, Nov 22). Sensorimotor pathway controlling stopping behavior during chemotaxis in the Drosophila melanogaster larva. *eLife, 7*. https://doi.org/10.7554/eLife.38740

Tenedini, F. M., Sáez González, M., Hu, C., Pedersen, L. H., Petruzzi, M. M., Spitzweck, B., Wang, D., Richter, M., Petersen, M., Szpotowicz, E., Schweizer, M., Sigrist, S. J., Calderon de Anda, F., & Soba, P. (2019, 2019/08/05). Maintenance of cell type-specific connectivity and circuit function requires Tao kinase. *Nature Communications, 10*(1), 3506. https://doi.org/10.1038/s41467-019-11408-1

Thevenaz, P., Ruttimann, U. E., & Unser, M. (1998). A pyramid approach to subpixel registration based on intensity. *IEEE Trans Image Process, 7*(1), 27-41. https://doi.org/10.1109/83.650848

Tracey, W. D., Wilson, R. I., Laurent, G., & Benzer, S. (2003, 2003/4//). painless, a Drosophila gene essential for nociception. *Cell, 113*(2), 261-273. http://www.ncbi.nlm.nih.gov/pubmed/12705873

Turner, H. N., Armengol, K., Patel, A. A., Himmel, N. J., Sullivan, L., Iyer, S. C., Bhattacharya, S., Iyer, E. P. R., Landry, C., Galko, M. J., & Cox, D. N. (2016, Dec 5). The TRP Channels Pkd2, NompC, and Trpm Act in Cold-Sensing Neurons to Mediate Unique Aversive Behaviors to Noxious Cold in Drosophila. *Curr Biol, 26*(23), 3116-3128. https://doi.org/10.1016/j.cub.2016.09.038

Turner, H. N., Patel, A. A., Cox, D. N., & Galko, M. J. (2018). Injury-induced cold sensitization in Drosophila larvae involves behavioral shifts that require the TRP channel Brv1. *PLoS One, 13*(12), e0209577. https://doi.org/10.1371/journal.pone.0209577

Vaadia, R., Li, W., Voleti, V., Singhania, A., Hillman, E. M. C., & Grueber, W. B. (2018, 2018/11//). Characterization of proprioceptive system dynamics in behaving Drosophila larvae using high-speed volumetric microscopy. *bioRxiv*, 467274-467274. https://doi.org/10.1101/467274

Valdes-Aleman, J., Fetter, R. D., Sales, E. C., Heckman, E. L., Venkatasubramanian, L., Doe, C. Q., Landgraf, M., Cardona, A., & Zlatic, M. (2021). Comparative Connectomics Reveals How Partner Identity, Location, and Activity Specify Synaptic Connectivity in Drosophila. *Neuron, 109*(1), 105-122.e107. https://doi.org/10.1016/j.neuron.2020.10.004

Vogelstein, J. T., Park, Y., Ohyama, T., Kerr, R. A., Truman, J. W., Priebe, C. E., & Zlatic, M. (2014, 2014/4//). Discovery of Brainwide Neural-Behavioral Maps via Multiscale Unsupervised Structure Learning. *Science, 344*(6182), 386-392. https://doi.org/10.1126/science.1250298

Vogt, K., Zimmerman, D. M., Schlichting, M., Hernandez-Nunez, L., Qin, S., Malacon, K., Rosbash, M., Pehlevan, C., Cardona, A., & Samuel, A. D. T. (2021, Jan). Internal state configures olfactory behavior and early sensory processing in Drosophila larvae. *Sci Adv, 7*(1). https://doi.org/10.1126/sciadv.abd6900

Ward, L., Wright, E., & McMahon, S. B. (1996, Jan). A comparison of the effects of noxious and innocuous counterstimuli on experimentally induced itch and pain. *Pain, 64*(1), 129-138. https://doi.org/10.1016/0304-3959(95)00080-1

Winding, M., Pedigo, B. D., Barnes, C. L., Patsolic, H. G., Park, Y., Kazimiers, T., Fushiki, A., Andrade, I. V., Khandelwal, A., Valdes-Aleman, J., Li, F., Randel, N., Barsotti, E., Correia, A., Fetter, R. D., Hartenstein, V., Priebe, C. E., Vogelstein, J. T., Cardona, A., & Zlatic, M. (2023, Mar 10). The connectome of an insect brain. *Science, 379*(6636), eadd9330. https://doi.org/10.1126/science.add9330

Wu, P., Arris, D., Grayson, M., Hung, C. N., & Ruparel, S. (2018). Characterization of sensory neuronal subtypes innervating mouse tongue. *PLoS One, 13*(11), e0207069. https://doi.org/10.1371/journal.pone.0207069

Xiao, R., & Xu, X. Z. S. (2021, Feb 10). Temperature Sensation: From Molecular Thermosensors to Neural Circuits and Coding Principles. *Annu Rev Physiol, 83*, 205-230. https://doi.org/10.1146/annurev-physiol-031220-095215

Yoshino, J., Morikawa, R. K., Hasegawa, E., & Emoto, K. (2017, 2017/8//). Neural Circuitry that Evokes Escape Behavior upon Activation of Nociceptive Sensory Neurons in Drosophila Larvae. *Current Biology, 27*(16), 2499-2504.e2493. https://doi.org/10.1016/j.cub.2017.06.068

Zarin, A. A., Mark, B., Cardona, A., Litwin-Kumar, A., & Doe, C. Q. (2019, Dec 23). A multilayer circuit architecture for the generation of distinct locomotor behaviors in Drosophila. *eLife, 8*. https://doi.org/10.7554/eLife.51781

Zheng, Z., Lauritzen, J. S., Perlman, E., Robinson, C. G., Nichols, M., Milkie, D., Torrens, O., Price, J., Fisher, C. B., Sharifi, N., Calle-Schuler, S. A., Kmecova, L., Ali, I. J., Karsh, B., Trautman, E. T., Bogovic, J. A., Hanslovsky, P., Jefferis, G., Kazhdan, M., Khairy, K., Saalfeld, S., Fetter, R. D., & Bock, D. D. (2018, Jul 26). A Complete Electron Microscopy Volume of the Brain of Adult Drosophila melanogaster. *Cell, 174*(3), 730-743 e722. https://doi.org/10.1016/j.cell.2018.06.019

Zwart, M. F., Pulver, S. R., Truman, J. W., Fushiki, A., Fetter, R. D., Cardona, A., & Landgraf, M. (2016, 2016/8//). Selective Inhibition Mediates the Sequential Recruitment of Motor Pools. *Neuron, 91*(4), 944-944. https://doi.org/10.1016/j.neuron.2016.07.041